Modeling Dynamic and Steady Coronal Processes in the Alfvén Wave Solar Atmosphere Model

by

Judit Szente

A dissertation submitted in partial fulfillment
of the requirements for the degree of
Doctor of Philosophy
(Atmospheric, Oceanic and Space Sciences)
in the University of Michigan
2018

Doctoral Committee:

Professor Tamas I. Gombosi, Co-Chair
Professor Gabor Toth, Co-Chair
Dr. Judith T. Karpen, NASA Goddard Space Flight Center
Professor Enrico Landi
Associate Professor Susan T. Lepri
Research Professor Ward B. Manchester IV
Professor Kenneth G. Powell

Judit Szente

judithsz@umich.edu

ORCID ID: 0000-0002-9465-7470

ACKNOWLEDGEMENTS

My special thanks goes to my advisors: Professors Tamas Gombosi, Gabor Toth, Enrico Landi and Chip Manchester. I enjoyed their teaching, guidance, patience and help every day of the past years. I am feeling honored that I could learn from them and that they invested so much of their time and energy into my development. I am feeling very thankful for Tamas for hiring me and letting me be part of his group. I am grateful for his advising and for being supportive as much as humanly possible. I cannot thank him enough for giving me time off when I had difficulties in my personal life. Gabor spent an immense amount of time teaching me how to think and how not to think, in many aspects of life. I am certain that *none* of my projects would have been finished without him, and I am incredibly happy that he found me worthy of his time and patience. I am very thankful for Enrico for teaching me invaluable skills to become a scientist. I cannot thank him enough for not giving up on me when multiple times I lost my way in projects. I am grateful for his encouragement and motivating, continuous positive attitude towards me. I am very grateful for Chip for the many inspirational conversations and advising. I felt he treated students as colleagues from the beginning, and helped me understand basic physics with an infinite patience and positive thinking. I am truly overwhelmed by the help and mentoring I received over these year, both professionally and personally.

I would also like to thank to the dissertation committee, Dr. Judy Karpen, Professors Sue Lepri and Ken Powell for taking time to read this thesis, guiding me in making it a better one, and traveling to my defense. I am feeling honored having

them on my committee.

I would like to thank all my professors from inside and outside the department, especially to Professor and Chair Jim Slavin, who was always encouraging, and Professor Karl Krushelnick, who taught me formidable things about plasmas.

I would like to express my gratitude to the administration and IT staff, especially to Sandy Pytlinski, for helping our student life every way possible, and personally being there for me on multiple occasions. I would like to thank Deborah Eddy, Laura Hopkins, and Jan Beltran for their kindness and for the good atmosphere they bring to the department.

I would like to thank my office mates and students who made these years the most fun possible. I am especially grateful to John Haiducek for being my friend and helping me in many ways in life.

I would also like to thank people from outside the Department. Without Dr. Peter Erdi and Dr. Aron Tobias I would have never been able to make it to the front door of the Space Research Building, not to mention the country I am now living in. Their friendship and unconditional support shaped my life beyond my imagination.

I would like to thank my family, here in Ann Arbor and "there" in Budapest and Veszprem. It was very hard for them being patient with me and seeing me struggle sometimes. I would like to thank to my parents and to my brother for supporting me with all their might since I was born.

I literally cannot express with words how grateful I am to my husband. During the past 5 years he helped me as an advisor and then as a partner in life, in both roles with infinite energy and patience.

I would like to especially thank to Dr. Emese Dobay, who built my personality bit by bit during these years and taught me how to manage my life in a successful way.

I would like to thank Szilvia Sáray for being the always-inspiring best friend anyone

could ever wish for. She helped me through numerous difficult times and is always a great support for whatever comes.

I would like to express my gratitude to Péter Székely for teaching me the basics of physics and how to enjoy solving problems. His influence on my thinking is with me on a daily basis.

I would also like to thank to my friends and colleagues who substantially shaped my life and personality: to Deepti Bettampadi, Carrie Burlingame, Yuxi Chen, Tamer Elbayoumi, Zhenguang Huang, Meng Jin, Dorottya Lendvai, Pedro Mateu, Zsuzsa Nyitrai, László Ropolyi, and Zsófia Sárközy. I cannot write the complete list of names because I would never be able to submit this thesis. Even if not mentioned by name, I would like to thank everyone who helped and supported me during my PhD years, and also for those who did not.

“Même pour le simple envol d’un papillon,
Le ciel tout entier est nécessaire.”
/Paul Claudel/

TABLE OF CONTENTS

ACKNOWLEDGEMENTS ii

LIST OF FIGURES vii

LIST OF TABLES xiii

ABSTRACT xiv

CHAPTER

I. Introduction 1

1.1 Structure of the Sun 1
1.1.1 Solar Interior 2
1.1.2 Stratification of the Solar Atmosphere 2
1.2 Coronal and Solar Wind Observations 15
1.2.1 Spectral Observations of the Corona 17
1.2.2 Observing the Alfvén-Wave Turbulence in the Solar Wind 21
1.3 MHD Solar Corona Model 22
1.4 Outline 27

II. Coronal Jet Modeling 29

2.1 Introduction 29
2.2 Jet Observations and Models 30
2.3 Simulation Description 38
2.3.1 Coronal Model 38
2.3.2 Jet Model 43
2.3.3 Boundary and Initial Conditions 45
2.4 Simulation Results 50
2.4.1 Jet Generation by Magnetic Reconnection 51
2.4.2 Temperature 53
2.4.3 Density 54

2.4.4 Velocity 55
2.4.5 Flows, Fields, and Forces in the Outer Corona . . . 56
2.4.6 Mass, Momentum, and Energy Transport 58
2.4.7 Quasi-Periodic Recurrence 63
2.4.8 Energy Changes in the Corona 64
2.5 Comparison with Observations 68
2.6 Conclusions 74

III. Synthetic Spectrum 77

3.1 Introduction 77
3.2 Synthetic Spectra 78
3.2.1 Line Formation 78
3.2.2 Solar Corona Model 80
3.3 SPECTRUM Implementation 83
3.3.1 Synthetic Spectral Calculation 87
3.3.2 DEM and EM Calculation 92
3.4 Comparison with Observations 92
3.4.1 Open and Closed Magnetic Field Regions 95
3.4.2 Narrowband Imaging 99
3.4.3 Nonthermal Line Broadening and Effective Velocity 100
3.5 Summary of Chapter 3 106

IV. Summary and Future Work 108

4.1 Summary 108
4.2 Future Plans 109

BIBLIOGRAPHY 111

LIST OF FIGURES

Figure

1.1 Figure I-1. from Schrijver (2001). The evolution of solar atmosphere model paragidms over time are shown on three panels. Mass flows (indicated by arrows with the symbol ρ), electron beams (e^-), intermittent heating due to changes in the magnetic field connectivity (ϵ), radiative transfer, MHD waves create a dynamic atmosphere. 4

1.2 Figure I-1. from Athay (1976) shows an empirical-based temperature model of the solar atmosphere from the photosphere to the corona. . 5

1.3 Figure 1.19 from Aschwanden (2004). Electron density, neutral hydrogen density, and electron temperature models for the chromosphere and the lower corona. In the sharp transition region the plasma temperature rises by two orders of magnitude, the density drops by about one order of magnitude, and the H plasma becomes fully ionized within 100 km. See further references in the original textbook. 6

1.4 Figure 1. from Newkirk (1967) shows coronal electron densities in the equatorial solar corona derived from different techniques. The "Whang, Liu & Chang 1966" line corresponds to a theoretical model for comparison. See references in the original paper. 7

1.5 Figure 2. from Schmidt et al. (2012). Active region AR 111504 observed with the 1.5 meter solar telescope GREGOR Broad-Band Imager on June 17, 2012. The sunspot structure and surface granulation are clearly shown on this figure taken at wavelength 590 nm. 8

1.6 Image shows the solar corona during a solar total eclipse from 2015. Taken from `https://eclipse2017.nasa.gov/sites/default/files/publications/pocket_folder.pdf`. 11

1.7 Figure 1. from McComas et al. (2003). Polar plots of solar wind speed measured by the Solar Wind Observations Over the Poles of the Sun (Ulysses/SWOOPS; Bame et al., 1992) as a function latitude is shown during solar minimum (left) and maximum (right). In the center of the top panels there are images taken of the solar disc and corona with the EUV Imaging Telescope on board the Solar and Heliospheric Observatory (EIT/SoHO Delaboudinière et al., 1995) at 195 Å band, with the Manua-Loa K-coronameter (70-95 Å), and white light images taken with the SoHO C2 Large Angle Spectroscopic Coronagraph (SoHO/LASCO; Brueckner & Bartoe, 1983). The bottom panel shows the average monthly (white) and smoothed (red) sunspot numbers as a function of time. 14
1.8 Figure 7 from Kaastra et al. (2008) shows the oxygen ion concentration versus temperature assuming collisional ionization equilibrium. 17
1.9 Figure 6. from Cranmer et al. (2017) shows the height dependence of transverse velocity fluctuations in coronal holes and the fast solar wind. The curves are from theoretical models, while colored indicators report observations. The two solid curves correspond to velocity fluctuations 0 km/s and 6 km/s, the dotted line is for velocity fluctuations with amplitude 3 km/s with dimensionless outer-scale length-scale normalization constant 0.35. For references and details see the original paper and Cranmer & van Ballegooijen (2005). . . . 18
1.10 Upper panel (from Figure 4 of Brooks et al., 2009) is a DEM solution based on Hinode/EIS quiet Sun measurements of the coronal disk. This DEM is the representative quiet-sun DEM in the SolarSoft CHIANTI package. The dashed line shows a previously derived quiet-corona DEM (Brooks & Warren, 2006), and the lower panel shows their ratio. 20
1.11 Figure 1 from Klimchuk (2017) shows the predicted DEM response to low- and high-frequency nanoflares, arguing that the cool side of the DEM function is generated by impulsive rather than gradual heating mechanism. 21
2.1 Cut-planes across the jet region show the initial collisional heat exchange time scale calculated in [s], plotted on a logarithmic scale. X and Z axes correspond to the HGR coordinate system, see discussion in text. White lines show 2-dimensional magnetic field lines. 43

2.2 Initial configurations for the simulated polar jet in the vertical open-field region (top row) and the loop jet in the tilted closed-field region (bottom row). Shown are the radial velocity in the $Y = 0$ plane (left panels), the radial magnetic field on the solar surface $r = R_\odot$ with some representative field lines (middle panels), and a zoomed-in view of the jet location (right panels). The compact jet dipole is the small blue dot marked by the arrows on the upper hemisphere. The scales are indicated by the black arrows of the field-of-view (FOV), which define the physical size of the plotted regions. In the left bottom corners the indicator for the orientation of the coordinate axes of the images is shown. 48

2.3 The loop jet initial condition on the $Y = 0$ plane. From left to right, top row: total magnetic field strength, radial magnetic field component with some magnetic field lines, and density of the steady-state solar wind. Bottom row: proton pressure, electron pressure, and temperature ratio of protons to electrons. See Section 2.3 for details on the model. 49

2.4 Left: grid structure in a 2D cut at $Y = 0$ of the whole domain ($24R_\odot$). Middle: same, zoomed to $6.25R_\odot$, showing the first few levels of the adaptive, radially stretched grid. Right: zoomed to $0.3R_\odot$, showing several magnetic field lines near the jet dome. 50

2.5 Polar jet simulation at time $t = 1$ h 27 m 20 s (top row); loop jet simulation at time $t = 2$ h 27 m 30 s (bottom row). Left panels: radial velocity is color-shaded on a plane through the center of the jet; gray and blue lines represent magnetic field lines in front of and behind the plane, respectively. Middle and right panels: zoomed to the jet core at the same times, from different perspectives. Magnetic field lines and the null-point region on the separatrix surface ($B = 0$ isosurface) are color-shaded according to proton temperature. Shown in transparent gray is an isosurface of dense plasma ($\rho = 5 \times 10^{-15}$ g cm^{-3}). Selected pre- and post-reconnection magnetic field lines are labeled [2] and [1], respectively. 52

2.6 Density enhancement relative to the initial steady state in planes through the center of the polar (top row) and loop (bottom row) jets. Left panels: large-scale view of the solar wind; the partial white disk is the Sun. Right panels: close-up view near the solar surface. . 55

2.7 Plasma velocities for polar (top row) and loop (bottom row) jets color-shaded on selected magnetic field lines at the end of the simulations. Left panels: field-aligned component ($v_{\rm par}$). Right panels: perpendicular component ($v_{\mathbf{r}\times\mathbf{B}}$). The perpendicular component is projected along the cross product of the position vector $\mathbf{r}$ with the magnetic field $\mathbf{B}$, to distinguish positive and negative directions. . . 56

2.8 Polar jet at the end of the simulation. Top row: radial, latitudinal, and longitudinal velocity components (left to right). Middle row: radial magnetic field change (left) and latitudinal and longitudinal magnetic field components (middle and right). Bottom row: radial, latitudinal, and longitudinal components of the Lorentz force (left to right). All figures show the same plane through the center of the jet. The white disk is the Sun. 58
2.9 Integration regions for the polar jet. Left panel: the core integration region is the translucent box. The radial magnetic field component on the solar surface is color-shaded; selected magnetic field lines are shown. Middle panel: the coronal integration region is the pink-shaded volume. Right panel: plasma density is color-shaded near and on the solar surface. The black line marks the lower boundary of the coronal integration region at $1.015R_{\odot}$; the chromosphere is excluded from this region. 59
2.10 Integration results for the polar-jet core (left panels) and corona (right panels): changes in mass (top row), radial momentum (middle), and energies (bottom). Negative values of changes in the energies are not shown due to the logarithmic scale. See Section 2.4.6 for details. 61
2.11 Temperature and energy-density changes for the polar jet at the end of the simulation. Top row, left to right: proton temperature, internal energy density, and kinetic energy density. Bottom row: electron temperature, magnetic energy density, and gravitational energy density. All figures show the same plane through the center of the jet as in Figure 2.8. The white disk is the Sun. 62
2.12 Line-of-sight synthetic images of the simulated polar jet (left panels) compared to EUV and Hinode/XRT observations (right panels) of Jet 3 (top and middle rows) and Jet 1 (bottom row). Both images within each pair are shown on the same logarithmic color scale. For further discussion see Section 2.5. 71
2.13 Line-of-sight synthetic and observed images in the same layout as Figure 2.12. The EUV observations (right panels) are of Jet 2. For further discussion see Section 2.5. 72
3.1 AWSoM steady-state simulation results of CR 2063 (*left*) and CR 2082 (*right*), showing electron density in the top row and radial bulk speed in the bottom one in a cut-plane viewed from the LOS direction, along with a similarly contour-colored 1.002 solar radii spherical surface of the solar body. The field of view is 6 solar radii in each image. . . . 82
3.2 AWSoM steady-state simulation results of CR 2063 (*left*) and CR 2082 (*right*) respectively, showing parallel proton (top row), perpendicular proton (middle row), and electron temperatures (bottom row). A cut-plane from the LOS direction is shown, along with a similarly contour-colored 1.002 solar radii spherical surface of the solar body. The field of view is 6 solar radii in each image. 83

3.3 *From top to bottom:* Model validation of AWSoM steady-state simulation results of CR 2063 and CR 2082 respectively, comparing line-of-sight SoHO/EIT observations to synthetic images. 84
3.4 *From top to bottom:* Model validation of AWSoM steady-state simulation results of CR 2063 and CR 2082 respectively, comparing OMNI 1 AU in-situ plasma measurements (*red*) with simulated data sampled at the same location of the domain (*black*). 85
3.5 Spectral calculation validation of uniform density, isothermal plasma input from SPECTRUM (black) compared to CHIANTI's synthetic spectral calculation (turquoise). 88
3.6 *From left to right:* White boxes show the Hinode/EIS observation sites of CR 2063 and CR 2082 on SoHO/EIT narrowband images. . 93
3.7 *From left to right:* Magenta boxes represent the three data boxes where the MHD solution data were extracted for synthetic spectral calculations corresponding to observation sites of CR 2063 and CR 2082 with field of view 0.8 solar radii. 94
3.8 Coronal EM (*up*) and DEM (*down*) of observed *(black)* and simulated *(green)* coronal plasmas in closed *(left)* and open *(right)* magnetic field regions are shown. 95
3.9 Comparison of coronal spectra of the observed *(black)* and simulated *(green)* plasmas in the closed magnetic field region. The synthetic spectra are scaled down by a factor of 10. 96
3.10 Comparison of coronal spectra of observed *(black)* and simulated *(green)* plasmas in open *(right)* magnetic field region. The synthetic spectra are scaled down by a factor 10. 97
3.11 Synthetic spectral line profile of Fe XIII 202.044 Å obtained by SPECTRUM (*green*) compared to Hinode/EIS observation (*black*) for the West limb (*top*) and the North polar (*bottom*) observations of CR 2063. 99
3.12 *Left to right:* LOS view of the modeled solar corona of CR 2063 and CR 2082. Synthetic narrowband images are calculated using synthetic spectra obtained from SPECTRUM in the wavelength range 165 Å to 350 Å, and instrumental response function from SoHO/EIT 195 Å. (The concentric cirles appear due to the low resolution of the images.) 100
3.13 *Left to right:* FWHM for spectral lines of selected ions, having nonthermal effects included and excluded from the line profile calculation. The difference between the left and right panel shows that nonthermal broadening has a significant effect on line widths. 101
3.14 Figure 7 from van der Holst et al. (2010) shows the transverse velocity perturbation vs radial distance in a coronal hole of a two-temperature 3D simulation. 102

3.15 Figure 5 from Hahn et al. (2012) shows effective velocity of selected spectral lines vs radial distance in the coronal hole of CR 2082. Effective velocity profiles were interpreted as strong wave damping in the low coronal region, much stronger than expected by Alfvén-wave-heated theoretical coronal models. Dashed lines show for the effective velocity as a function of radial distance for each emission line in the case of undamped waves normalized at 1.1 $R_{\odot}$. 103
3.16 Predicted intensity (*top,left*), FWHM (*top,right*), Doppler shift (*bottom,left*), and effective velocity (*bottom,right*) of selected spectral lines along radial distance in the coronal hole of CR 2082. Effective velocities show little or no wave damping in the low coronal region compared to what was observed. 104
3.17 Effective velocities obtained from synthetic spectra using a 1D data set extracted from the same observation as in Figure 3.16 to avoid the line-of-sight effect. 105
3.18 2D synthetic maps of intensity (*top, left*), FWHM (*top, right*), Doppler shift (*bottom, left*), and effective velocity (*bottom, right*) of line Fe XIII 202.044 Å from the observer's LOS from CR 2082. 106

LIST OF TABLES

Table

1.1 Typical plasma beta values in different solar regions. Based on Table 5.1 from Schrijver & Siscoe (2009) and Table 1.1 from Aschwanden (2004) 9

1.2 Solar wind properties at Earth, based on Table 9.1 from Schrijver & Siscoe (2009). 15

ABSTRACT

This thesis presents a study of the solar wind acceleration and coronal plasma heating with techniques that use both observational data and magnetohydrodynamic (MHD) simulations. Its focus is estimating the mass, momentum, and energy transport from the chromosphere to the solar corona under different conditions, both at small scales, by building an MHD model of a coronal jet, and at global scales, by computing synthetic spectra.

The first part of the thesis estimates how much coronal jets contribute to the solar wind outflow and study their effect on the global corona. We present the computational implementation of a coronal jet into the two-temperature Alfvén Wave Solar Atmosphere Model (AWSoM) within the Space Weather Modeling Framework (SWMF). This is the first jet simulation implemented within a realistic, physically self-consistent global solar coronal model. We describe the interaction of the jet with the background solar-wind plasma and find that the large-scale corona is affected significantly by the outward propagating torsional Alfvén waves generated by our polar jet, across 40° in latitude and out to 24 $R_{\odot}$. We compare the physical properties and dynamic behavior of the polar jet to observations using line-of-sight synthetic images at EUV and X-ray bands, and find very close matches in terms of physical structure, dynamics, and emission. We conclude that even though jets interact with a large volume of coronal plasma, their contribution to the above-mentioned transport processes is much smaller than the average background solar-wind contribution. Also, it shows that jets introduce disturbances to the solar wind that can be detected by the

Parker Solar Probe in-situ instruments during the close approaches of the spacecraft to the Sun.

The second part of the thesis compares observational and synthetic spectra of the quiet Sun. It presents the implementation of SPECTRUM, which is a post-processing tool within SWMF, that predicts the solar spectrum providing line profiles for any user-defined line of sight. SPECTRUM takes into account Doppler shift, thermal broadening, anisotropic proton and electron temperatures, and the broadening due to low-frequency Alfvén waves. It can also apply instrument response function and instrumental broadening for any instrument. We use the three-temperature AWSoM model to obtain synthetic spectral observations of three different observational sites. Comparing the predicted spectra with Hinode/EIS observations, the model shows less significant wave damping in the low corona region, below 2 solar radii, and the observed effective velocity profiles are not explained by the solely Alfvén-wave driven coronal model.

The measured quiet-Sun emission measure (EM) and differential emission measure (DEM) curves with predictions determined from output plasma parameters of AWSoM are compared, just as line-of-sight narrowband images. SPECTRUM shows as a more rigorous model validation tool than only comparing to line-of-sight images and 1 AU in-situ observations, and that it allows us to predict observables for upcoming future missions (Solar Orbiter). At the same time, SPECTRUM also enables scientists to utilize AWSoM predictions to carry out in-depth, quantitative studies of the physics of solar corona heating and wind acceleration.

With these additions to the AWSoM model and the SWMF, we extended the platform to study the dynamic and quiet solar corona. These are significant steps towards understanding the phenomena of coronal heating and solar wind acceleration.

CHAPTER I

Introduction

This thesis studies the solar corona: how it is heated and how solar wind is accelerated. We do this by using numerical models of the solar corona, and examine both dynamic (jets) and steady (quiet-Sun spectra) processes.

In the following we present an introduction to coronal jets and synthetic spectra of the solar corona. Due to the complexity of these topics, the review discusses what is the solar corona, how it is observed, and how it is modeled, based on popular textbooks on the topic (Golub & Pasachoff, 1997; Gombosi, 1998; Gurnett & Bhattacharjee, 2005; Phillips et al., 2008; Schrijver & Siscoe, 2009; Landi Degl'Innocenti, 2014) along with review articles (Hollweg, 1978; Velli et al., 1989; Cranmer, 2009; Klimchuk, 2006; Cranmer, 2009; Klimchuk, 2015; Laming, 2015; Cranmer et al., 2017), unless citations indicate the origin otherwise.

1.1 Structure of the Sun

The Sun is a middle-aged, metal-rich, main-sequence star on the Orion-Cygnus Arm of the Milky Way. Its mass is about $M_\odot = 2 \times 10^{30}$ kg, radius $R_\odot = 7 \times 10^8$ m. The differential rotation has a period of 24-38 days, depending on the latitude. Its average equatorial rotation period is about 26 days, and polar about 35 days. The mean synodic rotation rate is about 27.2753 days, which is the length of a Carrington

Rotation. Carrington Rotations are numbered starting with 1, which rotation begins on October 13, 1853. The average equatorial magnetic-field strength is about 10^{-4} T, while in sunspots the magnetic field strength can be over a thousand times larger. The solar effective blackbody radiation temperature is 5780 K.

1.1.1 Solar Interior

The solar core contains about half of the solar mass, and is within a volume of a sphere with radius 0.25 $R_\odot$, where nuclear fusion is generating energy at temperature 1.5×10^7 K. The core energy is transported into the outer regions through the radiative zone. The top of the radiative zone is at about 0.75 $R_\odot$.

The convection zone is the upmost layer of the solar interior. In this region buoyancy-driven flows carry the energy from the radiative zone to the solar surface. The convective plasma appears as granulation on the solar surface, with granules about 1000 km in diameter. Solar interior measurements are based on helioseismology (a technique to study the sub-surface sound wave propagation in the Sun), without which we would have no other observational information of the solar interior other than the observed granulation and the neutrino flux escaping from the core generated by the ongoing nuclear reaction.

It is assumed that the magnetic flux generation is within a thin layer at the base of the convective zone. Plasma motions have a direct effect on the generation of the solar magnetic field observed in the atmosphere. The combination of the sub-surface convective motions and differential rotation is responsible for the solar dynamo and the genartion of the magnetic field and hence solar activity.

1.1.2 Stratification of the Solar Atmosphere

The solar atmosphere is mostly composed of hydrogen-helium plasma with less than 2% (by number) of heavier (also called "metallic" in astronomy) elements

(mostly O, C, Ne, Fe). The helium abundance ranges from 5% to 10%, depending on the region of observation.

The solar surface is called the photosphere, above which the solar atmosphere is described in three layers: the chromosphere, the transition region and the corona. The splitting of the gaseous solar atmosphere into layers is somewhat subjective, not only because no distinct boundaries exist, but also because there are discrete structures interconnecting these layers with each other (Athay, 1976). The solar atmosphere is indeed very inhomogeneous; streamers and loops of different size form colder and warmer regions. The evolution of the view on the solar atmosphere is shown on a representative sketch in Figure 1.1. The rightmost panel corresponds to our current view on the complexity of the atmospheric plasma. Despite its inhomogenity, the solar atmosphere is usually described based on its average temperature and density profiles along radial distance from above the photosphere. Based on a 1D model, Figure 1.2 shows the temperature of the atmospheric layers along the radial distance. The temperature decreases with height in the photosphere, but after reaching a minimum at about 4200 K, it increases up to 10^4 K, where within the thin transition region (about 100 km thick) the temperature suddenly increases to millions of K. In the corona then the temperature further increases, depending on the configuration of the magnetic field. Figure 1.3 shows the sudden electron density drop at the transition region, along with the temperature change. The neutral hydrogen density profile clearly indicates that the plasma becomes fully ionized by reaching high chromospheric temperatures. Finally, based on multiple measurements, Figure 1.4 shows the density along radial distance from the solar surface to beyond Earth (which is 1 AU $= 1.5 \times 10^8$ km), about 215 $R_\odot$ from the Sun).

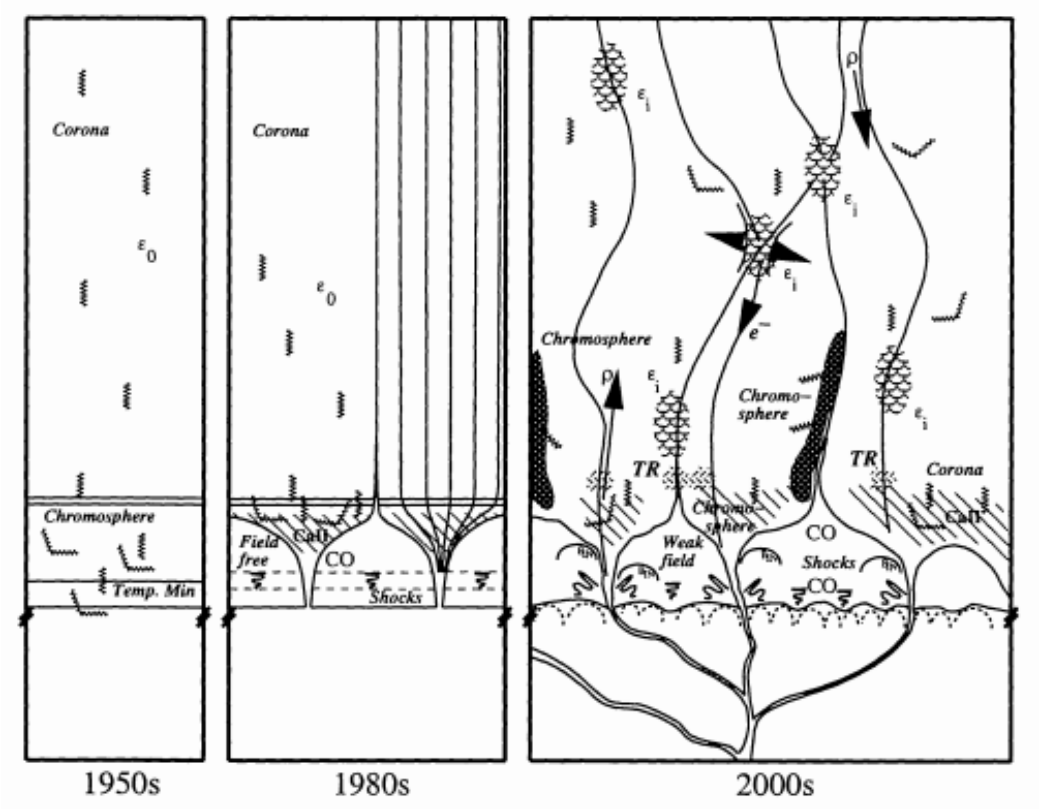

Figure 1.1: Figure I-1. from Schrijver (2001). The evolution of solar atmosphere model paragidms over time are shown on three panels. Mass flows (indicated by arrows with the symbol ρ), electron beams (e^-), intermittent heating due to changes in the magnetic field connectivity (ϵ), radiative transfer, MHD waves create a dynamic atmosphere.

1.1.2.1 Photosphere

Being a gaseous object, the solar surface is defined somewhat arbitrarily through the definition of optical depth:

$$\tau_\lambda(s) = \int_{s_0}^{s} \alpha_\lambda(s')\, ds' \tag{1.1}$$

where α is the absorption coefficient of the medium and s is the location relative to s_0 within the medium. The solar effective surface is defined as the region where the optical depth is 1. This practically corresponds to the layer below which we do not see photons from (they are more likely absorbed before reaching the less dense region

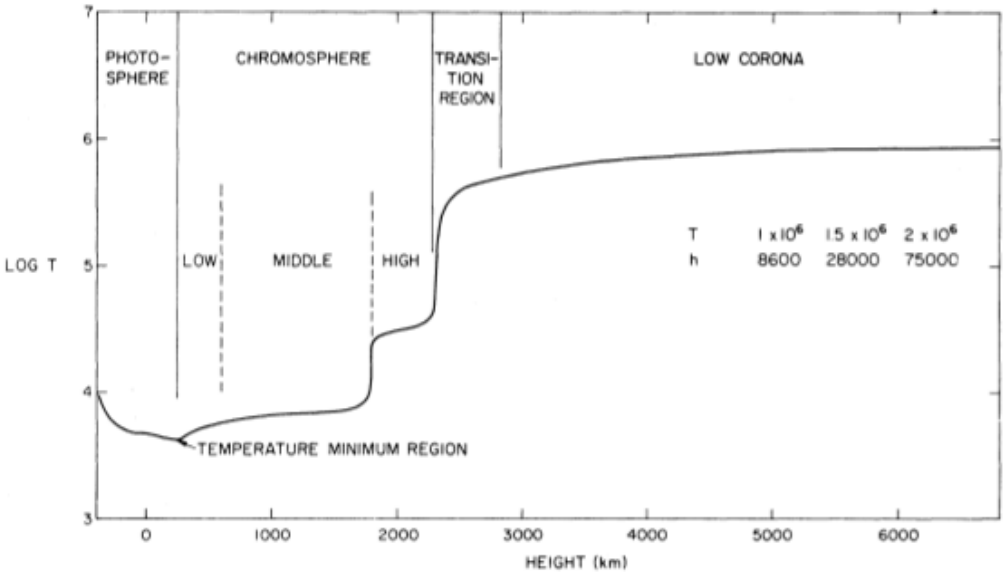

Figure 1.2: Figure I-1. from Athay (1976) shows an empirical-based temperature model of the solar atmosphere from the photosphere to the corona.

of the atmosphere), but above which most outward-directed radiation can reach the observer. This visible solar region is called the photosphere. The photosphere has a temperature of about 4000 - 6000 K, density 4×10^{-4} kg/m^3 and the region is about 300-500 km thick. The dominant radiation in this region is in the visible range; the Sun is observed in this wavelength range like a black body radiation source with peak temperature about 5780 K. Next to the continuum radiation, there are also visible Balmer emission spectral lines of H originating from this region. The plasma is only partially ionized, dense and collisional. This means that the mean free path of particles and photons are unity or smaller, and the different species share the same temperature. All particles have a Maxwellian velocity distribution, and the plasma is in Local Thermodynamic Equilibrium. The radiative losses are playing a significant role in the energy budget of the region, and are considered as drivers of the convection in the photosphere. Convection models of this region are based on combining the magnetohydrodynamic equations (see Section 1.3) with the radiative transport of both continuum and line radiation of elements (see, for example, Carlsson

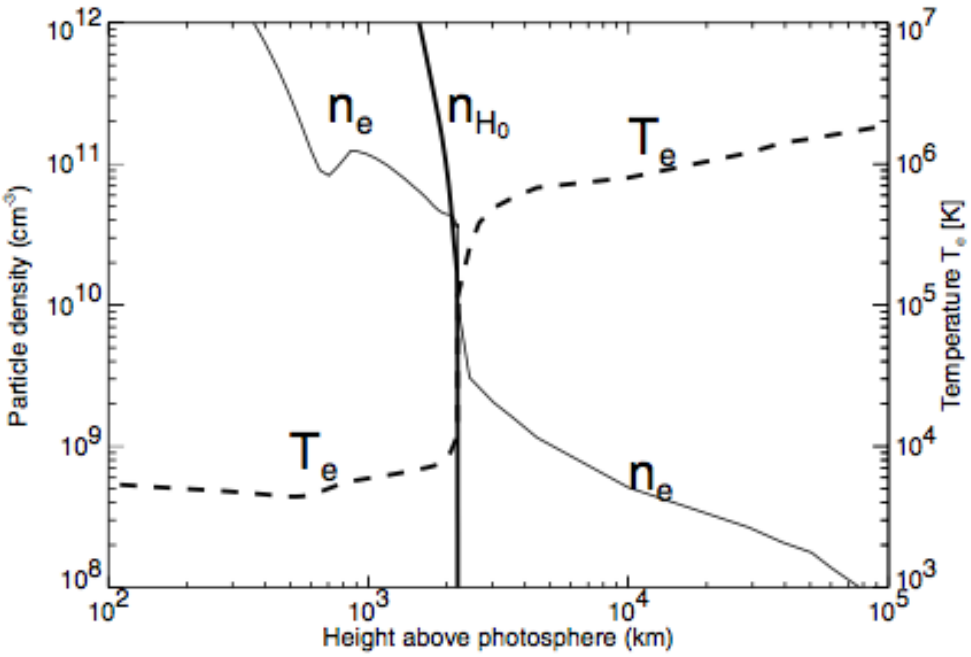

Figure 1.3: Figure 1.19 from Aschwanden (2004). Electron density, neutral hydrogen density, and electron temperature models for the chromosphere and the lower corona. In the sharp transition region the plasma temperature rises by two orders of magnitude, the density drops by about one order of magnitude, and the H plasma becomes fully ionized within 100 km. See further references in the original textbook.

et al., 2004).

As mentioned before, the solar surface is nonuniform: it shows continuous granulation at a scale of about 1000 km, and is darkened by sunspots and illuminated by bright points. Figure 1.5 shows a sunspot observation with the surface granulation on the surrounding surface. Sunspots are dark regions of $\sim$ 10000 km size, with low-temperatures (4-5000 K), strong magnetic fields (10^{-1} T), and lifetimes of a few solar rotations. Sunspot number, location, and polarity are highly connected to the 22-year solar cycle. Along with sunspots, smaller and weaker (10^{-4} T) magnetic field regions emerge to the surface, forming bright spots on the surface. Bright points are passively carried by the granular flows on the surface, collecting in the network surrounding supergranules 20000 km in diameter. Convective flows also generate per-

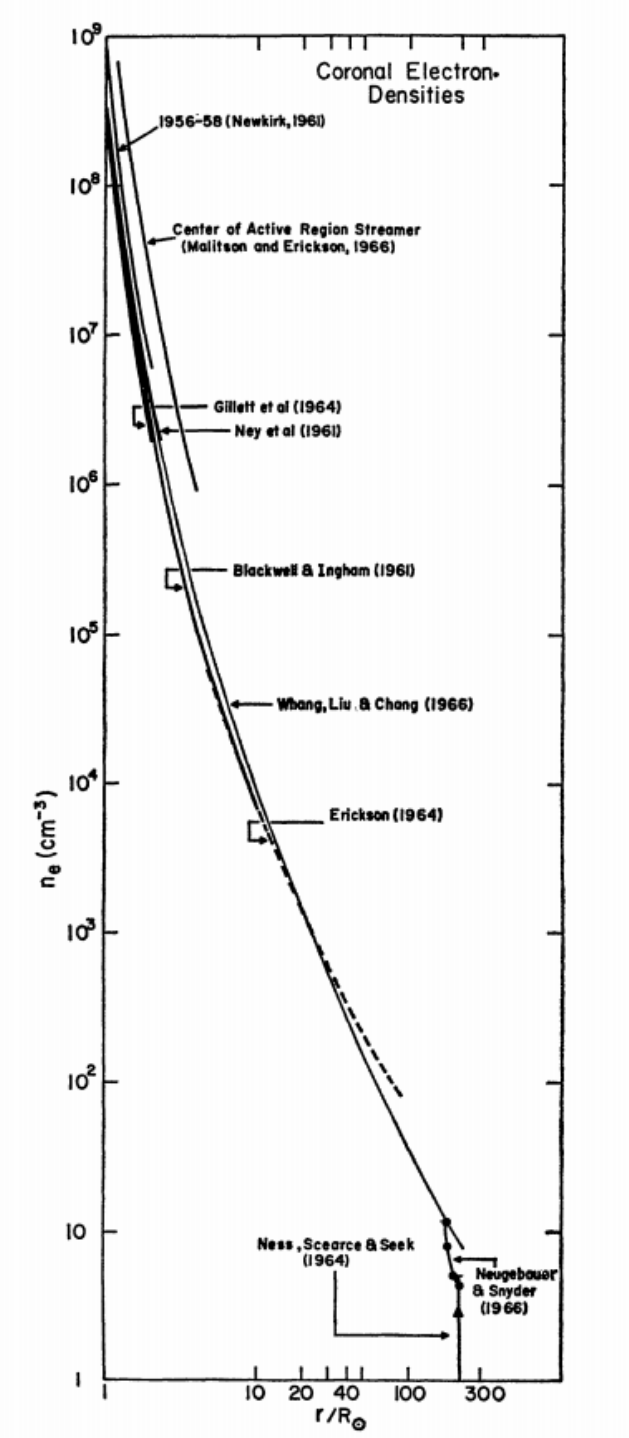

Figure 1.4: Figure 1. from Newkirk (1967) shows coronal electron densities in the equatorial solar corona derived from different techniques. The "Whang, Liu & Chang 1966" line corresponds to a theoretical model for comparison. See references in the original paper.

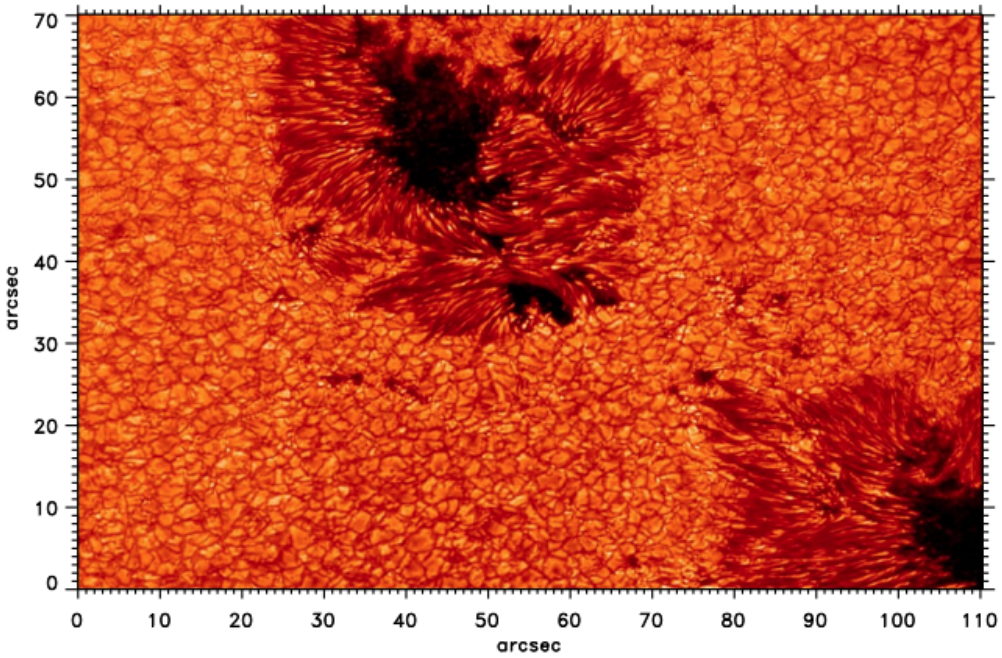

Figure 1.5: Figure 2. from Schmidt et al. (2012). Active region AR 111504 observed with the 1.5 meter solar telescope GREGOR Broad-Band Imager on June 17, 2012. The sunspot structure and surface granulation are clearly shown on this figure taken at wavelength 590 nm.

turbations and oscillations that are observed in waves, possibly being energy sources for the plasma above the photosphere.

1.1.2.2 Chromosphere

Above the photosphere the temperature rises to about 10^4 K and the density drops by an order of magnitude compared to below, within 2500 km. At the top of the chromosphere the H component of the plasma is fully ionized, and H, He, Ca II, and K lines are forming in this region. Ionization is the key process within the region: it is believed that the first ionization potential (FIP) effect takes place on the bottom and top of this layer: the change from photospheric to coronal ion abundance depends on the FIP of that element. While the direction of change is still under debate (whether the high FIP elements are depleted or the low FIP ones are enhanced), it is usually assumed that low FIP elements have abundances enhanced by a factor

of 4. For example O, Ne, and He (high FIP) are of photospheric abundance, while Mg, Si, and Fe (low FIP) are of 4 times enhanced in the corona compared to their photospheric abundances. It is commonly assumed that the reason for this is likely to be found in the coronal heating mechanism, more precisely the ponderomotive force of Alfvén waves acting on the plasma. More on the FIP effect can be found in Laming (2015).

The plasma undergoes an important change within this region: the thermal pressure is less and less dominant compared to the magnetic pressure in the upper chromosphere. The ratio between the two is the plasma beta: $\beta = \frac{p_{thermal}}{p_{magnetic}}$. The different plasma beta values are listed in Table 1.1.

Location	β
solar interior, base of convection zone	10^4
photosphere	14
hot corona	0.2
cool corona	0.07
corona, above active region	10^{-4}
outer corona ($> 5R_\odot$)	7

Table 1.1: Typical plasma beta values in different solar regions. Based on Table 5.1 from Schrijver & Siscoe (2009) and Table 1.1 from Aschwanden (2004)

The chromosphere contains a network of spicules and jets, along with brighter plage and darker filament regions. The plasma density drops with height, and by the top of the chromosphere the atmosphere is optically thin. This means that the photon mean free path is large enough for photons to leave the atmosphere, and the atoms behave as scattering centers of the incoming radiation from the lower regions. The particles are still collisional, so the particle velocities have the same Maxwellian distribution.

The chromosphere is driven by the photospheric processes. The photospheric 5-minute oscillations generate a 3-minute oscillation in the chromosphere. The upward propagating photospheric-generated acoustic waves were observed in Ca II lines. The

supergranular flow field of the photosphere creates a chromospheric network of bright bands. The greater plasma emission in the network indicates excess heating in the regions with larger photospheric magnetic field beneath, but the origin of the increased heating is debated. Energy transport by waves has been estimated from multiple observations, resulting in a controversy over result whether or not enough energy is transported via chromospheric oscillations to heat the coronal plasma, and generate the solar wind.

1.1.2.3 Transition Region

In the transition region the chromospheric plasma suddenly heats up to approximately a million K over a distance of 100 km. Because the density drops exponentially in this region, the radiative losses are inefficient ($Q_{rad} = n_e n_H \Lambda(T_e)$ is the optically thin radiation with N_e and N_P electron and proton number densities and $\Lambda(T_e)$ is mainly electron-temperature dependent radiative cooling), resulting in an excessive heating in this region. The plasma in this region is radiating in UV and EUV lines of heavy ions (e.g., C IV, O IV, Si IV), with a not yet understood average red shift in their emission. Because the density falls about 2 orders of magnitude, by the top of the region and the only significant processes are 2-body collisions and radiative or dielectronic recombinations. Most ions are in ground states and there are only few excited states. The plasma is optically thin.

1.1.2.4 Solar Corona

The outermost part of the solar atmosphere is called the corona. It is difficult to define where the corona begins, as there are significant inhomogeneities both spatially and temperature-wise in the region. Despite the inhomogeneity it is common to use the term "corona" for the plasma above 6×10^5 K. Due to the momentum obtained from thermal pressure, Alfvén wave pressure and other sources, the coronal

plasma is leaving the atmosphere continuously, traveling along magnetic fieldlines. This continuous outflow is called the solar wind. The supersonic solar wind travels out to the termination shock, where it becomes subsonic before reaching the heliopause, which is the contact surface of the solar wind plasma with the interstellar medium.

The corona is very hot plasma (millions of K) that radiates in UV and EUV lines of heavy ions (e.g., Fe IX, Fe XII, Fe XIV). Due to the sudden doubling of plasma along the line of sight, the limb is bright compared to the disc-center observations (opposite of photospheric observations). Because of the low density, the magnetic field dominates the plasma bulk motions. The acceleration and heating of the solar wind are among the main fundamental yet unsolved problems of the solar physics community. The corona shows structures from the smallest observed scales to global structures, including: jets, coronal mass ejections (CMEs), waves, loops, streamers, and plumes. Figure 1.6 shows several of these features on an eclipse observation. The

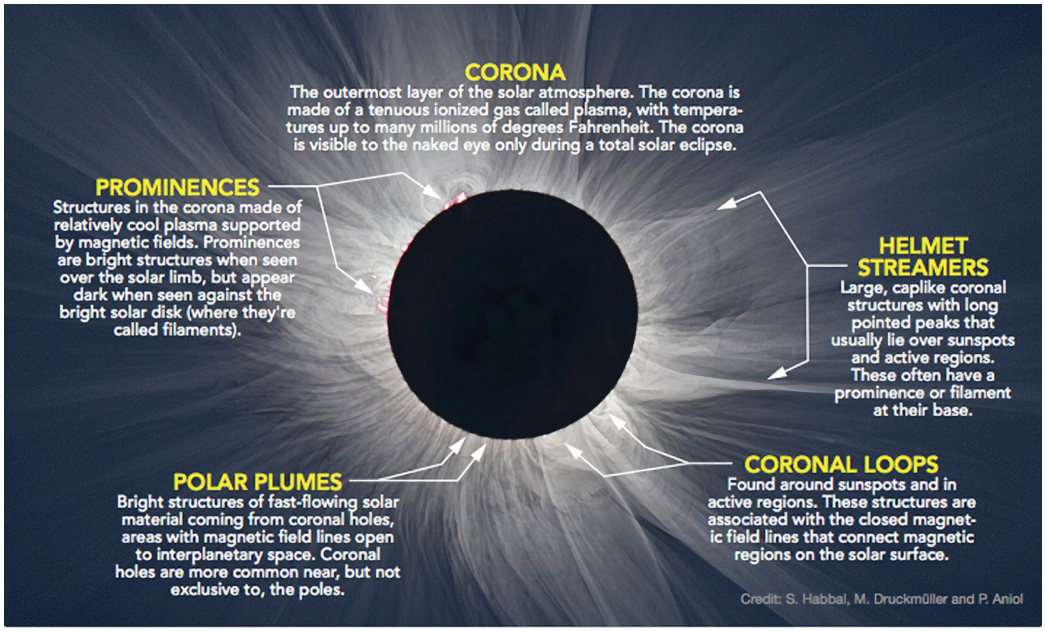

Figure 1.6: Image shows the solar corona during a solar total eclipse from 2015. Taken from `https://eclipse2017.nasa.gov/sites/default/files/publications/pocket_folder.pdf`.

largest structures observed in the corona are streamers, which, during solar minimum,

are equatorial phenomena, extend out to several solar radii, last for long time periods, and are observed in white light by coronagraphs. They correspond to closed magnetic field regions. Helmet streamers have footpoints in bright, dense active regions, closing about a solar radius above the solar surface, ending with radial outflow.

Coronal holes correspond to open magnetic field regions, where the plasma is less dense and radiates less; hence these regions appear darker in EUV images. The solar wind flows into the interplanetary space along the radial magnetic field with significantly larger speed and lower temperature than observed from closed magnetic regions.

Loops correspond to hot, dense plasma structures originating from the lower layers of the Sun, connecting opposite polarity of magnetic field regions on the photosphere. Plumes correspond to bright, plasma outflows in coronal holes, observed in EUV, at both polar and equatorial regions. Because the following chapters focus on the solar corona, in the following sections we discuss the coronal observations and models in more detail.

The solar corona temperature is fundamentally dependent on the magnetic field structure (Vaiana & Rosner, 1978). The relationship between the magnetic flux and plasma temperature in the solar atmosphere is fundamental and has been noticed as well in stellar observations. The plasma heating depends on the strength and geometry of the magnetic field in ways that remain poorly understood.

As mentioned before, the inhomogeneity of the corona is due to the organization of the magnetic field of the Sun. The Sun has a magnetic field, which is dynamically generated in the interior by the continuous bulk motions of the convective rotating star. The emergence of magnetic flux generates solar activity on and above the surface. The phenomenon of magnetic field generation is studied by dynamo theory, explaining the 11 year reversal cycle of the magnetic field, the amplification and emergence of magnetic field from below the solar surface, and the differential rotation of the outer

layers. In general, the corona radiates stronger at regions where plasma is denser and hotter, which often occurs where the magnetic field is stronger. It is also observed that hot plasma tends to follow the magnetic field direction in low plasma beta regions (frozen-in condition), and heat is conducted preferentially parallel to the magnetic field. Moreover, for non-collisional plasmas in strong magnetic fields, the warmer the plasma, the more anisotropic the heat conduction is: with increasing temperature the parallel conductivity increases, and perpendicular one decreases. The coronal loop length to width ratio therefore reflects the anisotropic plasma conductivity and hence temperature of the region. Loop thermodynamics reflects the temperature's strong dependence on magnetic field geometry.

Because the corona is the outermost region of the Sun's atmosphere, the ongoing coronal processes are direct drivers of space weather and it is important to understand and forecast them. The Earth's magnetosphere is in continuous connection with the solar wind, so it is of utmost interest to understand the dynamic and quiet solar corona, which is the topic of this thesis.

1.1.2.5 Solar Wind

The solar wind is a continuous outflow of particles from the solar atmosphere into the interplanetary space, carrying magnetic flux along. The supersonic expansion of the solar wind, along with the spiral structure of the expanding magnetic field within the interplanetary medium, were first described by Parker (1958). In the case of an approximatly dipolar field, the current sheet separates the fields of opposite polarities of the two hemispheres. The solar wind originates either from open magnetic field regions (fast wind) or from anywhere else (slow wind). The regions of open field are called coronal holes, where solar wind outflows are faster and less ionized than the slow wind of other origins. Figure 1.7 shows the solar wind speed measurements during the two orbits of the Ulysses space craft (Wenzel et al., 1992) along with

solar activity (sunspot number). The figure shows that the structure of the solar

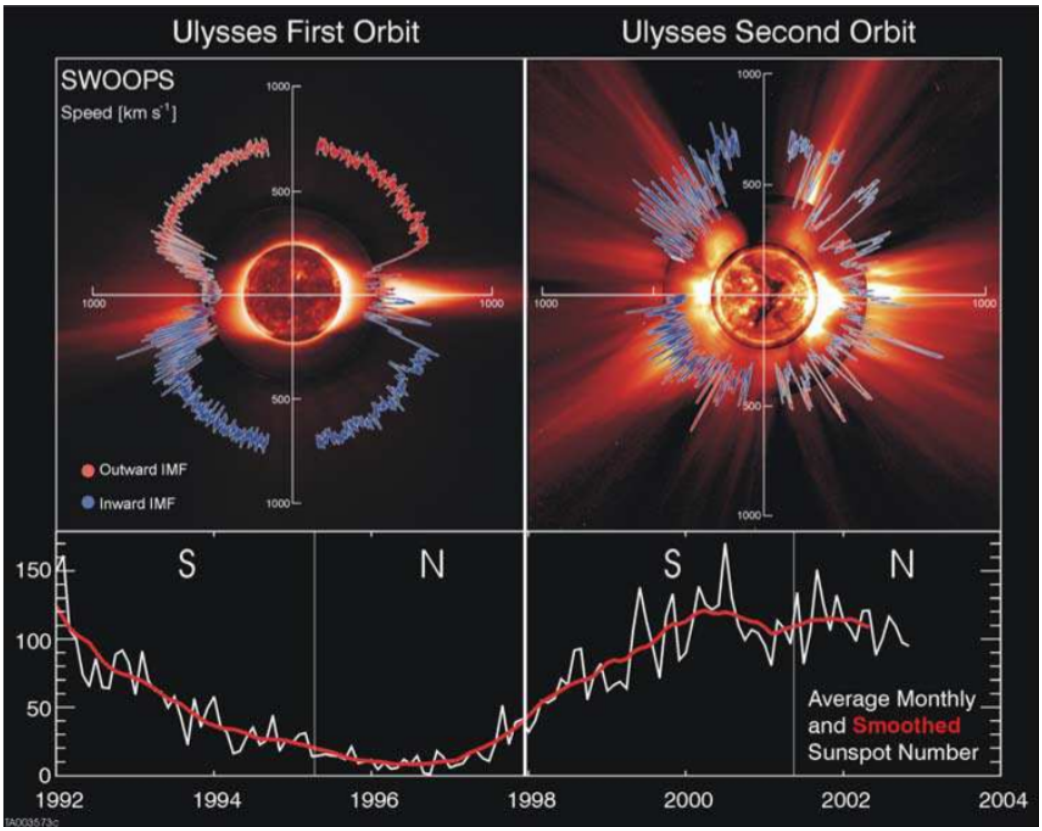

Figure 1.7: Figure 1. from McComas et al. (2003). Polar plots of solar wind speed measured by the Solar Wind Observations Over the Poles of the Sun (Ulysses/SWOOPS; Bame et al., 1992) as a function latitude is shown during solar minimum (left) and maximum (right). In the center of the top panels there are images taken of the solar disc and corona with the EUV Imaging Telescope on board the Solar and Heliospheric Observatory (EIT/SoHO Delaboudinière et al., 1995) at 195 Å band, with the Manua-Loa K-coronameter (70-95 Å), and white light images taken with the SoHO C2 Large Angle Spectroscopic Coronagraph (SoHO/LASCO; Brueckner & Bartoe, 1983). The bottom panel shows the average monthly (white) and smoothed (red) sunspot numbers as a function of time.

wind changes dramatically as solar activity changes. During quiet Sun conditions, the solar wind has a bimodal structure and can be discussed as slow and fast wind. Not only the velocities are different in the different winds, but also the elemental abundances, the temperature structures, and densities. Table 1.2 summarizes the differences below. The high speed of the fast solar wind made it clear that the thermal

Property (1 AU)	Slow wind	Fast Wind
Speed	430 ± 100 km/s	800 ± 100 km/s
Density	10 cm^{-3}	3 cm^{-3}
Flux	$(3.5 \pm 2.5) \times 10^8$ $cm^{-2}s^{-1}$	$(2 \pm 0.5) \times 10^8$ $cm^{-2}s^{-1}$
Magnetic Field	$(6 \pm 3) \times 10^{-9}$ T	$(6 \pm 3) \times 10^{-9}$ T
Proton Temperature	$(4 \pm 2) \times 10^4$ K	$(2.4 \pm 0.6) \times 10^5$ K
Electron Temperature	$(1.3 \pm 0.5) \times 10^5$ K	$(1 \pm 0.2) \times 10^5$ K
Isotropies	isotropic T_p	$T_{p_\parallel} > T_{p_\perp}$
Variability	highly variable	uniform, slow changes
He abundance	He/H ∼ 1-30%	He/H ∼ 5%
Ion Abundance	low FIP enhanced	photospheric abundances
Ion Density	n_i/n_p variable	n_i/n_p constant
Ion Temperature	$T_i \simeq T_p$	$T_i \simeq (m_i/m_p)\, T_p$
Ion Velocity	$v_i \simeq v_p$	$v_i \simeq v_p + v_a$
Origin	streamers and transient openings	coronal holes

Table 1.2: Solar wind properties at Earth, based on Table 9.1 from Schrijver & Siscoe (2009).

energy input from the coronal base is not sufficient to energize the plasma outflow thermally (Parker, 1965). The additional energy source that heats and accelerates the solar wind is not yet confirmed. There are several theories among which nanoflare heating, and Alfvén-wave dissipation are the leading ones (Parker, 1972; Klimchuk, 2006, 2015; Cranmer, 2009). While nanoflare heating theories suppose that small-scale reconnection events impulsively energize the plasma, Alfvén-wave heating happens via the continuous interaction of waves with the plasma. Although we are going to use a coronal model based on Alfvén-wave heating, we wanted to note that both the theoretical and modeling work related to solar wind acceleration and heating is under development during the time this thesis is written.

1.2 Coronal and Solar Wind Observations

The corona was observed long before any instrumentation was developed for solar observations. The solar corona is several magnitudes less bright than the solar disk in the visible wavelengths, also compared to the brightness of the clear sky, so it is

very difficult to observe the corona without any instruments, but it can be clearly seen during total solar eclipses. The observed coronal light is produced by different processes: strongly polarized Thomson scattering by free electrons (K-corona), reflection by dust particles (F-corona), infrared thermal emission of dust surrounding the corona (T-corona), and emission by coronal plasma in isolated spectral lines of coronal ions (E-corona). The corona was first observed both spectroscopically and via imaging at visible wavelengths. The E-corona mostly emits in the UV and X-ray wavelengths, less total energy than the K, F and T coronas, due to its smaller range and overall emission.

As previously noted, the corona is optically thin, so all observed structures are integrated images of all the emitting plasma along lines of sight, passing entirely through the corona, incorporating multiple structures. To decompose the spatially and thermally distinct formations, images are taken at multiple wavelengths dominated by emission from different heights of the solar atmosphere and also at different temperatures.

In the optically thin, hot plasmas of the corona, the main components (H, He) are fully ionized and produce no significant emission compared to the line emission of elements of lower abundance (10^{-4} or smaller relative to hydrogen), which in case of the solar corona are Fe, Si, S, O, N, Ne, Mg, Na, Al, Ca, Ar. The abundance of ionization stages of an element depends on the electron temperature and the electron binding energy. At low and high temperatures, the gas is either not hot enough to strip enough electrons from the element, or so hot that all electrons are already stripped from the atom. The result is that the abundance curve peaks at a certain temperature, where the ionization level is the most probable, which is the temperature of maximum formation. An example of the charge state distribution for an element is shown in Figure 1.8. The temperature of maximum formation is noted further on when line emissions are discussed along with the wavelength of the corresponding

transition. Line formation is going to be discussed in Chapter III.

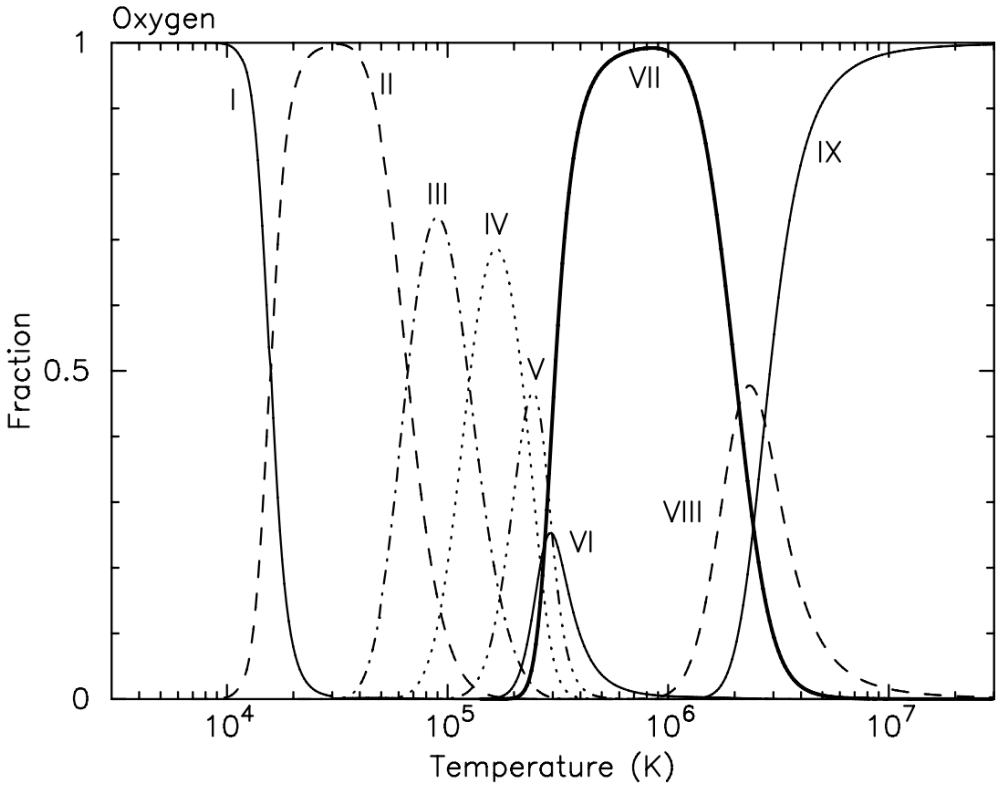

Figure 1.8: Figure 7 from Kaastra et al. (2008) shows the oxygen ion concentration versus temperature assuming collisional ionization equilibrium.

1.2.1 Spectral Observations of the Corona

Significant temperature differences among heavy ions, protons, and electrons in the corona have been shown via spectroscopic studies by Landi (2007) and Landi & Cranmer (2009). Spectroscopic observations are routinely used to discuss the abovementioned theories about explaining the energy deposition mechanism in the solar corona. Cranmer et al. (2015) lists a summary of the key ultraviolet spectroscopy observations relevant to the coronal heating and solar wind acceleration problem made by SoHO/UVCS. Figure 1.9 summarizes the current observational evidence for the presence of damped MHD turbulence in the solar corona, discussed in multiple studies using different instruments: Solar Ultraviolet Measurements of Emitted Radiation

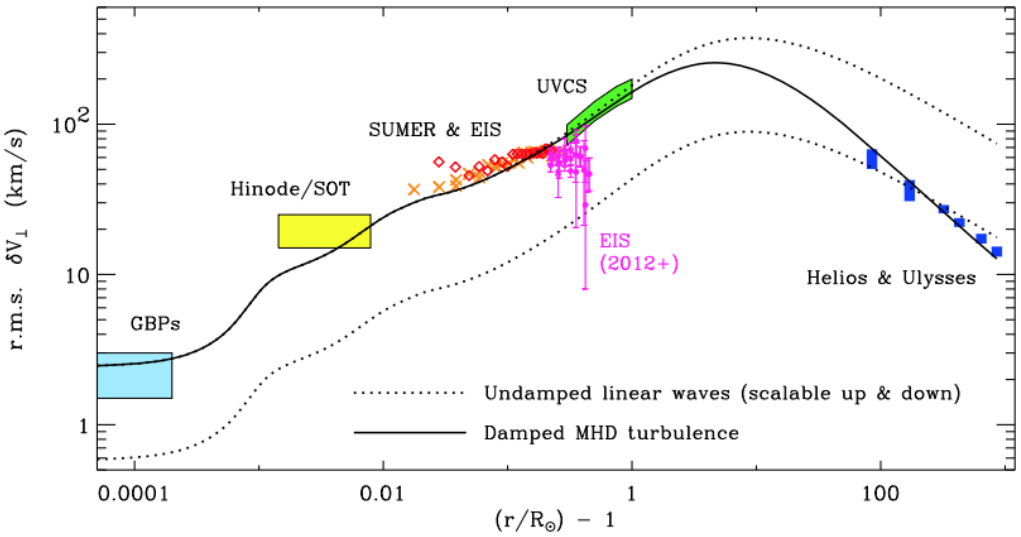

Figure 1.9: Figure 6. from Cranmer et al. (2017) shows the height dependence of transverse velocity fluctuations in coronal holes and the fast solar wind. The curves are from theoretical models, while colored indicators report observations. The two solid curves correspond to velocity fluctuations 0 km/s and 6 km/s, the dotted line is for velocity fluctuations with amplitude 3 km/s with dimensionless outer-scale length-scale normalization constant 0.35. For references and details see the original paper and Cranmer & van Ballegooijen (2005).

on board the Solar & Heliospheric Observatory (SoHO/SUMER; Wilhelm et al., 1995), EUV Imagig Spectrometer for Hinode (Hinode/EIS; Culhane et al., 2007a), Ultraviolet Coronagraph Spectrometer for SoHO (SoHO/UVCS; Kohl et al., 1995). While on one hand Hassler et al. (1990), Banerjee et al. (1998, 2009), Doyle et al. (1998), and McIntosh & De Pontieu (2012) showed that nonthermal motions from Alfvén waves could be identified in high resolution spectra, Patsourakos & Klimchuk (2006) and Patsourakos et al. (2014) found that synthetic line profiles generated by a nanoflare-heated corona cause modest line-broadening at lower than coronal temperatures but have stronger effects on hot plasmas, so that nanoflare heating would also leave a distinct line broadening effect depending on model parameters. MHD waves propagating in coronal holes have been observed both in narrow-band images (mostly in the EUV and visible range) and in spectroscopic data (Jess et al.,

2009; Banerjee et al., 2011).

Using spectroscopic observations, it is a common technique to measure the effective line width, which includes both thermal and nonthermal motions from observed spectral lines, and estimate wave energy deposition based on the change of the line width with radial distance. With this technique, Gupta et al. (2010) found spectroscopic evidence of wave propagation from an on-disk region into the off-limb corona using Hinode/EIS and SoHO/SUMER coronal-hole observations. Banerjee et al. (1998, 2009) and Doyle et al. (1998) found in both Hinode/EIS and SoHO/SUMER observations that the nonthermal velocity is inversely proportional to the square root of electron density, and concluded that undamped, radially propagating Alfvén waves responsible for the velocity profile and that the wave energy of the Alfvén waves is sufficient to drive the observed high-speed solar wind. Harrison et al. (2002) found evidence of wave damping in closed-loop regions of the quiet Sun in off-limb observations by the Coronal Diagnostic Spectrometer on board SoHO (CDS/SoHO Harrison et al., 1995). Later Bemporad & Abbo (2012), and Hahn et al. (2012) found evidence of significant Alfvén-wave damping in the low corona (up to about 0.4 solar radii off-limb) in coronal hole measurements by Hinode/EIS. While Gupta (2017) showed that wave damping is present in both active regions and quiet-Sun observations with a possible temperature dependence, Hahn & Savin (2014) argued that wave damping might be more dependent on global magnetic-loop properties (such as length of the loop) than local collisions, based on combining the PFSS model (Schatten et al., 1969; Schrijver & De Rosa, 2003) with Hinode/EIS observations of quiet Sun regions. Effective velocity (the root mean square of thermal and nonthermal velocities, Equation 3.17) measurements inside high-temperature loops of active regions have shown no trend relative to the observed temperature, suggesting neither nanoflare nor Alfvén wave heating is consistent with observations (Brooks & Warren, 2016).

Derived quantities such as emission measure and differential emission measure

(EM and DEM) are commonly used to differentiate among coronal heating theories (Parker, 1988; Hirayama, 1974; Fletcher et al., 2011; Hannah et al., 2011). An example of a coronal disk DEM is shown in Figure 1.10. Klimchuk (2017) showed that different nanoflare occurrence frequencies provided different power-law distributions in DEM curves, and his comparison with observations lent support to nanoflare heating theories, (see Figure 1.11).

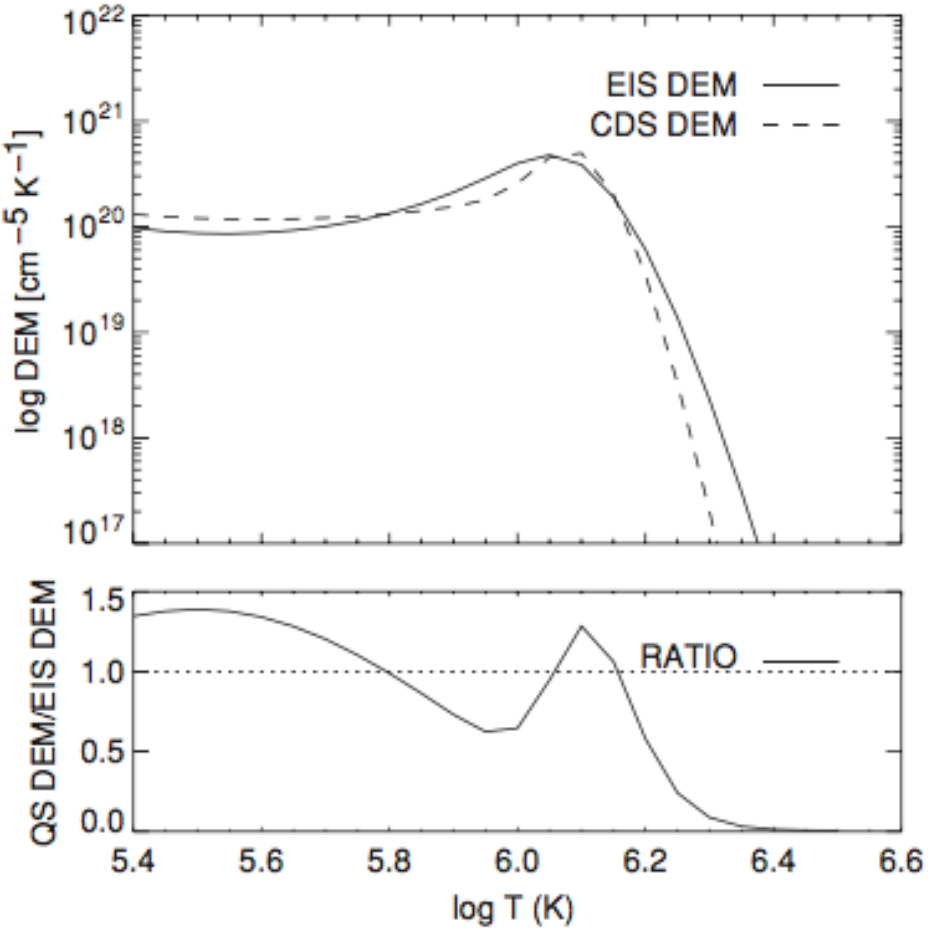

Figure 1.10: Upper panel (from Figure 4 of Brooks et al., 2009) is a DEM solution based on Hinode/EIS quiet Sun measurements of the coronal disk. This DEM is the representative quiet-sun DEM in the SolarSoft CHIANTI package. The dashed line shows a previously derived quiet-corona DEM (Brooks & Warren, 2006), and the lower panel shows their ratio.

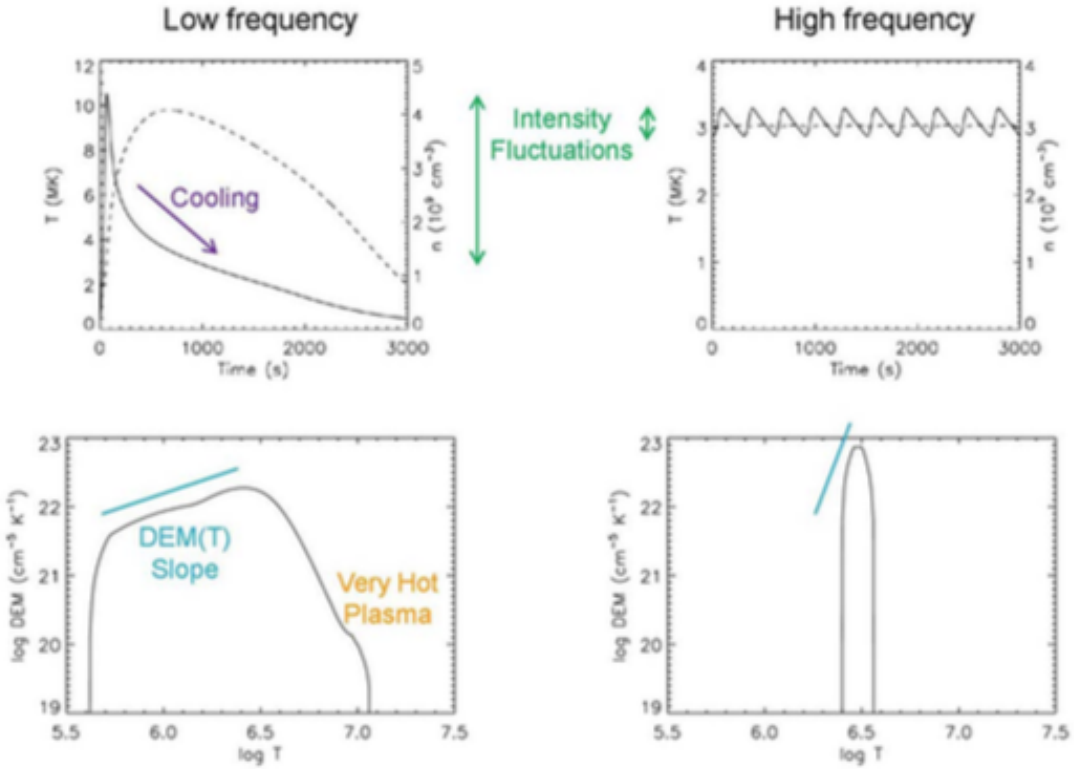

Figure 1.11: Figure 1 from Klimchuk (2017) shows the predicted DEM response to low- and high-frequency nanoflares, arguing that the cool side of the DEM function is generated by impulsive rather than gradual heating mechanism.

1.2.2 Observing the Alfvén-Wave Turbulence in the Solar Wind

The history of Alfvén-wave turbulence in the solar wind dates back to the work of Coleman (1968), who showed that turbulence is important near 1 AU based on measurements of Mariner 2. Alfvén waves were included in the early solar wind models of Belcher (1971) and Alazraki & Couturier (1971). While in the former models the Alfvén waves only propagated outwards away from the Sun, later on it was realized that outward propagating low-frequency Alfvén waves are partially reflected by the density gradients in the solar atmosphere, producing waves propagating in opposite direction (see, e.g., Heinemann & Olbert, 1980; Matthaeus et al., 1999; Dmitruk et al., 2002; Verdini & Velli, 2007; Cranmer, 2010; Chandran et al., 2011). Counter-

propagating waves are essential for generating an incompressible cascade (Velli et al., 1989) and hence for coronal heating. De Pontieu et al. (2007) showed via Hinode observations that there is sufficient energy in the chromospheric magnetic-field fluctuations to heat the solar corona and maintain temperatures at 1 MK. McIntosh et al. (2011) subsequently showed, using Solar Dynamics Observatory (SDO) data, that these waves are omnipresent in the transition region and lower corona. DeForest et al. (2016) used the Inner Heliospheric Imager instrument on board the Solar-Terrestrial Relations Observatory (STEREO/HI1) and found observational features compatible with the onset of magnetohydrodynamic instabilities leading to a turbulent cascade in the low corona. Numerical simulations have been used to interpret observations of nonthermal velocity measurements. For example, Zaqarashvili et al. (2006) explained the observed wave damping at about 0.2 solar radii with energy conversion from Alfvén to ion-acoustic waves, using MHD simulations.

1.3 MHD Solar Corona Model

"All models are wrong but some are useful" is one of the most common aphorisms about (statistical) models, originating from mathematician-statistician Box (1979). Solar models are the heart of space-weather predictive capabilities, as the Sun is the source and driver of all space weather events within the heliosphere. This section shows a way the complexity of the corona can be modeled using the magnetohydrodynamic approach.

Magnetohydrodynamics (MHD) combines hydrodynamics and magnetism when describing the plasma state and motion at a macroscopic level. This description implies that the plasma is fully ionized and in ionization equilibrium, charge-neutral, and the particle velocities are basically Maxwellians. In the simplest case we can assume that resistivity is insignificant, and we describe the plasma with the ideal MHD equations. Because of the limitation of space we will describe the governing

equations of the Michigan Solar Corona Model in relation to the ideal MHD equations, focusing on the physical meaning of the introduced extra terms. The coronal model we are going to use here is the Alfvén Wave Solar atmosphere Model (AWSOM, Sokolov et al., 2013; van der Holst et al., 2014), which is part of the Space Weather Modeling Framework (SWMF, Tóth et al., 2012), that has been successfully used to model solar wind plasma from the chromosphere to beyond Mars for space weather purposes, and for studying both quiet (Huang et al., 2012; Jin et al., 2012; Nuevo et al., 2013) and dynamic (Jin et al., 2013, 2017b,a; Szente et al., 2017) processes on the Sun, using the Block Adaptive Tree Solar-wind Roe-type Upwind Scheme (BATS-R-US).

The conservation of mass is expressed via the continuity equation (Equation 1.2): the mass within a volume element can change only by mass flux across the surface of the volume element or by source/sink terms within the element. The source/sink term on the right hand side of the equation is zero.

$$\frac{\partial \rho}{\partial t} + \nabla \cdot (\rho \mathbf{u}) = 0, \tag{1.2}$$

where ρ is the mass density and $\mathbf{u}$ is the bulk speed of the plasma.

The second equation is the equation of plasma motion (Equation 1.3),

$$\rho \frac{D\mathbf{u}}{Dt} = \mathbf{J} \times \mathbf{B} - \nabla \cdot \mathbf{P}, \tag{1.3}$$

where $\frac{D\mathbf{u}}{Dt} = \frac{\partial}{\partial t} + \mathbf{u} \cdot \nabla$ is the convective derivative, $\mathbf{J}$ is current density, $\mathbf{B}$ is magnetic field, and P is the pressure tensor.

In the case of the solar wind description, we have to take into account multiple deviations from ideal MHD:

1. The electron and proton temperatures are significantly different.

2. The solar gravitational field is present.

3. Alfvén waves act as an extra pressure term on the plasma motion.

The momentum equation neglecting the proton temperature anisotropy within the two-temperature AWSoM model is:

$$\frac{\partial(\rho\mathbf{u})}{\partial t}+\nabla\cdot\left(\rho\mathbf{uu}-\frac{\mathbf{BB}}{\mu_0}\right)+\nabla\left(p_p+p_e+\frac{B^2}{2\mu_0}+p_A\right)=-\rho\frac{GM_\odot}{r^3}\mathbf{r}, \tag{1.4}$$

in which p_p and p_e are the proton and electron pressures, respectively. $p_A=\frac{1}{2}\left(\omega_+ + \omega_-\right)$ is the Alfvén wave pressure, expressed with the wave energy densities $\omega_\pm$, where $+$ direction corresponds to outward- and $-$ direction to inward propagating waves. μ_0 is the permeability of vacuum, $\mathbf{r}$ is the position vector relative to the center of the Sun, G the gravitational constant, and $M_\odot$ the solar mass. In the case of temperature anisotropy, we have an extra term due to the anisotropy. The momentum equation (Equation 1.5) for the three-temperature (parallel and perpendicular proton temperatures and isotropic electron temperature) AWSoM model is:

$$\frac{\partial(\rho\mathbf{u})}{\partial t}+\nabla\cdot\left[\rho\mathbf{uu}+\left(P_{p\parallel}-P_{p\perp}\right)\mathbf{bb}-\frac{\mathbf{BB}}{\mu_0}\right]+\nabla\left(P_{p\perp}+P_e+\frac{B^2}{2\mu_0}+P_A\right)= -\rho\frac{GM_\odot}{r^3}\mathbf{r}, \tag{1.5}$$

where $\mathbf{b}=\mathbf{B}/B$. The model defines the pressure-temperature relationship as follows:

$$p_{e,p}=N_{e,p}k_BT_{e,p} \tag{1.6}$$

for the two-temperature case, and

$$p_{p\parallel}=N_pk_BT_{p\parallel}, \tag{1.7}$$

for the three-temperature case. N is number density, T is temperature, and the

subscripts e, p, $p\parallel$ correspond to electron, proton, parallel-proton quantities.

The energy equation for the ideal MHD description is:

$$\frac{\partial}{\partial t}\left(\frac{P}{\gamma-1}+\frac{\rho u^2}{2}+\frac{\mathbf{B}^2}{2\mu_0}\right)+\nabla\cdot\left[\left(\frac{\rho u^2}{2}+\frac{\gamma p}{\gamma-1}+\frac{B^2}{\mu_0}\right)\mathbf{u}-\frac{\mathbf{B}(\mathbf{u}\cdot\mathbf{B})}{\mu_0}\right]= -\rho\frac{GM_\odot}{r^3}\mathbf{r}\cdot\mathbf{u}. \quad (1.8)$$

When shocks are present in the solar wind solution, it is advisable to solve the energy equation instead of the pressure equations to obtain proper jump conditions at the shock front. The energy conservation is described in Equation 1.9 and Equation 1.10 for the two-temperature model, and Equation 1.11, Equation 1.12 and Equation 1.10 for the three-temperature model. The energy change within a volume element is due to energy flux through the surface of the volume element, and also to source terms (right side of the equation) such as heat conduction, heat exchange between the species (proton, electron) and gravitational energy. Thus

$$\frac{\partial}{\partial t}\left(\frac{P_p}{\gamma-1}+\frac{\rho u^2}{2}+\frac{\mathbf{B}^2}{2\mu_0}\right)+\nabla\cdot\left[\left(\frac{\rho u^2}{2}+\frac{\gamma P_p}{\gamma-1}+\frac{B^2}{\mu_0}\right)\mathbf{u}-\frac{\mathbf{B}(\mathbf{u}\cdot\mathbf{B})}{\mu_0}\right]= -(\mathbf{u}\cdot\nabla)\left(p_e+p_A\right)+\frac{N_p k_B}{\tau_{ep}}\left(T_e-T_p\right)+Q_p-\rho\frac{GM_\odot}{r^3}\mathbf{r}\cdot\mathbf{u}, \quad (1.9)$$

in which the polytropic index is $\gamma = 5/3$, N_p is the proton number density, T_p and T_e are the proton and electron temperatures, k_B is the Boltzmann constant, Q_p is heating function of protons based on Alfvén-wave damping, and τ_{ep} is the relaxation time of electron-ion collisions.

The time evolution of the electron pressure is given by:

$$\frac{\partial}{\partial t}\left(\frac{P_e}{\gamma-1}\right)+\nabla\cdot\left(\frac{P_e}{\gamma-1}\mathbf{u}\right)+P_e\nabla\cdot\mathbf{u}= -\nabla\cdot\mathbf{q}_e+\frac{N_p k_B}{\tau_{ep}}\left(T_p-T_e\right)+Q_e-Q_{\mathrm{rad}}, \quad (1.10)$$

where $\mathbf{q_e}$ is the electron heat conduction, which is assumed collisional near the Sun and collisionless far away from the Sun; Q_e is the heating function of electrons due to Alfvén-wave damping; and $Q_{\rm rad}$ is the radiative loss term.

For the three-temperature case, in practice we solve for the full average pressure and for the parallel proton pressure component, and calculate the perpendicular component as $p_\perp = \left(3p_p - p_{p\parallel}\right)/2$. The equations for the average and parallel proton pressures are

$$\frac{\partial}{\partial t}\left(\frac{P_p}{\gamma-1}+\frac{\rho u^2}{2}+\frac{\mathbf{B}^2}{2\mu_0}\right)+\nabla\cdot\left[\left(\frac{\rho u^2}{2}+\frac{p_p}{\gamma-1}+\frac{B^2}{\mu_0}\right)\mathbf{u}+\mathbf{P}\cdot\mathbf{u}-\frac{\mathbf{B}\left(\mathbf{u}\cdot\mathbf{B}\right)}{\mu_0}\right]= -\left(\mathbf{u}\cdot\nabla\right)\left(p_e+p_A\right)+\frac{N_p k_B}{\tau_{ep}}\left(T_e-T_p\right) +Q_p-\rho\frac{GM_\odot}{r^3}\mathbf{r}\cdot\mathbf{u}, \tag{1.11}$$

$$\frac{\partial p_{p\parallel}}{\partial t}+\nabla\cdot\left(p_{p\parallel}\mathbf{u}\right)+2p_{p\parallel}\mathbf{b}\cdot\left(\nabla\mathbf{u}\right)\cdot\mathbf{b}= \frac{\delta p_{i\parallel}}{\delta t}+2\frac{N_p k_B}{\tau_{ep}}\left(T_e-T_{p\parallel}\right)+2Q_{p\parallel}, \tag{1.12}$$

where $\mathbf{P}_p = p_{p\parallel}I+\left(p_{p\parallel}-p_{p\perp}\right)\mathbf{bb}$ is the proton pressure tensor, $Q_{p\parallel}$ is the heating function for the parallel proton temperature, and the source term $\frac{\delta p_{p\parallel}}{\delta t}$ is added for the relaxation of the proton pressure anisotropy to a stable state when the firehose, mirror, and proton cyclotron instabilities occur (Meng et al., 2015).

Finally we solve the wave energy density equation

$$\frac{\delta\omega_\pm}{\delta t}+\nabla\cdot\left[\left(\mathbf{u}\pm\mathbf{V}_A\right)\omega_\pm\right]+\frac{\omega_\pm}{2}\left(\nabla\cdot\mathbf{u}\right)=\mp R\sqrt{\omega_-\omega_+}-\Gamma_\pm\omega_\pm, \tag{1.13}$$

where $\mathbf{V}_A = \mathbf{B}/\sqrt{\mu_0\rho}$ is the Alfvén speed, R is the reflection coefficient (mostly due to the field-aligned component of the Alfvén speed gradient), and Γ is the dissipation rate, for which we take the phenomenological description of Dmitruk et al. (2002).

The + subscript represents Alfvén waves propagating in the direction parallel to the magnetic field, while − is for the Alfvén waves propagating antiparallel to **B**.

The MHD equations are closed with Faraday's law

$$\nabla \times \mathbf{E} = -\frac{\partial \mathbf{B}}{\partial t}, \tag{1.14}$$

where **E** is the electric field, expressed from Ohm's law as

$$\mathbf{E} = -\mathbf{u} \times \mathbf{B}, \tag{1.15}$$

Ampère's law is

$$\nabla \times \mathbf{B} = \mu_0 \mathbf{J}, \tag{1.16}$$

where the displacement current is neglected. Finally, the magnetic field is divergence free:

$$\nabla \cdot \mathbf{B} = 0, \tag{1.17}$$

More on the coronal model is discussed in Chapter 2.

1.4 Outline

With the MHD description of the plasma, it is possible to model both the dynamic and steady state solar corona, producing synthetic observations to analyse and further evaluate observations, using both in-situ plasma measurements and imaging-spectroscopic data. Solar corona models used for space weather modeling use photospheric magnetograms for boundary conditions. Such models have been studied and evaluated on a regular basis. Lately Jian et al. (2015) published about the per-

formance of these models in predicting the plasma conditions at Earth. One of the many results of this study is that the magnetic boundary conditions are of critical importance for solar wind models (see works from Riley et al., 2015; Tlatov et al., 2016; Linker et al., 2017).

In Chapter II we explain what coronal jets are and why they are interesting. We describe the jet model embedded within the realistic global corona and solar wind two-temperature AWSoM model. In Chapter III we discuss the physics, algorithm, and implementation of the SPECTRUM code, which we developed as a post-processing tool for synthetic spectral calculations within the SWMF. SPECTRUM can not only help to understand spectral observations better, but also can serve as a new model validation tool for solar (or even stellar) corona models.

CHAPTER II

Coronal Jet Modeling

2.1 Introduction

Jets are ubiquitous and are seen in X-rays followed by emission in cooler EUV bands, as observed with multiple instruments onboard Yohkoh (Ogawara et al., 1991), the Solar and Heliospheric Observatory (SoHO; Domingo et al., 1995), the Transition Region and Coronal Explorer (TRACE; Handy et al., 1999), Hinode (Kosugi et al., 2007), the Solar Terrestrial Relations Observatory (STEREO; Kaiser et al., 2008), and the Solar Dynamics Observatory (SDO; Pesnell et al., 2012). Their typical sizes range from 10^2 to 10^4 km, outflow speeds from 10^1 to 10^3 km s^{-1}, and lifetimes from 10^{-1} to 10^1 hr (Shimojo et al., 1996; Savcheva et al., 2007; Shibata et al., 2007). They have been observed at multiple wavelength bands – visible (Bohlin et al., 1975), UV (Brueckner & Bartoe, 1983), EUV, and X-ray (Shibata, 1982) – corresponding to electron temperatures ranging from about 10^4 K to 10^7 K. Jets are similar to spicules in size, also both contribute to the quiet corona. While spicules contribute through slow plasma outflow at about the ion acoustic speed, jets exhibit eruptive plasma injections with fast plasma outflow at about the Alfvén speed over longer periods of time. This chapter focuses exclusively on jets, which are distinct from spicules. The constant presence of jets raises the question of their contribution to the solar wind plasma and coronal heating. First hydrodynamic (Shibata, 1982), later

magnetohydrodynamic models complemented the increasingly detailed solar disk and in-situ observations, and have informed us of the fine structure of jets, which also raises questions about observable traces they leave in the outer coronal plasma. Many models have attempted to reproduce and quantitatively predict jet properties, to estimate their contribution to coronal heating and the solar wind, and identify their observable signatures in the extended solar atmosphere. However, even the most advanced models (3D MHD models for instance, see Section 2.2) studied jets without considering the background solar wind plasma interaction with the jet. Modeling the jet in a complete solar corona instead of a local box, allows to estimate the jet contribution to the global solar wind.

In this chapter, we address these two limitations and discuss two 3D MHD jet simulations realized within the Alfvén Wave Solar Model (AWSoM), that provides realistic atmospheric stratification, solar wind acceleration and turbulence-based coronal heating (Sokolov et al., 2013; van der Holst et al., 2014). We use the simulation results to give quantitative estimations of the significance of jets' contributions to the global solar corona and to suggest observables that can be investigated with the upcoming Parker Solar Probe mission.

After a short review of jet properties in Section 2.2, Section 2.3 describes the simulation model and Section 2.4 presents the results. We compare synthetic line-of-sight images to observations in Section 2.5 as model validation. Finally, the findings are summarized in Section 2.6. The contents of this chapter have been published in Szente et al. (2017).

2.2 Jet Observations and Models

Energy deposition in the chromospheric plasma results in various types of jets, depending on the vertical location of the process (Sterling et al., 1994). The first models of jets were hydrodynamic; based on observations Shibata (1982) classified

jets into two categories based on the location of their bright points: the 'crest-shock' type jets have bright points at the low corona's low density plasma and are driven by shock waves. These jets can be observed in the EUV bands. The second type is the 'shock-tube' jet, whose bright point is at the middle-upper chromosphere, and its driver is a large pressure gradient. Only this jet type is visible in both Hα lines (due to its higher density) and the accompanying X-ray flares.

Having more detailed observations from Yohkoh's Soft X-ray Telescope (Yohkoh/SXT; Tsuneta et al., 1991), jets were distinguished by the plasma temperature at which they have been observed. With Yohkoh/SXT, Shibata et al. (1994) observed various jets in active regions, emerging flux regions, and at X-ray bright points of their flaring footpoints. Distinguishing between superhot (up to about 10^7 K) and hot (about 10^6 K) plasma ejections, the terms coronal X-ray and EUV jets were introduced. Jets were also related to magnetic field topology changes. Studying EUV jets, Moschou et al. (2013) found that in many cases the ejected material falls back due to its low velocity. They also inferred untwisting magnetic flux and reported recurrence of ejections in multiple cases. Shibata et al. (1992) suggested that magnetic reconnection is the driver of jets. Several studies have also suggested that X-ray jets are driven by magnetic reconnection events, either through spectroscopic observations (Kim et al., 2007) or multi-spacecraft observations (Madjarska, 2011). Evidence for jet formation by reconnection between twisted and untwisted magnetic loops in open- and closed-field regions was observed by Yohkoh/SXT. Moreover, rotating motions, spinning and unwinding, and magnetic flux cancellation were observed in multiple bands; for example Sterling et al. (2010) used observations in Ca II H and EUV bands taken by Hinode's and STEREOs' instruments: the Solar Optical Telescope (Hinode/SOT; Tsuneta et al., 2008), the X-ray Telescope (Hinode/XRT; Golub et al., 2007), the EUV Imaging Spectrometer (Hinode/EIS; Culhane et al., 2007a), and the Extreme Ultraviolet Imager (STEREO/EUVI; Wuelser et al., 2004),

and later Chen et al. (2012) used observations taken by the Atmospheric Imaging Assembly onboard SDO (SDO/AIA; Lemen et al., 2012). In a study of nine jets observed by Yohkoh/SXT, the Mees CCD Imaging Spectrograph (Penn et al., 1991), and the Imaging Vector Magnetograph at the Mees Solar Observatory (Mickey et al., 1996), Canfield et al. (1996) found that X-ray jets and Hα surges are associated with moving magnetic bipoles. They reported spinning motion in all observed surges, consistent with the untwisting of magnetic field. They also discussed the morphology of jets, including the upflow and downflow of reconnection exhaust. Evidence of helical structures within jets has been revealed by stereoscopic observations by the STEREO spacecraft (Patsourakos et al., 2008). Overall both EUV and X-ray jets are suggested to be produced by small-scale reconnection events (Chifor et al., 2008a). These multiple wavelength observations showed not only the recurrent reconnection, but also the mixing of dense, cold plasma with tenuous, hot plasma. They also showed that, within the jet plasma, the density increased with increasing upflow velocity.

Being closely tied to the magnetic field evolution, another common classification of X-ray jets was based on the relative direction of the coronal field the flux emerges into: in the cases of nearly horizontal fields, the jet is a 'two-sided loop' type, while the ones emerging into vertical or moderately tilted fields are 'anemone' jets (Shibata et al., 1994). Shimojo et al. (1996) suggested that the anemone morphology is due to the emergence of a bipole magnetic structure into the open flux, based on a statistical study of a hundred X-ray jets. The different jet types seemed to relate to each other in morphology and regarding their driving forces. Shibata et al. (2007) observed 59 jets with Ca II H broadband filters, which were called 'Ca jets.' They estimated that during the one hour Hinode/SOT observation, the jet did not provide sufficient energy flux to heat the ambient corona. The inferred magnetic structures of these anemone-shaped jets were assumed to be due to an opposite-polarity magnetic dome being reconnected with the ambient open field. The drivers of these jets were the

reconnecting fields at the footpoints of the dome. A similar driver mechanism was suggested in jet models of different sizes and vertical locations: coronal X-ray jets are the largest, followed by EUV jets, and then photospheric nanoflares. As Nishizuka et al. (2011) pointed out, the chromospheric and coronal anemone jets show very similar dynamics.

Jets are often observed with accompanying bright spots in the local plasma. The appearance and reappearance of bright points along with jets was studied from multiple aspects. Kamio et al. (2007) and Pucci et al. (2012) showed that jets and bright points are strongly correlated and concluded that jets are results of magnetic topology change due to reconnection. Kamio also found evidence of up- and downflows as evidence of reconnection outflow. Coronal-hole bright points and a particular jet were studied using Hinode/EIS observations by Doschek et al. (2010). They found a Doppler shift in the Fe XII line indicating flows toward the observer; the jet speed was measured to be about 15-20 km s^{-1}, and the speed decreased to zero toward the base. The maximum observed temperature was about 1.4×10^6 K, decreasing with height. The velocity and temperature profiles with height suggested that heating occurred at the base of the jet. Expanding bright loop structures prior to the jet onset were observed by Singh et al. (2012). Chromospheric anemone jets showed intermittent and recurrent ejections, while some also showed signs of current-sheet formation or quasi-periodicity. Shimojo et al. (2007) discussed that jets along closed magnetic field lines might cause brightening at the other end of the loop structure. Having observations of smaller loops, they were able to measure the speed of the hot plasma flow along the loop structure that causes the brightening at the other footpoint. In addition, they remarked on the fine structures of X-ray jets in the Hinode/XRT observations: the majority of observed jets appeared after a brightening which was followed by a loop expansion, possibly due to kinking. A statistical study of 100 jets observed during

a 6 month period of 1991-1992 with Yohkoh/SXT by Shimojo et al. (1996) showed that the majority of jets included footpoint brightening: 27% of the bright regions were clearly above the actual footpoints, which suggested that the reconnection and localized plasma heating take place around the dome of closed field lines at the base of the jet.

Having multiple detailed observations with instruments aboard Hinode and SDO, the jet categorization moved forward: Moore et al. (2010, 2013) set up a classification based on morphology, phase, and magnetic reconnection scenario. They concluded that there are two basic types of X-ray jets: standard and blowout jets. They occur approximately in equal numbers, but standard jets are dimmer, and so they are more likely to be missed during observations. Blowout jets show lateral expansion of cool material, standard jets do not. Also blowout jets have a more complex structure and are accompanied by stronger brightenings than standard jets. Standard jets consist of one spire, usually having the shape of an inverted Y, without any strong X-ray brightening or lateral expansion.

Pucci et al. (2013) further analyzed in detail the differences (velocity, temperature, magnetic field strength), and similarities (recurrent reconnection events) between standard and blowout jets. Both types show axial rotation and are produced by bipolar magnetic fields emerging into the ambient field. Also, an observational study by Adams et al. (2014) proved that blowout jets can occur with flux convergence rather than emergence, and that a jet structure can be produced by destabilization along the polarity inversion line. This blowout eruption is like a filament eruption similar to CMEs and flares. They postulated that reconnection in the blowing-out arcade field constructs long EUV loops, that are identified as new types of blowout jets.

Due to the nature of line-of-sight observations many non-jet events may produce jet-like features in the field of view. Madjarska et al. (2007) showed that jet-like features may be produced by fast field-aligned flows, but by using spectroscopic tools it is possible to clearly describe the ongoing dynamics and distinguish such flows from jet events. Similarly, apparently helical, twisting structures in prominences were interpreted by Okamoto et al. (2010) and Li et al. (2012) to be in the form of jets. In many cases, the apparent twist might be created by overlapping field lines with loop-like geometries (Panasenco et al., 2014).

Another open question is the estimation of jet contribution to the solar wind plasma. Wang et al. (1998) suggested that jets occurred more often than observed, and that it is not clear how to estimate their significance. Similarly, observations of jets from SoHO's Large Angle Spectrometric COronagraph C2 (SoHO/LASCO; Brueckner & Bartoe, 1983) were analyzed by Corti et al. (2007) to find correlating Ulysses plasma measurements. Due to the very active corona, it was not easy to correlate the disturbances caused by the jet to Ulysses observations. They found that cold jets, initiated by reconnection of closed loops with the open background field, preserved the temperature signatures during propagation, and that the ejected mass is above 10^{11} g, which means that these jets are observable by available coronagraphs, such as SoHO/LASCO (see for example Kumar et al., 2018).

Numerical models have been used to study the morphology and quantitatively estimate the properties of jets for decades. Recently Cranmer et al. (2015) have shown in the context of a reduced MHD simulation that Alfvénic turbulence within an expanding, circular fluxtube can cause signatures in the coronal plasma that correspond to Type II spicules or network-jets observed by IRIS (De Pontieu et al., 2014). In

their model, chromospheric Alfvén waves develop into compressive waves that produce the shocks, driving the dense plasma from the chromospheric and transition regions to heights of thousands of kilometers in the corona. With a 1D hydrodynamic study, Sterling et al. (1993) discussed the many possible outcomes of energy deposition, depending on the rate and vertical height, and gave descriptions of the drivers of the emerging plasma ejections. They also predicted the bands to look for observable brightening corresponding to the location of deposition. Using 2D resistive MHD models with uniform gravitational field, Yokoyama & Shibata (1995) showed that cool Hα surges and hot X-ray jets can both originate from microflares (see also Yokoyama & Shibata, 1996). They also found that all physical and morphological characteristics were reproducible for both two-sided loop and anemone types of jets. In their model, fast mode shocks were produced at the reconnection site with the ambient field, which drove the jet further. Later, also with a 2D resistive MHD model with a uniform gravitational field, Nishizuka et al. (2008) successfully reproduced anemone jet features observed by Hinode/SOT, Hinode/XRT and by TRACE at 195 Å. Using a 2.5D resistive MHD model with a uniform gravitational field, Yokoyama & Shibata (1999) estimated that only 3% of energy was stored as waves generated in the jet during the reconnection. In another 2.5D MHD study, Yang et al. (2013) showed that moving magnetic features can create chromospheric anemone jets, along with tearing instabilities and slow-mode shocks in them.

Using a fully 3D approach to flux emergence within an open-field region, Moreno-Insertis & Galsgaard (2013) produced blowout jets with a stratified background atmosphere starting with a twisted flux rope below the photosphere. The model used ideal gas and uniform heating approximations. They successfully reproduced the standard and blowout phases of a jet, as described by Moore et al. (2010, 2013, 2015). In a related study, the Block Adaptive Tree Solar-wind Roe-type Upwind Scheme (BATS-

R-US) (Powell et al., 1999; Tóth et al., 2012) was used for modeling jet formation by Fang et al. (2014) in a fully 3D ideal MHD setup. They simulated the emergence of a twisted flux rope into the ambient open field, and found that the coronal mass is increased by about 2% due to the mass injection through the jet. The generated upward flow was strongly dominated by the magnetic twist, while the downflow was simpler, but still correlated with the magnetic twist. They concluded that the upward motion was accelerated strongly by the Lorentz force, and that the Poynting flux in the corona was dominated by the twisting motion that coincided with the upward mass transport of dense plasma. The field-aligned thermal conduction also transported energy downward to the lower atmospheric regions, inducing further plasma release by evaporation.

An alternative mechanism for generating coronal jets was proposed on theoretical grounds by Antiochos (1990, 1996). He argued that the null-point 'anemone' topology of the source region would be susceptible to explosive magnetic reconnection that could drive the jet, even in regions where no new flux is emerging. This model has been investigated in a series of numerical simulations by Pariat et al. (2009, 2010, 2015, 2016) and Wyper et al. (2016); Karpen et al. (2017). In these studies, the closed magnetic flux of the jet source region is energized by slow footpoint motions that introduce twist and cause the volume of closed flux to become distended along the ambient open field. Eventually, the flux succumbs to an ideal kinking or toppling instability, which ruptures the separatrix surface and drives fast reconnection between the internal, twisted closed flux and the external, untwisted open flux. The transfer of twist to the external field initiates nonlinear Alfvén waves on the reconnected open field lines, which are trailed by outflows of dense plasma that constitute the jet. This mechanism has been shown to produce recurrent jets in response to continued slow footpoint driving (Pariat et al., 2010) and to spawn jets that propagate into

the outer corona when solar gravity, wind, and spherical expansion are taken into account, generating observationally confirmed turbulent signatures propagating into the solar wind (Karpen et al., 2017). Breakout jets with mini-filaments have been successfully modeled with the above mentioned magnetic topology by Wyper et al. (2017, 2018), providing explanation of jet observations by Sterling et al. (2015) and Adams et al. (2014). However, these previous simulations assumed either adiabatic or isothermal evolution of the plasma, which is not adequate for predicting the density and temperature signatures of coronal jets observed on the Sun, even though they successfully predict the Alfvénic jet speeds and turbulent signature propagating into the solar wind.

The objective of this chapter is to remedy this omission by using a two-temperature model of the global corona that includes the complexities of heat conduction, optically thin radiative losses, and background atmospheric heating due to Alfvén waves. This far more comprehensive model of the coronal thermodynamics is described in Section 2.3. We employ it to simulate the generation of coronal jets driven by slow footpoint motions at the chromosphere, in a manner analogous to that of Pariat et al. (2009), as detailed in Section 2.4.

2.3 Simulation Description

2.3.1 Coronal Model

The computational model is based on the BATS-R-US code that is used as the Solar Corona component of the Space Weather Modeling Framework (SWMF) developed at the University of Michigan (Tóth et al., 2012). The fully self-consistent, two-temperature (electrons and protons) Alfvén Wave Solar Model (AWSoM; van der Holst et al., 2014) implemented in BATS-R-US is used in this chapter. In this

model, the corona and solar wind are heated by low-frequency Alfvén wave turbulence, and the Alfvén-wave pressure is the main driver of the fast solar wind outflow. The governing equations of the AWSoM model are the following:

$$\frac{\partial \rho}{\partial t} + \nabla \cdot (\rho \mathbf{u}) = 0, \tag{2.1}$$

$$\frac{\partial (\rho \mathbf{u})}{\partial t} + \nabla \cdot \left(\rho \mathbf{u}\mathbf{u} - \frac{\mathbf{B}\mathbf{B}}{\mu_0} \right) + \nabla \left(P_p + P_e + \frac{B^2}{2\mu_0} + P_A \right) = -\rho \frac{GM_\odot}{r^3} \mathbf{r}, \tag{2.2}$$

$$\frac{\partial \mathbf{B}}{\partial t} - \nabla \times (\mathbf{u} \times \mathbf{B}) = 0, \tag{2.3}$$

$$\begin{aligned} \frac{\partial}{\partial t} \left(\frac{P_p}{\gamma - 1} + \frac{\rho u^2}{2} + \frac{\mathbf{B}^2}{2\mu_0} \right) + \nabla \cdot \left[\left(\frac{\rho u^2}{2} + \frac{\gamma P_p}{\gamma - 1} + \frac{B^2}{\mu_0} \right) \mathbf{u} - \frac{\mathbf{B}(\mathbf{u} \cdot \mathbf{B})}{\mu_0} \right] = \\ -(\mathbf{u} \cdot \nabla)(P_e + P_A) + \frac{N_p k_B}{\tau_{ep}} (T_e - T_p) + Q_p - \rho \frac{GM_\odot}{r^3} \mathbf{r} \cdot \mathbf{u}, \end{aligned} \tag{2.4}$$

$$\begin{aligned} \frac{\partial}{\partial t} \left(\frac{P_e}{\gamma - 1} \right) + \nabla \cdot \left(\frac{P_e}{\gamma - 1} \mathbf{u} \right) + P_e \nabla \cdot \mathbf{u} = \\ -\nabla \cdot \mathbf{q}_e + \frac{N_p k_B}{\tau_{ep}} (T_p - T_e) + Q_e - Q_{\rm rad}, \end{aligned} \tag{2.5}$$

$$\frac{\partial w_\pm}{\partial t} + \nabla \cdot [(\mathbf{u} \pm \mathbf{V}_A) w_\pm] + \frac{w_\pm}{2} (\nabla \cdot \mathbf{u}) = \mp \mathcal{R} \sqrt{w_- w_+} - \Gamma_\pm w_\pm. \tag{2.6}$$

Equation 2.1 is the continuity equation, where ρ is the mass density and $\mathbf{u}$ is the proton bulk velocity. The electron bulk velocity is assumed to be the same as the proton velocity. Equation 2.2 is the momentum equation in which $\mathbf{B}$ is the magnetic field, μ_0 is the vacuum permeability, $P_{e,p}$ are the isotropic electron and

proton pressures, P_A is the Alfvén-wave pressure

$$P_A = (w_+ + w_-)/2 \tag{2.7}$$

where $w_{+,-}$ are the parallel and antiparallel (relative to $\mathbf{B}$) propagating Alfvén-wave energy densities, G is the gravitational constant, $M_\odot$ is the solar mass, and $\mathbf{r}$ is the position vector originated from the solar center. Solar rotation is ignored. Equation 2.3 is the induction equation for ideal MHD. Equation 2.4 is the proton pressure equation: $\gamma = \frac{5}{3}$ is the polytropic index, N_p is the proton number density, k_B is the Boltzmann constant, τ_{ep} is the electron/proton temperature equilibration time due to Coulomb collisions, $T_{e,p}$ are the isotropic electron and proton temperatures, and Q_p is the proton heating function. Ideal equation of state for both electrons and protons is used: $P_{e,p} = N_{e,p} k_B T_{e,p}$. Equation 2.5 describes the evolution of electron pressure: $\mathbf{q}_e$ is the electron heat flux,

$$\mathbf{q}_e = f_S \mathbf{q}_{e,S} + (1 - f_S)\mathbf{q}_{e,H}, \tag{2.8}$$

where

$$f_S = \frac{1}{1 + (r/[5R_\odot])^2} \tag{2.9}$$

and

$$\mathbf{q}_{e,S} = -\kappa_e T_e^{5/2} \mathbf{b}\mathbf{b} \cdot \nabla T_e \tag{2.10}$$

is the Spitzer collisional heat flux and

$$\mathbf{q}_{e,H} = \frac{3}{2} \alpha p_e \mathbf{u} \tag{2.11}$$

is the Hollweg collisionless heat flux (Hollweg, 1978) with $\alpha = 1.05$, $\mathbf{b} = \mathbf{B}/B$ is the magnetic field unit vector, and $\kappa_e = 9.2 \times 10^{-12}\ \mathrm{W\,m^{-1}\,K^{-7/2}}$. With this description, the heat conduction is the Spitzer formulation in the dense lower corona and smoothly transitions to the collisionless regime of the upper corona at $r \approx 5R_\odot$. Additionally, Q_e is the electron heating function and Q_{rad} is the optically thin radiative energy loss,

$$Q_{\mathrm{rad}} = N_e N_p \Lambda(T_e), \tag{2.12}$$

where $\Lambda(T_e)$ is the radiative cooling function from CHIANTI 7.1 (Landi et al., 2013). Equation 2.6 describes the evolution of the Alfvén-wave energy densities $w_\pm$. $\mathbf{V}_A = \mathbf{B}/\sqrt{\mu_0 \rho}$ is the Alfvén speed, $\mathcal{R}$ is the reflection rate (see details in Section 2.4.8), and $\Gamma_\pm$ is the dissipation rate (also discussed in Section 2.4.8). The $+$ and $-$ subscripts correspond to waves propagating parallel and antiparallel, respectively, relative to the local magnetic field direction. For the details of partitioning the Alfvén-wave heating between the electrons and protons (Q_e and Q_p), see Chandran et al. (2011) or the summary presented in van der Holst et al. (2014).

The equations above lack physical resistivity and viscosity, because in a global model it is not possible to resolve the scales corresponding to physical resistivity with the computational resources. The Spitzer resistivity in the chromospheric boundary plasma is of the order of $10^{-4}\ \Omega$m. With a time step of 0.04 s, the physical resistivity scales are on the order of meters, which is not feasible to resolve.

Instead of physical viscosity and resistivity, the model relies on numerical viscosity and resistivity that result from the numerical diffusion terms that stabilize the solution as well as ensure that fast reconnection is possible (and occurs) in the simulation. Away from discontinuities the numerical diffusion terms are greatly reduced

as the solution is spatially 2nd order accurate. Numerical diffusion terms have no significant effect on the solution in these smooth regions, because larger-scale structures are well-resolved on the grid, so that the diffusion time scale is long compared to the dynamic time scale. Near discontinuities, such as shock waves and current sheets, the code relies on the numerical dissipation and the conservation laws to get the right solution. For example, at reconnection regions, where the current sheet steepens to a discontinuity at the level of the local grid resolution, the scheme switches to first order, and the anti-parallel components of the magnetic field dissipate at a rate that is some fraction of the local fast magnetosonic speed. While it is difficult to resolve the actual scales of the viscous shock layers or the current sheet width due to resistivity, the solution can still be reasonably accurate on larger scales. MHD models with numerical viscosity and resistivity have successfully simulated numerous space plasma systems with shocks and reconnection sites (see for instance the review by Tóth et al., 2012)

In this numerical scheme, the dissipated kinetic energy at shocks is being delivered to proton heating only. Another consequence of the numerical scheme is that, for magnetic reconnection, the dissipated magnetic energy is being delivered only to the protons due to the conservation of the total energy that includes the proton thermal energy density. This is contrary to a reconnection based on resistivity, which would heat the electrons. In this model, the electron thermal energy is calculated from Equation 2.5, which involves adiabatic heating, heat conduction, and proton-electron heat exchange. That the protons are heated instead of the electrons is justified as long as the Coulomb colllisional energy exchange equilibrates the electron and proton temperatures at a fast enough rate. In Figure 2.1, we show in a meridional slice through the jet region the time scale of the collisional heat transfer between the electrons and protons for the steady state at time $t = 0$ s. This shows that this time

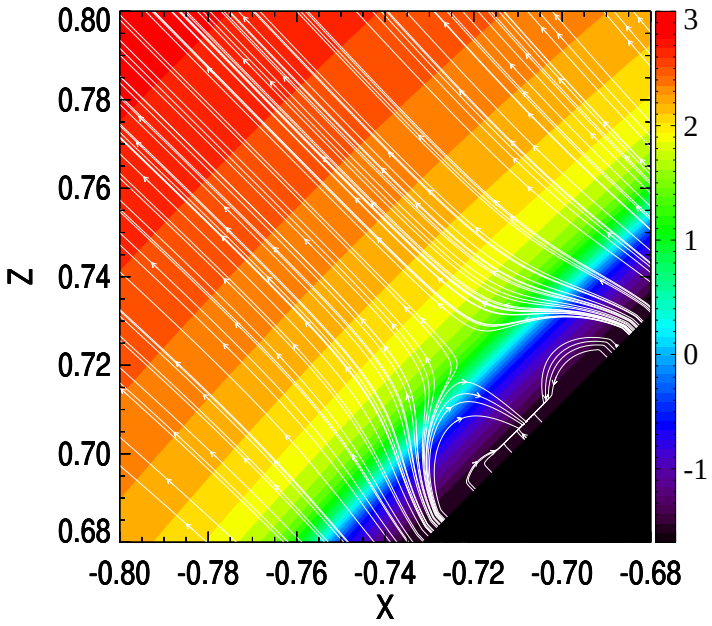

Figure 2.1: Cut-planes across the jet region show the initial collisional heat exchange time scale calculated in [s], plotted on a logarithmic scale. X and Z axes correspond to the HGR coordinate system, see discussion in text. White lines show 2-dimensional magnetic field lines.

scale is small in this region, so that the proton and electron temperatures remain very close to each other. Hence, it is assumed that the imperfections of the adaptation of the physics into the global model do not have a significant effect on the resulting behaviour of the jets.

The initial and boundary conditions applied to these equations are discussed in Section 2.3.3.

2.3.2 Jet Model

In this chapter, we present two jet scenarios, with one jet positioned at 90° and the other at 45° magnetic latitude with respect to the background solar dipole field.

Throughout the chapter, we refer to the jet in the open-field region at 90° as the "polar" jet, and to that in the tilted, closed-field region at 45° as the "loop" jet. The total solar magnetic field is represented by the superposition of a dipole positioned at the Sun's center, to generate the weak, global background field, and a dipole positioned at a small depth $d = 1.4 \times 10^{-2} R_{\odot}$ below the Sun's surface and oriented in the radial direction, to generate the stronger, more compact field of the jet source region. The global dipole field has a vertical strength of 2.8 G at its magnetic pole on the surface, whereas the compact dipole field has a vertical strength of 35 G. The two fields are oppositely directed at the surface above the compact dipole, forming a dome of closed magnetic flux with a magnetic null point at its top. This is the same embedded dipole topology (fan-spine) first proposed by Antiochos (1990) and subsequently modeled by Pariat et al. (2009, 2010, 2015, 2016), Karpen et al. (2017), Wyper et al. (2016); Wyper & DeVore (2016); Wyper et al. (2017, 2018), etc. as described in Section 2.2. As described in Section 2.2, multiple observations show that untwisting motions are quite common in jets, indicating that the jets likely originate in the interaction between twisted flux in compact magnetic loops and untwisted flux in the large-scale background field. To capture this feature, the stored energy released by the jet is built up by imposing a rotation of the chromospheric plasma at the base of the domain around the axis of the compact dipole field. Due to the flux-freezing condition of ideal MHD, the plasma motion drags the magnetic field along, inducing magnetic twist in the closed flux beneath the dome. A similar energization mechanism was used by Pariat et al. (2009, 2010, 2015) to initiate jets in Cartesian geometries. We adopted the simple analytic velocity profile

$$v_{\perp} = Ar - Br^{C}, \tag{2.13}$$

where $v_\perp$ is the tangential velocity of the plasma imposed in the boundary cells of the grid below the solar surface, and r is the radial distance of each point from the compact dipole's axis. To obtain a close match to the profile used by Pariat et al. (2009), We chose the parameter values $A = 3.60 \times 10^3 R_\odot^{-1}$ km s^{-1}, $B = 2.42 \times 10^{11} R_\odot^{-C}$ km s^{-1}, and $C = 5.14$. The rotational motion is imposed between distances $0.002 R_\odot$ and $0.013 R_\odot$ from the dipole axis; at the outer edge of this range, $v_\perp$ falls to zero. These choices result in a peak velocity magnitude of 30 km s^{-1}, which is approximately the chromospheric sound speed and less than 10% of the peak Alfvén speed within the dome. The magnetic field evolution, therefore, is reasonably quasi-static. Slower rotational motions would have been preferred, but they also would have made the simulations impractically long to perform. The rotational speed (approximately 33 km s^{-1}) is just below the local ion acoustic speed and well below the local Alfvén speed.

2.3.3 Boundary and Initial Conditions

Rather than simulating only a local wedge or box around the jet as most jet models do (Pariat et al., 2009, 2010, 2015; Fang et al., 2014), the equations are solved in three dimensions on a spherical domain, from the chromospheric inner boundary at $r = 1.001 R_\odot$ to the outer boundary at $r = 24 R_\odot$. All simulations were performed in a Heliographic Inertial Coordinate System (HGI), which in the case of the non-rotating solar body, is the same as Heliographic Rotating Coordinate System (HGR). The origin is in the center of the solar body, the X axis is aligned with the intersection of the ecliptic and solar equatorial planes, the Z axis is perpendicular to the solar equator and directed North, and the Y axis completes according to the right-hand rule. The zero latitude is positioned on the solar equator, positive in the northern and negative in the southern hemisphere. The zero longitude is towards the X direction, and increases towards the Y axis. In the left bottom corner of each Figure panel,

there is an indicator of the orientation of the coordinate system.

The boundary conditions imposed at $24R_\odot$ are super-Alfvénic outflow. The initial condition over the domain is the Parker solution, with fixed chromospheric boundary conditions $n = 3 \times 10^{10}$ cm^{-3} and $T = 5 \times 10^4$ K at $1.001R_\odot$. At the inner boundary, the boundary conditions are the following:

- The radial magnetic field component B_r is held fixed; the latitudinal and longitudinal components B_θ, B_ϕ are allowed to adjust freely in response to the interior dynamics.
- The density ρ in the boundary cells is fixed according to the exponential scale-height profile.
- Both the proton and electron temperatures are fixed at the lower boundary to $T_{e,p} = 5 \times 10^4$ K.
- The outgoing Alfvén-wave energy density w_+ is fixed to provide constant, continuous heating that sustains the atmosphere (see Sokolov et al. (2013) for details); the incoming wave energy density w_- is set to zero.
- The field-aligned velocity component $v_{\rm par}$ is copied from the first physical cells into the boundary cells (mirrored relative to the boundary); the other velocity components $\mathbf{v_{r\times B}}$ are reflected.

In the chromospheric boundary grid cells the temperature is set to $T = 50000$ K, while the density falls according to the exponential scale height, which provides a solution in hydrostatic equilibrium with gravity. The transition region is intentionally broadened (Lionello et al., 2009) so that it can be numerically resolved in a global scale 3D model, and is lifted, along with the underlying chromospheric plasma, into the corona by the jet. The rotational boundary flows at the jet source location, described in Section 2.3.2, are superimposed on the velocity boundary conditions above.

These flows augment the prescribed Alfvén-wave energy flux, by introducing an additional Poynting flux of energy into the domain, which is the source of the magnetic energy injected as twist field and stored below the dome.

To avoid the singularity of the spherical grid at its poles, the jet region is placed at 45° latitude and 180° longitude. To obtain the open-field conditions for the polar jet setup, the axis of the global background dipole is aligned with that of the compact jet dipole. To obtain a background with a tilted and closed magnetic field around the loop jet, we aligned the global dipole axis with the Z coordinate direction, as is usually done.

In the following simulations, we used a second-order scheme with Linde flux and Koren limiter, setting $\beta = 1.2$ (for details, see Tóth et al., 2012). To keep the divergence of the magnetic field small, the eight-wave scheme of Powell (1994) is used. The radially stretched spherical block-adaptive grid uses 9 refinement levels, resulting in 6 million cells. The simulated three hours of physical time required approximately 8 million iterations and took more than a half million CPU hours per simulation.

The initial solar wind solutions (before the jets are initiated) are presented in Figures 2.2 and 2.3.

Figure 2.2 shows the radial velocity and magnetic field profiles in both configurations. The top left panel shows the effect of the 45° rotation of the global dipole field on the solar-wind velocity profile for the polar jet; the bottom left panel is the same view for the loop jet. In the middle panels, the small negative-polarity region (blue) on the upper hemisphere is due to the compact dipole field where we generate the jets. In the right panels the initial magnetic structures near the jet dipole are shown. The ambient magnetic field is weaker and tilted in the case of the loop jet

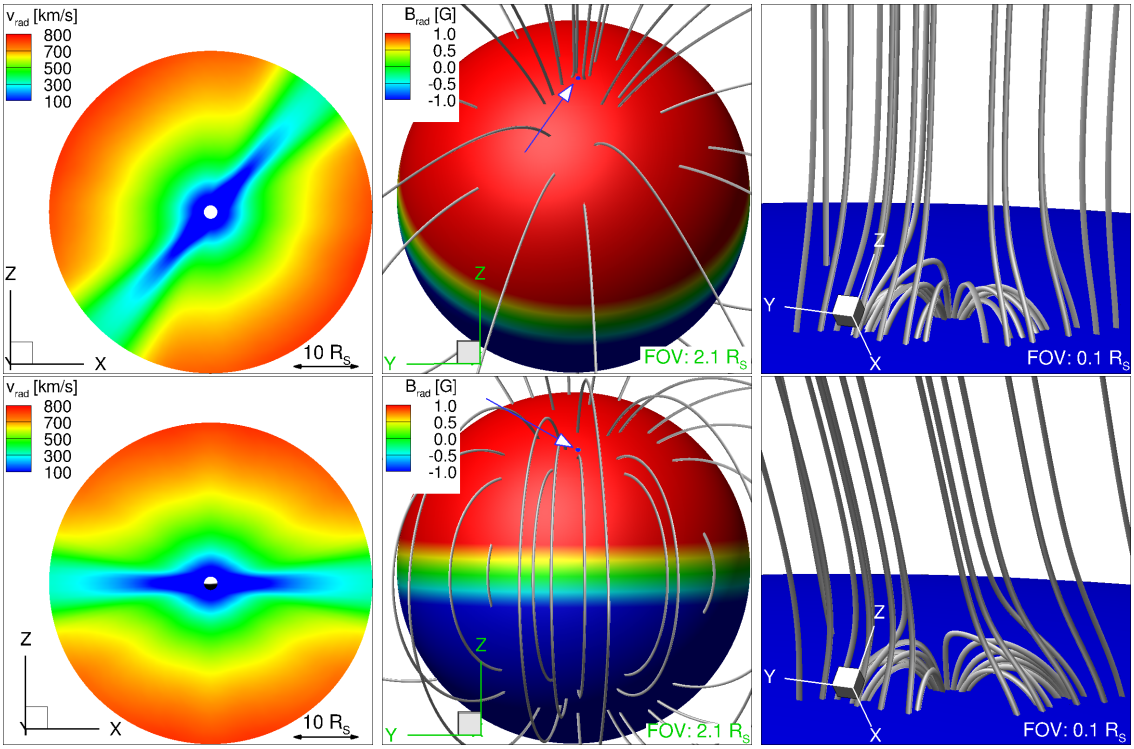

Figure 2.2: Initial configurations for the simulated polar jet in the vertical open-field region (top row) and the loop jet in the tilted closed-field region (bottom row). Shown are the radial velocity in the $Y = 0$ plane (left panels), the radial magnetic field on the solar surface $r = R_\odot$ with some representative field lines (middle panels), and a zoomed-in view of the jet location (right panels). The compact jet dipole is the small blue dot marked by the arrows on the upper hemisphere. The scales are indicated by the black arrows of the field-of-view (FOV), which define the physical size of the plotted regions. In the left bottom corners the indicator for the orientation of the coordinate axes of the images is shown.

(bottom) compared to the polar jet (top). Figure 2.3 shows the profiles of magnetic field strength, radial magnetic field component, density, pressures, and temperature ratio. The compact jet dipole has no significant effect on the steady-state solar wind solutions at global scales.

We first run the simulations in local time-stepping mode for 80000 iterations, during which we perform adaptive mesh refinement (AMR) on the inner shell of the domain close to the inner boundary, to resolve the high-density transition region

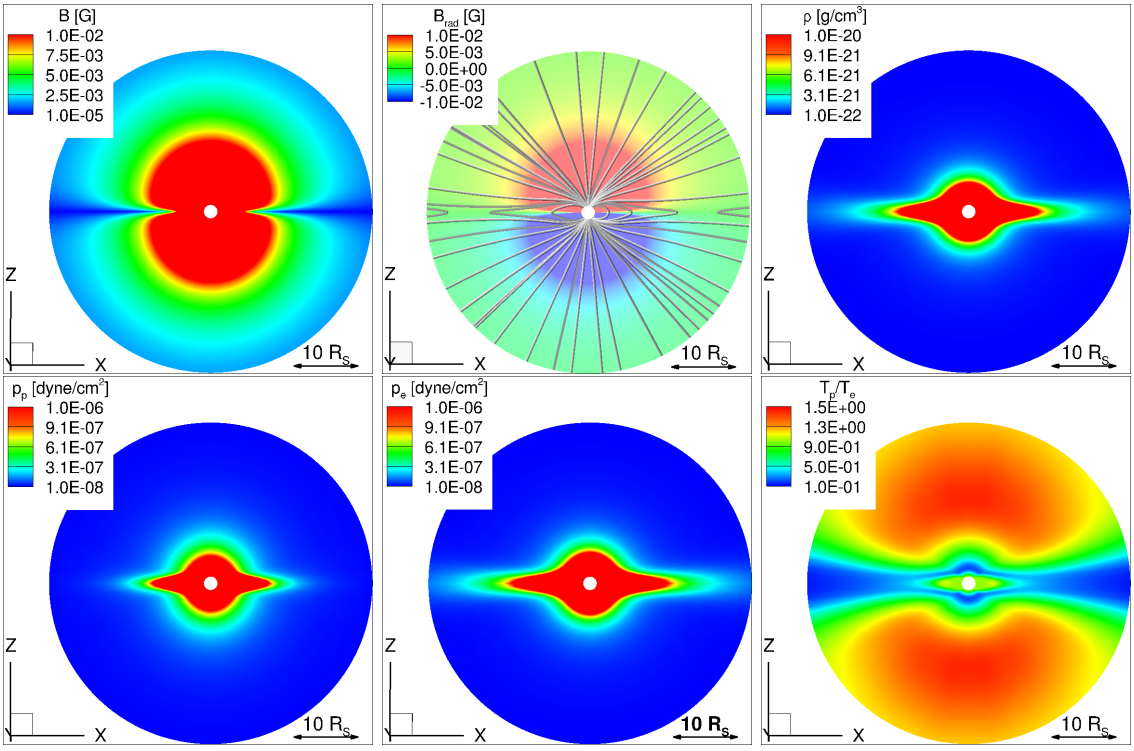

Figure 2.3: The loop jet initial condition on the $Y = 0$ plane. From left to right, top row: total magnetic field strength, radial magnetic field component with some magnetic field lines, and density of the steady-state solar wind. Bottom row: proton pressure, electron pressure, and temperature ratio of protons to electrons. See Section 2.3 for details on the model.

and low corona. Once those solutions converges, we again perform AMR, but this time only close to the region where the jet dipoles are located: in a spherical box of 5° in both longitudinal and latitudinal directions and $0.1R_\odot$ in the radial direction. The resulting cell size in the jet region is about $1.4 \times 10^{-3}R_\odot$ in the azimuthal and $2.5 \times 10^{-5}R_\odot$ in the radial directions. Such high resolution is needed to fully resolve the jet structure. The static grid for the polar jet simulation is shown in Figure 2.4.

On the left, there is the whole simulation domain; the middle and right panels focus on the jet region. The grid for the loop jet is similar. As jets have been observed to persist over long time scales (some jets inside active regions last for up to 10 hours; Savcheva et al., 2007), we carried out both simulations until the solutions become quasi-periodic in response to the ongoing rotational driving.

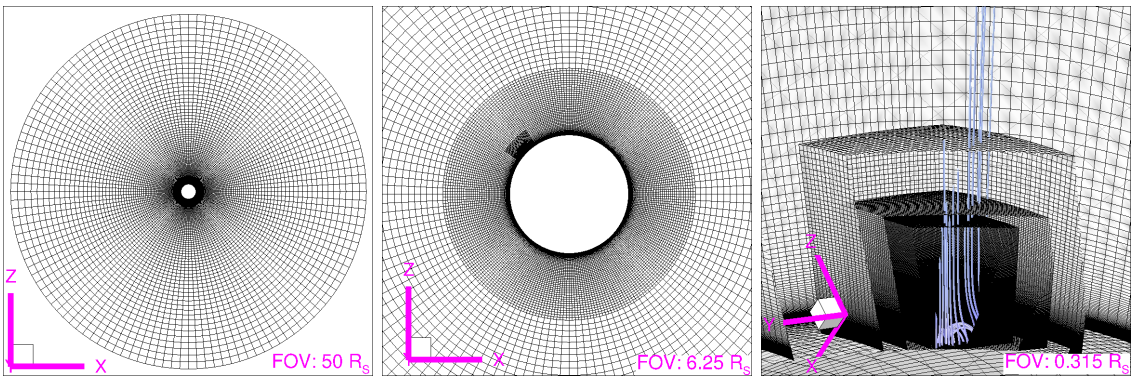

Figure 2.4: Left: grid structure in a 2D cut at $Y = 0$ of the whole domain ($24R_\odot$). Middle: same, zoomed to $6.25R_\odot$, showing the first few levels of the adaptive, radially stretched grid. Right: zoomed to $0.3R_\odot$, showing several magnetic field lines near the jet dome.

2.4 Simulation Results

In this section we discuss the results of the simulations of both the polar and loop jets. Due to the similarities in the low-coronal structure and the driving mechanism in the two cases, numerous features of the resulting jets are shared by the configurations. On the other hand, because the polar jet occurs in open magnetic field while the loop jet occurs in closed field, other aspects of the two jets are distinctly different. We explore both their similarities and their differences in the subsections to follow.

As described above, in the beginning both systems are relaxed to a minimum-energy, quasi-steady state. Then, the steady footpoint driving is initiated within the closed magnetic flux of the compact dipoles. In each case, there followed an initial interval of buildup of magnetic twist within the closed regions, culminating in a first, energetic burst of reconnection and release of a jet. The systems then relaxed, but not all of the way back to their starting, minimum-energy states. Closed magnetic flux embedded deep within the jet source region is unable to transfer its twist to the ambient, untwisted open field by reconnection. This trapped twist flux and its associated magnetic free energy served as the starting configuration for a new cycle

of constant footpoint motions, gradual energy storage, sudden onset of magnetic reconnection, and rapid release of another jet. These repetitive cycles quickly settled down to drive quasi-periodic recurrent jets in both of the configurations. We anticipated this outcome, based on the previous demonstration by Pariat et al. (2010) of homologous polar jets driven by similar footpoint motions in an adiabatic, Cartesian, gravity-free simulation. In the descriptions below, we focus on the properties of a typical quasi-periodic individual jet from each of the two cases, rather than on the unique, and somewhat atypical, initial jet. The most important new features of the simulations are the properties of the jet plasma, which we illustrate in the inner corona for both of the jets. Thereafter, we examine the cumulative impact of the recurrent polar jets on the outer corona as well.

2.4.1 Jet Generation by Magnetic Reconnection

The ongoing process of jet generation by magnetic reconnection is illustrated in Figure 2.5 for the polar jet in the top row and for the loop jet in the bottom row.

All panels show a fixed-time snapshot during one of the quasi-periodic bursts of reconnection between the twisted, closed flux of the compact dipole field and the untwisted, open (or, in the loop case, faraway closed) flux of the global dipole field. Within each row, the field lines labeled [1] and [2] are the same. The lines labeled [2] are strongly twisted field lines rooted to the chromosphere at both ends within the closed-flux region. They are pre-reconnection field lines adjacent to the separatrix surface of the compact dipole field. The lines labeled [1] are rather strongly bent and are rooted to the chromosphere only at one end and, therefore, belong to the open-flux region. They are post-reconnection field lines, also adjacent to the separatrix surface.

The field lines [1] pass through a vertical plane cutting across the jet (left panels),

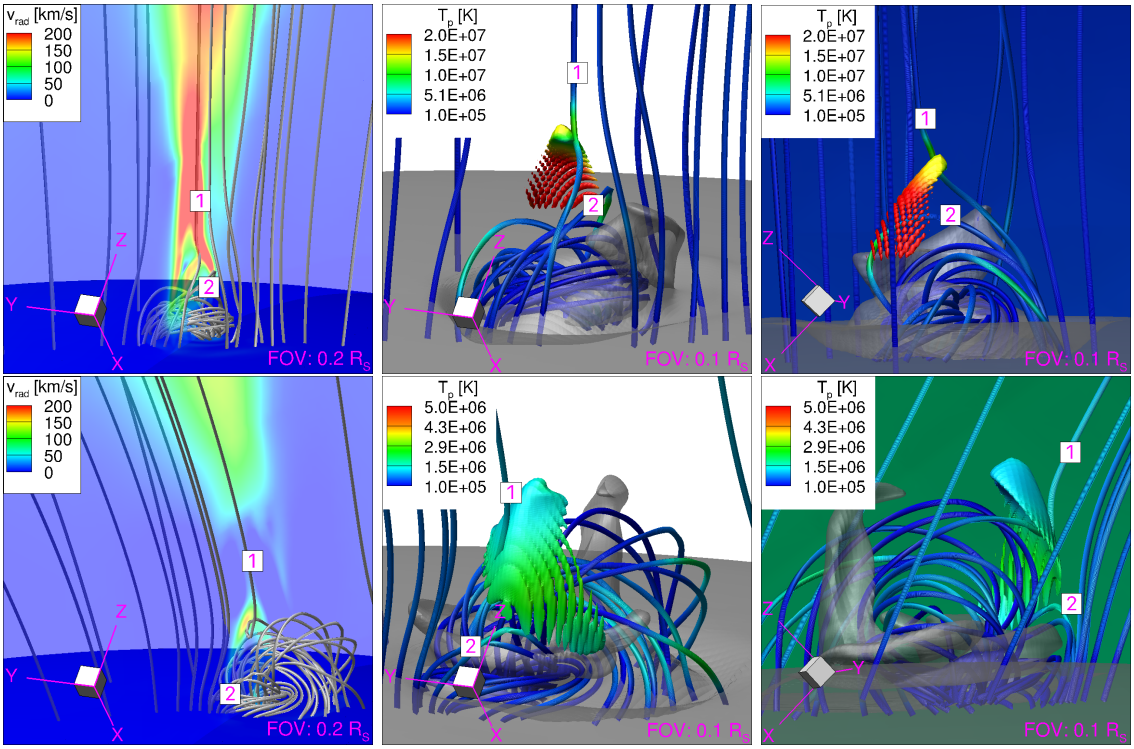

Figure 2.5: Polar jet simulation at time $t = 1$ h 27 m 20 s (top row); loop jet simulation at time $t = 2$ h 27 m 30 s (bottom row). Left panels: radial velocity is color-shaded on a plane through the center of the jet; gray and blue lines represent magnetic field lines in front of and behind the plane, respectively. Middle and right panels: zoomed to the jet core at the same times, from different perspectives. Magnetic field lines and the null-point region on the separatrix surface ($B = 0$ isosurface) are color-shaded according to proton temperature. Shown in transparent gray is an isosurface of dense plasma ($\rho = 5 \times 10^{-15}$ g cm^{-3}). Selected pre- and post-reconnection magnetic field lines are labeled [2] and [1], respectively.

where color shading shows the strong reconnection outflows from the reconnection region. These flows start from the top of the closed-flux dome in both jets. The outflow is stronger in the case of the polar jet throughout the simulation than at lower latitudes, because the ambient magnetic field is stronger in the open-field region. The middle and right panels of Figure 2.5 show the rotating separatrix surface, which is color-shaded by the proton temperature. This surface is much hotter than the ambient plasma, due to magnetic-energy release by the ongoing reconnection. The bent field lines [1] at the domes of the jets have newly reconnected and are still touching the

locally heated separatrix surface. After a few seconds, they stretch and straighten out to become parallel to the ambient open field. The twisted field lines [2] also touch the separatrix surface, and are about to reconnect with the ambient field to form new lines of type [1]. The visible twist and tilt on the open field lines, the heated spots on the separatrix surface, and the strong bidirectional outflows all highlight the locations of reconnection between the closed, twisted flux of the compact dipole source and the open, untwisted flux of the ambient field.

2.4.2 Temperature

The middle and right panels of Figure 2.5 show elevated temperatures occurring on the separatrix surface, reaching 20 MK for the polar jet (top row). As observed with Yohkoh/SXT by Shimojo et al. (1996), the bright spot is expected to be above the footpoint of the jet region (see figures at Section 2.5): the localized heating takes place around the dome, especially close to its top, where the magnetic reconnection takes place. We show the proton temperature in Figure 2.5. Because the numerical scheme used in the model, the energy dissipated by numerical reconnection is deposited directly into the proton fluid (Equation 2.4). Thermal energy subsequently is transferred to electrons via collisions, so the electron temperature responds with a time delay relative to the reconnection events that promptly heat the protons. This electron heating, in turn, has a profound effect on the radiative properties of the jets by determining which emission lines are excited and how intense are their emissions. Synthetic images of the simulated polar jet are compared with observations below in Section 2.5. (Synthetic images of the loop jet are similar to the ones presented for the polar jet.)

2.4.3 Density

The middle and right panels of Figure 2.5 also show gray isosurfaces of plasma at chromospheric density $\rho = 5 \times 10^{-15}$ g cm^{-3}. This dense plasma has been lifted up to heights well above the ambient chromosphere, where it mixes with the tenuous coronal plasma. We also have identified complementary regions of highly depleted plasma density at very low heights, close to the footpoints (not shown). This density structure is similar to those observed, for example, with Yohkoh/SXT by Shibata et al. (1992). Due to the quadratic dependence of the optically thin radiative losses on the plasma density, the enhanced densities at low coronal heights contribute very substantially to the synthetic emission images shown in Section 2.5.

As the twisted magnetic field in the closed region reconnects with the ambient field in the open region, the reconnection outflows depart along both field-aligned directions, upward and downward. The upward reconnection outflow continues to propagate along the field lines: radially in the polar jet and equatorward in the loop jet. Figure 2.6 shows the changes in the density profiles, relative to the steady-state corona, for both jets.

A strong density enhancement extends to several solar radii in the polar jet, while the jet material crosses the equator to reach the other hemisphere in the loop jet. The polar jet contributed density enhancements over ten times greater than the ambient coronal value after expansion into the outer corona. These values are far larger than those observed in the adiabatic or isothermal simulations of Pariat et al. (2009, 2010, 2015) or Karpen et al. (2017), respectively, none of which included the effects of the underlying chromosphere on the jet density. Pucci et al. (2013) observed density enhancements of standard and blowout jets to be about $10^{-16} - 10^{-15}$ g cm^{-3}, which in magnitude corresponds to the density of the lifted chromospheric plasma in the simulations.

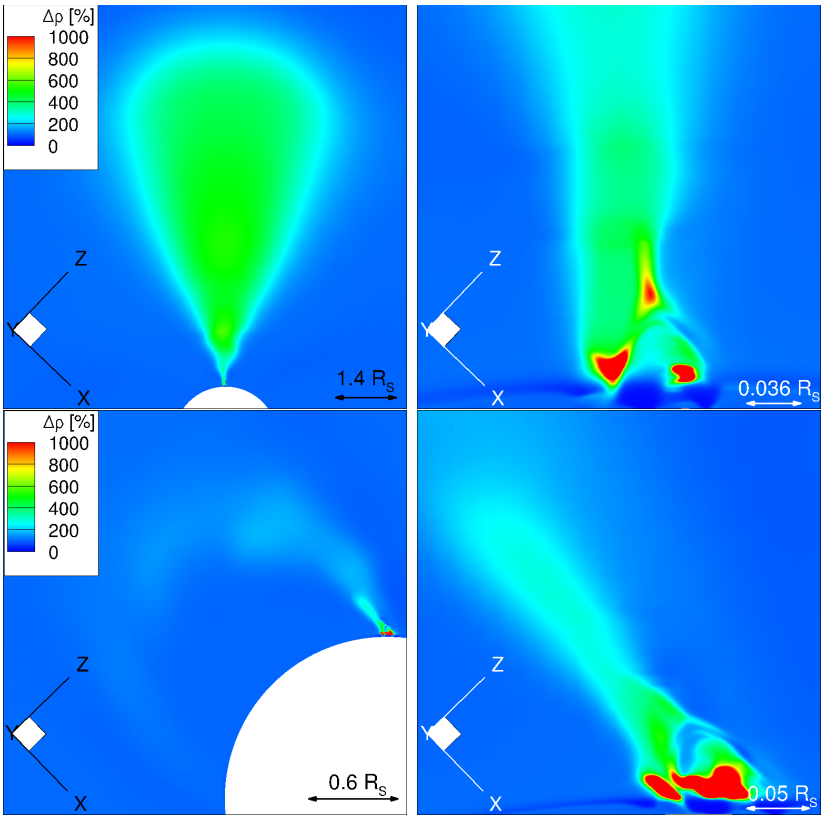

Figure 2.6: Density enhancement relative to the initial steady state in planes through the center of the polar (top row) and loop (bottom row) jets. Left panels: large-scale view of the solar wind; the partial white disk is the Sun. Right panels: close-up view near the solar surface.

2.4.4 Velocity

As described in Section 2.3, the rotation around the bipole axis is imposed on an annulus at the lower boundary. This implies that the magnetic field lines crossing the surface in the center of the annulus (close to the axis of the compact dipole) have one footpoint fixed, while the other rotates along with the plasma. These magnetic field lines become tilted and twisted until they reconnect with the ambient field. As both the rotation and the reconnection are ongoing processes throughout the simulation, they introduce a quasi-periodic behavior into the system. In particular, they introduce periodic velocity and magnetic disturbances that travel outward along the magnetic field lines. This periodicity appears in the velocity profiles as Alfvénic perturbations.

These are visible in Figure 2.7 as torsional waves propagating along the field lines.

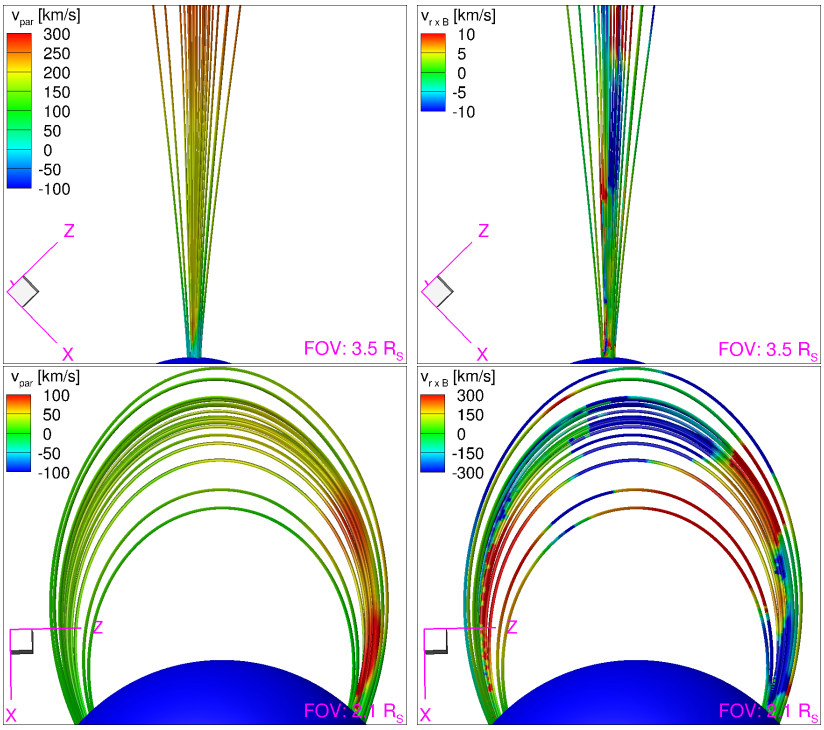

Figure 2.7: Plasma velocities for polar (top row) and loop (bottom row) jets color-shaded on selected magnetic field lines at the end of the simulations. Left panels: field-aligned component ($v_{\rm par}$). Right panels: perpendicular component ($v_{\mathbf{r}\times\mathbf{B}}$). The perpendicular component is projected along the cross product of the position vector $\mathbf{r}$ with the magnetic field $\mathbf{B}$, to distinguish positive and negative directions.

2.4.5 Flows, Fields, and Forces in the Outer Corona

We now turn to the larger-scale effects on the outer corona of the simulated jets. Because the loop jet leaves signatures only relatively near the solar surface in the inner corona, in the remainder of this Section 2.4 we discuss in detail only the polar jet simulation. In case of the loop jet the closed field geometry traps the jet outflow.

The physical size of this jet (length and width) is similar to what Savcheva et al. (2007) reported, although in their study there were some even larger jets observed in both dimensions. Due to the radial geometry of field lines, the polar jet leaves a

stronger signature in the ambient plasma than the loop jet. In the polar jet case, the disturbances reach the outer corona beyond $20R_{\odot}$ by the end of three hours of simulation time. This translates to an average wave speed of about 1300 km s^{-1}; the jet plasma outflow is much slower (see later). Figure 2.8 shows the change introduced by the polar jet in the velocity, magnetic field, and Lorentz force profiles by the end of the simulation, on a global scale.

As in the case of the jet driven by the helically twisted magnetic field described by Shibata et al. (1992), and confirmed via MHD simulation by Fang et al. (2014), the acceleration force is the Lorentz force as the magnetic twist propagates along the field lines. Wang et al. (1998) looked for jet signatures in the corona using simultaneous observations by SoHO/LASCO and EUV Imaging Telescope also on board SoHO (SoHO/EIT Delaboudinière et al., 1995). They correlated 27 jet events observed by both instruments by following the jet lifetime from the appearance of bright points in SoHO/EIT up to above three solar radii. The bulk material followed the leading edge of the jet at a smaller speed, decelerating below two solar radii. As a result, the jet plasma signature became elongated in coronal plasma, just as it is shown in Figure 2.8. In the top, the radial solar wind speed decreased, and also there are flows diverging from the jet towards the equatorial region. The middle row shows that the radial magnetic field increases in a large area in the outer corona, and it is depleted close to the jet. Due to the radial dependence of the magnetic field strength, calculating the energy change in the region is highly dominated by the lower, depletion region. This is why the magnetic energy overall decreases in the coronal region, as discussed in Section 2.4.6. In the latitudinal and longitudinal fields, the periodic perturbation propagates outwards. In the bottom row, we show that Lorentz forces accelerate plasma radially (mostly) outwards, and also towards the equatorial regions, in a periodically twisting manner.

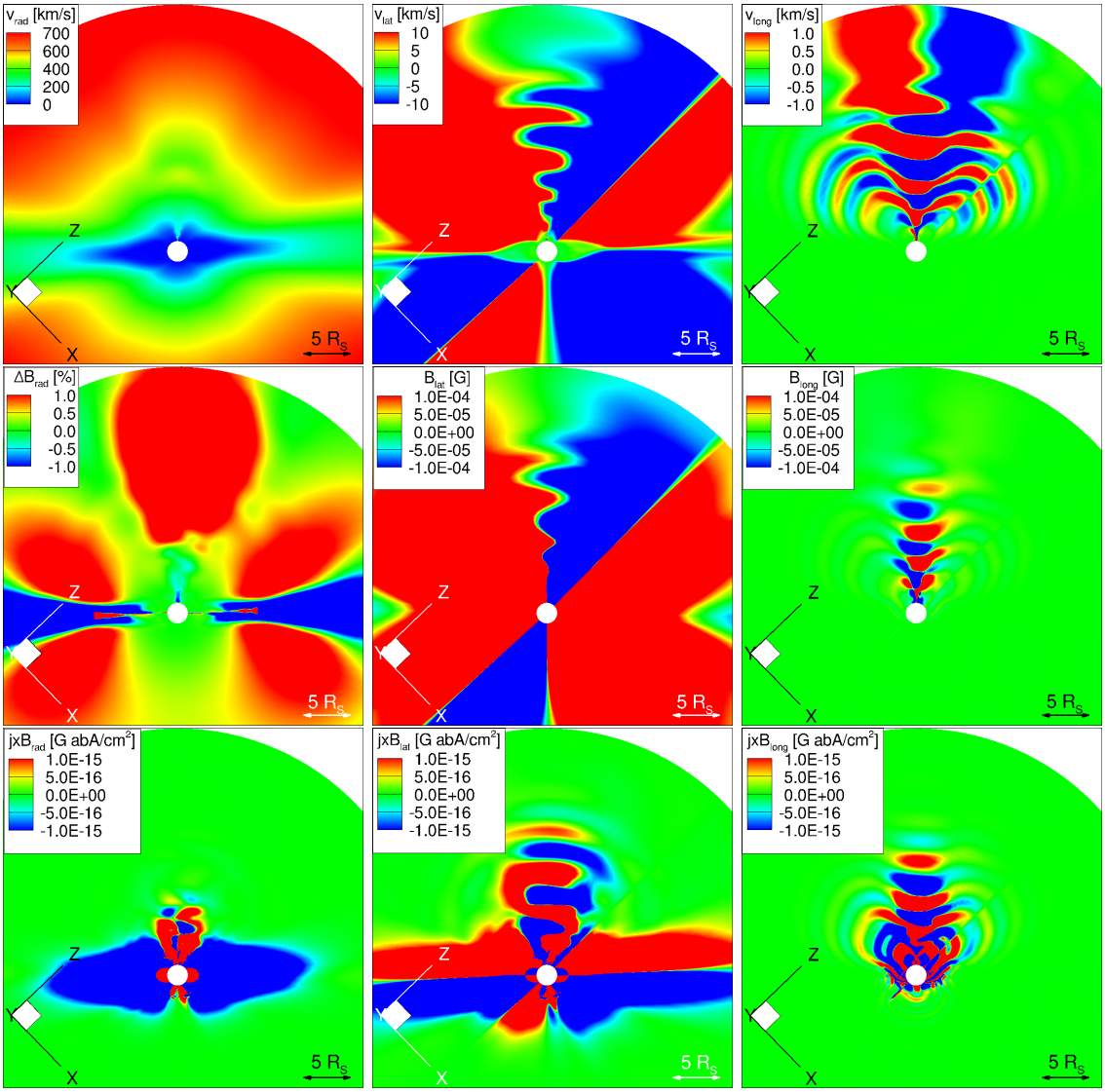

Figure 2.8: Polar jet at the end of the simulation. Top row: radial, latitudinal, and longitudinal velocity components (left to right). Middle row: radial magnetic field change (left) and latitudinal and longitudinal magnetic field components (middle and right). Bottom row: radial, latitudinal, and longitudinal components of the Lorentz force (left to right). All figures show the same plane through the center of the jet. The white disk is the Sun.

2.4.6 Mass, Momentum, and Energy Transport

In order to provide an overall estimate of the polar jet contribution to the solar wind, we calculate the mass, momentum, and energy transport from the chromosphere into the corona across the jet area throughout the simulation. Paraschiv et al.

(2015) used a sample of 18 jet observations to conclude that radiative and conductive losses are negligible. Also, calculating the wave energy and radiative loss terms, we observe no significant change to the background solar wind due to the jet. For this reason, we calculate the integrals of mass density, momentum density, and the magnetic, gravitational, internal, and kinetic energy densities, omitting wave energy and radiative losses. The integrations are performed every ten seconds throughout the simulation within two fixed, overlapping volumes shown in Figure 2.9.

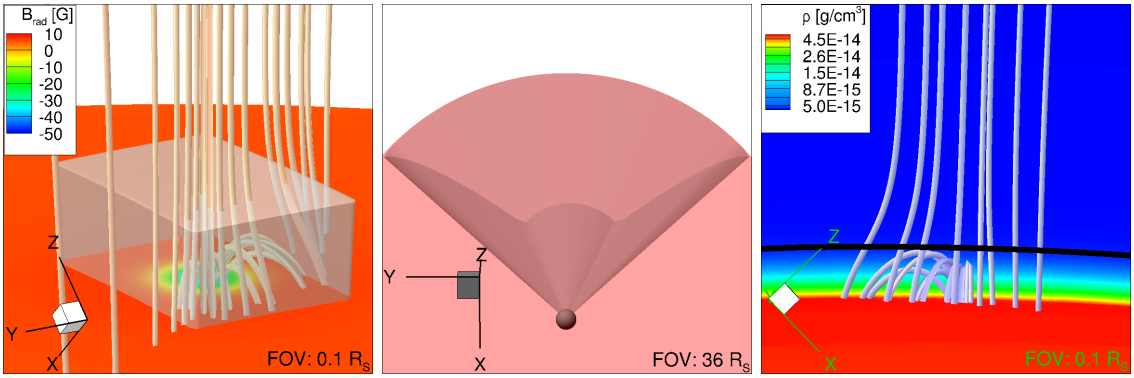

Figure 2.9: Integration regions for the polar jet. Left panel: the core integration region is the translucent box. The radial magnetic field component on the solar surface is color-shaded; selected magnetic field lines are shown. Middle panel: the coronal integration region is the pink-shaded volume. Right panel: plasma density is color-shaded near and on the solar surface. The black line marks the lower boundary of the coronal integration region at $1.015 R_\odot$; the chromosphere is excluded from this region.

The first region (left panel) is selected to contain the core of the jet. Its extents are $[43°, 47°]$ in latitude, $[178°, 182°]$ in longitude, and $[1.001, 1.030] R_\odot$ in radius. We refer to this region as the 'core,' and use this volume to calculate and identify local effects of the rotation that take place in the jet-generation region.

The extents of the second region are selected so that the velocity perturbations propagating due to the jet into the outer coronal plasma are fully contained within the volume (middle panel). This region covers $[15°, 75°]$ in latitude and $[130°, 230°]$ in longitude. Since we want to obtain a direct estimate of the jet's contribution to

the solar wind, the mass, momentum, and energy transfers are calculated considering only the coronal plasma above $1.015R_{\odot}$ (the black line on the right panel of Figure 2.9) out to the far end of the domain at $24.0R_{\odot}$. We refer to this region as the 'corona.'

We show the enhancements of mass, momentum, and energy relative to the steady-state in Figure 2.10 for both volumes.

In the core of the polar jet, a substantial amount of dense plasma is lifted up from the chromosphere into the core region. This plasma passes through the core volume and then gets released into the coronal region. Comparing the changes in the total and gravitational energy within the core, we find a strong correlation between them. The same dynamics can be observed on the top and middle panels showing the mass and momentum changes. The panels showing the mass change in the corona indicate that the region is not yet filled with the dense plasma, but those in the middle row show that the rate of momentum growth decreases by the end of the simulation time. This suggests that either the plasma starts to reach the outer boundary, leaving the simulation (and integration) domain, or the plasma might get released in a decelerating manner due to the increasing local density. In the polar jet, after the first energetic reconnection event, the magnetic energy reduces in the coronal region due to the field relaxation close to the jet core (Figures 2.8 and 2.11).

Internal and kinetic energies converge to roughly constant values, with the kinetic energy reaching those values more slowly and remaining slightly below the internal. Also during the first reconnection event, strong downward flows decelerate the otherwise radially outward moving plasma, which causes a large decrease in the kinetic energy at around t = 1000 s. This event resembles the pulse-driven jets discussed by Srivastava & Murawski (2011). The driver is most likely a single velocity pulse generated by the magnetic reconnection in the lower atmospheric region, although we do not observe cool plasma falling back after the ejection, as seen in observations.

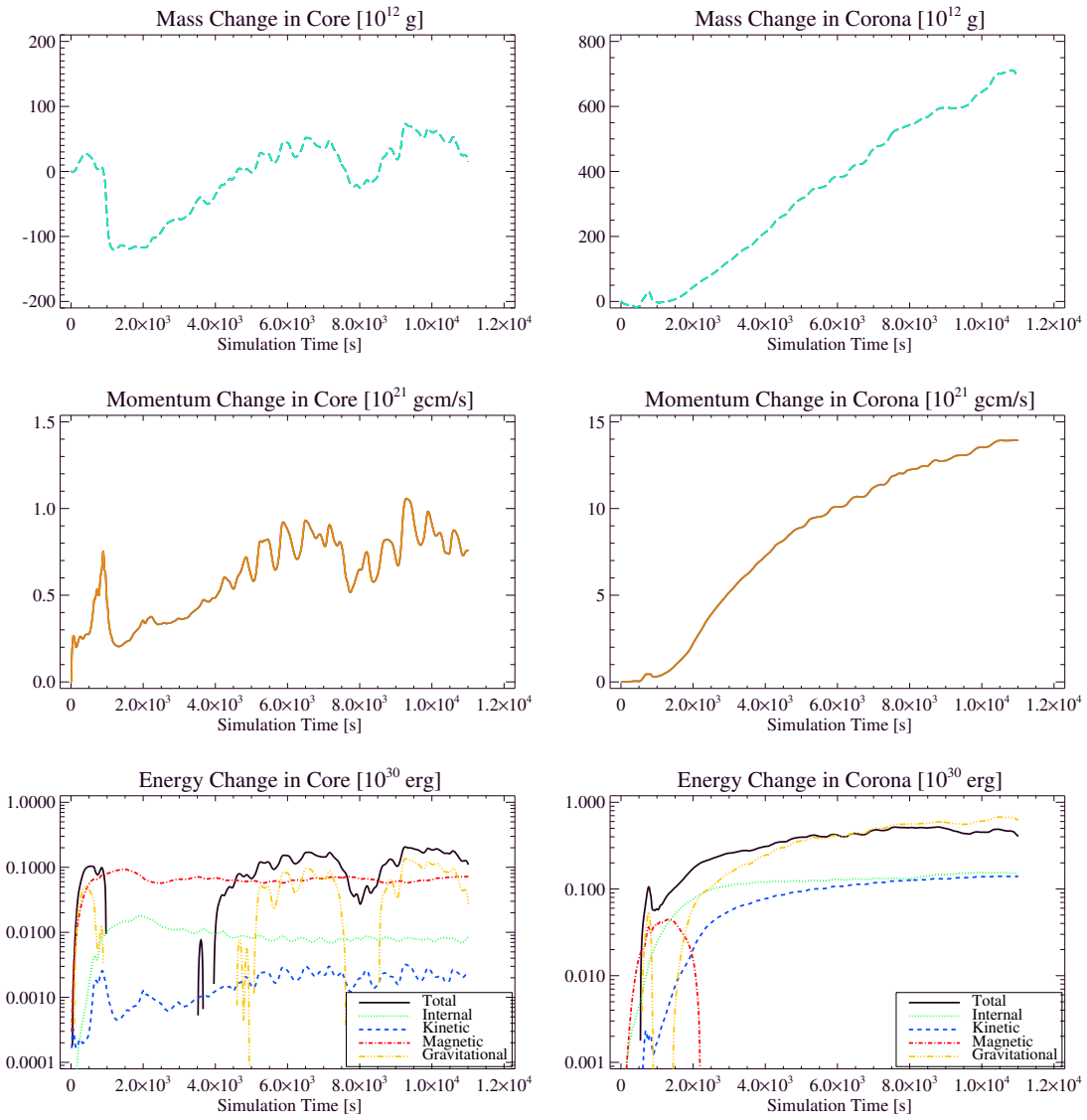

Figure 2.10: Integration results for the polar-jet core (left panels) and corona (right panels): changes in mass (top row), radial momentum (middle), and energies (bottom). Negative values of changes in the energies are not shown due to the logarithmic scale. See Section 2.4.6 for details.

Looking at the mass and momentum changes in the core over time, the phases of the jet dynamics described by Pariat et al. (2010) clearly appear: the energy build-up in the first approximately 1000 s, then the violent energy release, followed by a relaxation to a quasi-periodic state. A typical X-ray jet of size $5\times10^3-4\times10^5$ km has

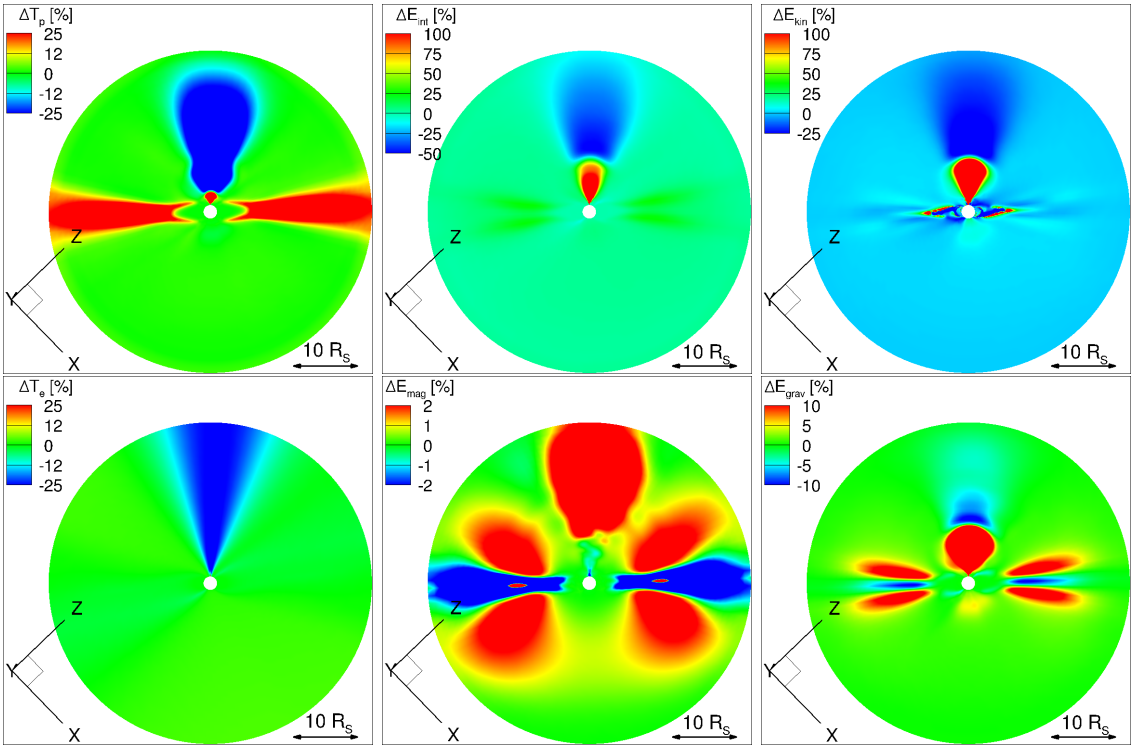

Figure 2.11: Temperature and energy-density changes for the polar jet at the end of the simulation. Top row, left to right: proton temperature, internal energy density, and kinetic energy density. Bottom row: electron temperature, magnetic energy density, and gravitational energy density. All figures show the same plane through the center of the jet as in Figure 2.8. The white disk is the Sun.

kinetic energy about $10^{25}-10^{28}$ erg (Shibata et al., 1992). This jet model fits into both ranges. We estimate the internal energy and mass transport into the corona through the polar jet model to be 6×10^{13} g in the core, and 7×10^{14} g in the corona. Shibata et al. (1992) also estimated these values in the case of a jet driven by a helically twisted magnetic field. The internal energy was about an order of magnitude larger than the kinetic. The mass of the observed jet was estimated to be around 10^{13} g. We see that the change of gravitational energy dominates both volumes, followed by magnetic energy in the core of the jet, and internal and kinetic energies within the coronal volume. These results are consistent with the observational study done on 18 jets by Paraschiv et al. (2015), finding that plasma heating takes a larger share of the energy than plasma acceleration.

2.4.7 Quasi-Periodic Recurrence

There are two oscillatory behaviors: faster fluctuations superposed on oscillations with longer periods. The large amplitude oscillations observed in the core appear mostly in the mass change rate, but they leave much weaker signatures in the energy terms compared to the small amplitude ones. Beside the three large-scale peaks in density, momentum and gravitational energy at times around $t = 1000$ s, $5000 - 7500$ s and $8000 - 10000$ s, there are higher frequency oscillations, visible in all variables shown in Figure 2.10. There is a strong correlation between mass change, momentum change, gravitational, kinetic and internal energy changes, and a strong anti-correlation between these and magnetic energy changes. These oscillations are clearly due to the continuous quasi-periodic reconnection process that creates the plasma perturbations shown in Figure 2.8. The oscillatory behavior is driven by reconnection events where the magnetic field direction changes sufficiently rapidly. The periodicity of these events is governed in part by the local value of the numerical resistivity (as discussed in Section 2.3.1), and in part by the rate of formation and strengthening of the current structures in response to the imposed surface motions, which together determine the onset and conditions and rate of reconnection. The approximate period of these oscillations is about 700 - 800 s.

Chifor et al. (2008b) also observed recurring solar jets in X-ray and EUV bands with periodicity of about an hour. Flux cancellation (with a minimum magnetic energy loss per jet of about 3×10^{29} erg) was correlated with the brightenings observed in X-ray and Ca II H. The same magnitude of total energy transported into the corona is produced by the model. Chifor also observed type III radio burst signatures during the first two largest jets, suggesting that stronger reconnection events happened at the beginning of the jet process, compared to later occurrences.

As discussed in Section 2.3.2, there is an imposed differential rotation profile in the boundary cells with peak rotation speed 30 km s^{-1} at distance $0.0085R_{\odot} = 5950$ km from the bipole axis. The plasma completes one rotation every 1246 s, corresponding to 8.86 rotations during the 11040 s simulation time. The system stabilizes after the first energetic reconnection at around $t = 3000$ s. Until $t = 10500$ s, there are about 10 complete high frequency oscillations (inferred from Figure 2.10), yielding an average period of 750 s. The period of reconnection events is about half of the rotation time period. Shen et al. (2011) discussed rotary motion and radial expansion on one side of a polar jet seen by SDO/AIA. They observed a mean rotational period of about 564 s. The twist stored before reconnection was between 1.17 and 2.55 turns, which matches theoretical and simulated results. The modeled jet shows more frequent reconnections and hence, it stores less twist. We suspect that the reason for this difference is that we use a second-order numerical solver, which corresponds to relatively high numerical resistivity. Using a numerical solver of higher order would decrease the numerical resistivity and may lead to more twist being stored between the reconnection events.

2.4.8 Energy Changes in the Corona

Shen et al. (2011) estimated the stored magnetic energy to be approximately $0.7 - 3.4 \times 10^{30}$ erg, and the jet's total hydrodynamic energy (kinetic, internal and gravitational) to around 1.7×10^{29} erg. The simulated energies are comparable to their estimate, suggesting that the modeled energy transport into the solar corona is consistent with observations.

In our simulations the surface area of energy deposition is a $2^{\circ} \times 2^{\circ}$ square (latitudinal $\times$ longitudinal width). We integrated the Poynting fluxes in the first physical cells due to both Alfvén wave dissipation or due to plasma motion in the changing magnetic field. The integration box is selected to be the smallest possible containing

the base of the jet structure. In this small region, we find that the average energy deposited in the boundary due to Alfvén wave dissipation is about 271 erg $\mathrm{cm}^{-2}\mathrm{s}^{-1}$ and 2490 erg $\mathrm{cm}^{-2}\mathrm{s}^{-1}$ due to plasma motion. All plasma motions are included in the energy flux calculation, including interior flows or waves that impinge upon the boundary and alter the imposed flow. These values are hence considered only a time average of Poynting fluxes related to the jet in the regions.

The imposed rotation generates Alfvén waves. As the energy panels in Figure 2.10 show, the energy deposited in the corona is mostly due to the plasma outflow and heating, rather than magnetic energy. Looking at the panel of the core energy changes, substantial magnetic free energy is stored in the jet and the reconnection process significantly changes only the gravitational, internal and kinetic energies, not the magnetic energy itself. We conclude that the magnetic energy released in a reconnection event is only a small fraction of the magnetic energy stored within the jet-producing region.

As will be shown below, the gravitational energy is dominant in the core, due to the large relative density enhancement shown in Figure 2.6. Looking at a cut-plane across the jet in Figure 2.11, the temperature and energy change significantly in the domain relative to the initial state of the solar wind. There is a visible jump in each energy profile at about $9R_{\odot}$, where the density enhancement region (relative to the original value) ends (see Figure 2.6, top right). At this height, the relative change in the plasma beta jumps from positive (in the low corona) to negative (in the outer corona). This jump is a consequence of the Alfvén wave heating, which is based on Equation 2.6. The reflection rate $\mathcal{R}$ introduced in Equation 2.6 is a key parameter understanding how the energy is deposited in the disturbed coronal region. Following the derivation of van der Holst et al. (2014), the evolution of parallel and antiparallel Alfvénic waves is governed by a balance between reflection $\mp\mathcal{R}\sqrt{w_{-}w_{+}}$

and dissipation $-\Gamma_{\pm} w_{\pm}$:

$$\mathcal{R} = \mathcal{R}_{\rm imb} \left(1 - 2\sqrt{\frac{w_-}{w_+}} \right), \tag{2.14}$$

where

$$\mathcal{R}_{\rm imb} = \sqrt{\left(\mathbf{b} \cdot [\nabla \times \mathbf{u}]\right)^2 + \left([\mathbf{V}_A \cdot \nabla] \log V_A\right)^2} \tag{2.15}$$

and

$$\Gamma_{\pm} = \frac{2}{L_{\perp}} \sqrt{\frac{w_{\pm}}{\rho}}, \tag{2.16}$$

and $L_{\perp}\sqrt{B} = 1.5 \times 10^9$ cm $\mathrm{G}^{1/2}$ is an input parameter. The reflection and dissipation rates strongly depend on the local mass density, the magnetic field strength and direction, and the gradients of those variables. We consider only the form of reflection rate in the case of imbalanced turbulence, on the northern hemisphere of the Sun, along straight magnetic field lines, where $4w_- \leq w_+$, as this region basically overlaps the hemisphere the polar jet interacts with. The dominant energy density of outward propagating (parallel) waves is more than 100 times greater than the counter-propagating (anti-parallel) wave energy density in this region, so strongly imbalanced turbulence is assumed and local wave dissipation. During the simulation, the reflection rate increases due to the introduced Alfvén speed gradients and velocity vorticity along the radial flow direction (Figure 2.8). With the increased reflection rate, the turbulence becomes more balanced, and there are more inward propagating waves. The interaction between the oppositely propagating waves results in higher energy dissipation rates. This means that, where the reflection rate has a sharp gradient (where the density-enhanced region ends), there is a discontinuity in the rate of energy deposition. The result of this sharp gradient is shown in Figure 2.11: the

lower region absorbs all the energy and inhibits heating above it. Within the region of large reflection rate, the corona is over-heated relative to the initial condition. Due to the way the traveling Alfvén waves are trapped within the region, the energy deposition decreases with radial distance from the region. This can indicate why there is a strong gradient in temperature and energy change in the corona. The another strong gradient in the proton temperature corresponds to another sharp gradient in the reflection rate. The outer boundaries of these regions are propagating radially outward during the simulation, with a speed of approximately 325 km s^{-1}. Overall, the integrals of energy changes are highly biased by the low-coronal region because the changes are much more significant there where the strong fields reconnect. This is why the overall budget for each energy variable becomes positive in the end. As Parker Solar Probe is going to fly through regions as low as 10 solar radii above the surface, the large gradients in density and temperature could be captured through measuring proton and alpha-particle properties.

The signatures of jet contribution to coronal heating and solar wind plasma were studied by looking for asymmetries (blue shifts) in the hot lines with Hinode/EIS by Brooks & Warren (2012). They found that the outflow had a high-speed component, which might be a contributor to the slow solar wind based on the composition (FIP) of the wind. Also they concluded that the released material was previously stored in coronal loops and was released by interchange reconnection between open and closed field lines, which is the scenario in the model. Poletto et al. (2014) estimated the wind energy flux of the order of 10^5 erg cm^{-2} s^{-1}, which for the whole Sun means a 5×10^{32} erg s^{-1} energy output. The polar jet simulation contributes 5×10^{29} erg of energy in about 1.1×10^4 s simulation time through a surface of size 60° in latitude × 100° in longitude; that is, about 7500 erg cm^{-2} s^{-1} flux to the coronal volume. This contribution is about two orders of magnitudes smaller than Poletto's estimated solar

wind energy output.

Assuming fifty jet events, each lasting for 1200 seconds (first blowout of energy occurring at about 10^{29} erg, as Poletto estimated), then fifty modeled polar jets contribute to the energy of the solar wind by about 5×10^{30} erg, which is about 0.5-1% of the overall energy budget needed to maintain the solar wind. We conclude, that having several ongoing jets in both polar and lower latitudinal open flux regions would produce a few percent of the energy flux of the steady-state coronal value, which is similar to the result of Poletto et al. (2014).

2.5 Comparison with Observations

This section focuses only on polar jets. Even though we do not aim to model or reproduce a particular jet observation, we calculate line-of-sight images in the EUV and soft X-ray bands using CHIANTI tables of the temperature response functions of the SDO/AIA and Hinode/XRT instruments, in order to identify structures comparable to actual jet observations. We selected three observations of jets with clear geometric structures and corresponding publications that played a main role in understanding the simulation results. They are the following:

- Jet 1 occurred on 2007 Jan 17 at UT 13:15, was observed by Hinode/XRT, and was studied by Cirtain et al. (2007). We compare the simulations to Hinode/XRT images taken with the Al-poly filter. The temperature where the instrument is the most sensitive is around $T = 6.3 \times 10^6$ K. The original observations showed jets ejecting plasma at sound and Alfvén velocities. It was also suggested that jets are more common structures on the solar surface than suggested before the Hinode observations. These jets lasted longer than the chromospheric ones ($1000 - 2000$ s) and showed transverse oscillations with

larger periodicity (200 s), suggesting Alfvén wave generation during the reconnection processes. These Hinode/XRT observations are part of the many images taken of the south pole during the SoHO/Hinode campaign 7197, analyzed by Savcheva et al. (2007). The resulting statistical study of X-ray polar jet parameters provided invaluable information about the velocity, size, location and duration of jets. This simulation fits into the outward velocity range (70-400 km s^{-1}, sometimes up to 1000 km s^{-1}) and the width range (6-10$\times 10^3$ km) estimated in that statistical study. The reported height range (1-12 $\times$ 10^4 km) strongly depends on the brightness of the ambient coronal plasma, but both the jet model and observations have rather comparable sizes as shown in Figure 2.12. Also in our case, we consider one period of about 700 s. This is within the distribution of the observed jet period interval, which peaked at about 600 s, but ranged between 300 and 2500 s.

- Jet 2 occurred on 2010 Aug 11 at UT 19:00, was observed by SDO/AIA, and was studied by Adams et al. (2014). We compared images in bands 171 Å, 335 Å, and 131 Å, which are respectively sensitive to the following electron temperatures (for emitting ions): $T = 6.3 \times 10^6$ K (Fe IX), $T = 2.5 \times 10^6$ K (Fe XVI), and $T = 4 \times 10^5$ K, 1×10^7 K, and 1.6×10^7 K (Fe VIII, Fe XX, and Fe XXIII). These observations show the difference between the jet models introduced by Moore et al. (2010) and the observed macrospicule jets initiated most likely by converging flows along supergranule edges. Also, they found that the observed blowout jet material most likely was stored within a magnetic arcade before eruption.

- Jet 3 occurred on 2011 May 31 at UT 21:45, was observed by SDO/AIA, and was studied by Chandrashekhar et al. (2014). We use bands 193 Å and 211 Å, which are dominated by emission from plasma at temperatures $T = 1.3 \times 10^6$ K,

2×10^7 K (Fe XII, Fe XXIV) and $T = 2 \times 10^6$ K (Fe XIV), respectively. These observations showed that as plasma flows along loops at the base of the jet, there are manifestations of quasi-periodic plasma ejections. There are transverse or rather torsional motions observed, interpreted as Alfvénic wave propagation with speed over a 100 km s^{-1}. The waves are also strongly damped during propagation, possibly due to a large density gradient between the initial and jet plasma (consistent with the model, see Section 2.4.5).

All synthetic images are generated for the full length of the simulation, every 10 seconds. The dynamics after the first stronger reconnection event are quite periodic. There is plasma spiraling in the disk-view images, and periodicity in the location of bright points in the limb ones. We compare the polar jet model outputs at different simulation times to the selected observations. The images are on the same spatial scale: the model jet is about the size of the observed one in each case. The coronal hole in the model (which simply corresponds to the pole of the dipole field, see Section 2.3) creates a cooler ambient plasma than was observed: the computed coronal brightness is consistently closer to the observed value in the lower temperature bands. This also means that at very high temperature bands (X-ray), it is possible to identify features more easily. Note, that the extending base and the structure of a minifilament are apparent next to the bright spot (at all wavelengths and jets), just as observed by Sterling et al. (2015). However, the model does not produce cooled plasma falling back to the region after ejection as observed (Culhane et al., 2007b), but rather downward flows of the reconnection exhaust. The results are presented in Figures 2.12 and 2.13.

In Figure 2.12, the top row compares the jet model at t = 1h 51m to the observations of Jet 3 made at 21:45:57 UT for the 193 Å band, and the middle row shows comparison at 21:45:49 UT for the 211 Å band. These iron lines are emitted by plasma hotter than 1 MK. In this case, the jet model reproduces the dome shape and the asymmetry in intensity, but its size is about 60% longer than that observed.

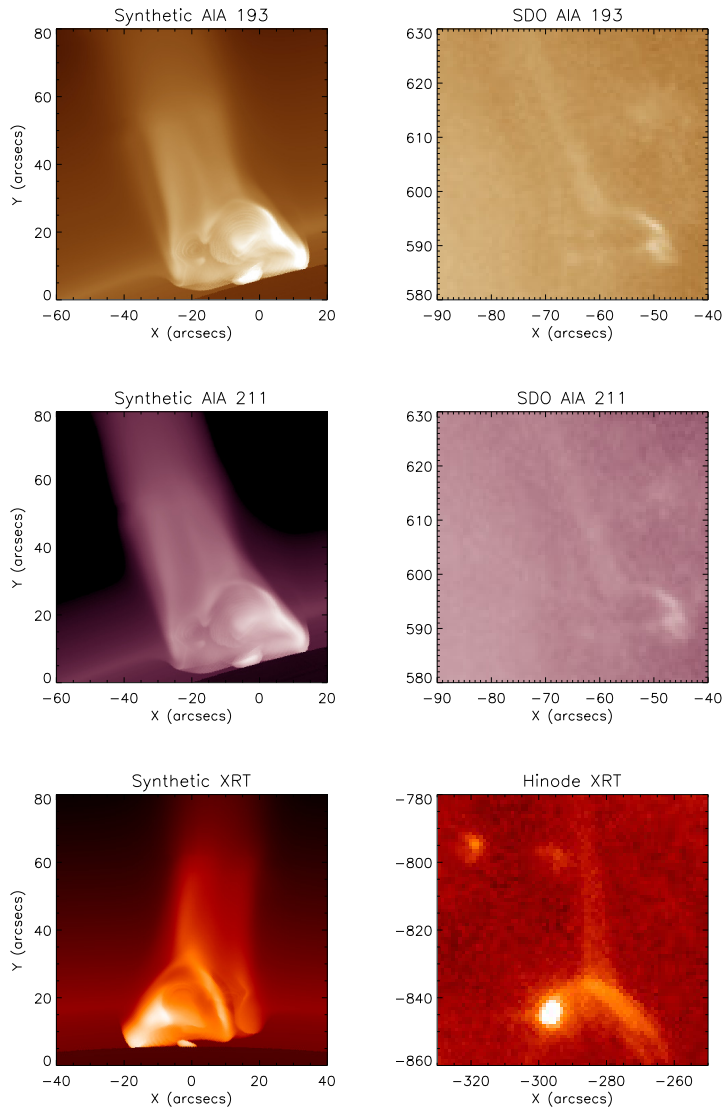

Figure 2.12: Line-of-sight synthetic images of the simulated polar jet (left panels) compared to EUV and Hinode/XRT observations (right panels) of Jet 3 (top and middle rows) and Jet 1 (bottom row). Both images within each pair are shown on the same logarithmic color scale. For further discussion see Section 2.5.

Due to the background and foreground structures in the plasma there is only a weak indication of the jet tail in the observations, unlike in the synthetic images, where the fully open field background is colder. Finally, the two panels in the bottom row show a synthetic X-ray image of the model at t = 1h 22m 40s compared to the observation of Jet 1 by Hinode/XRT with an Al-poly filter at 13:19:07 UT. These images are

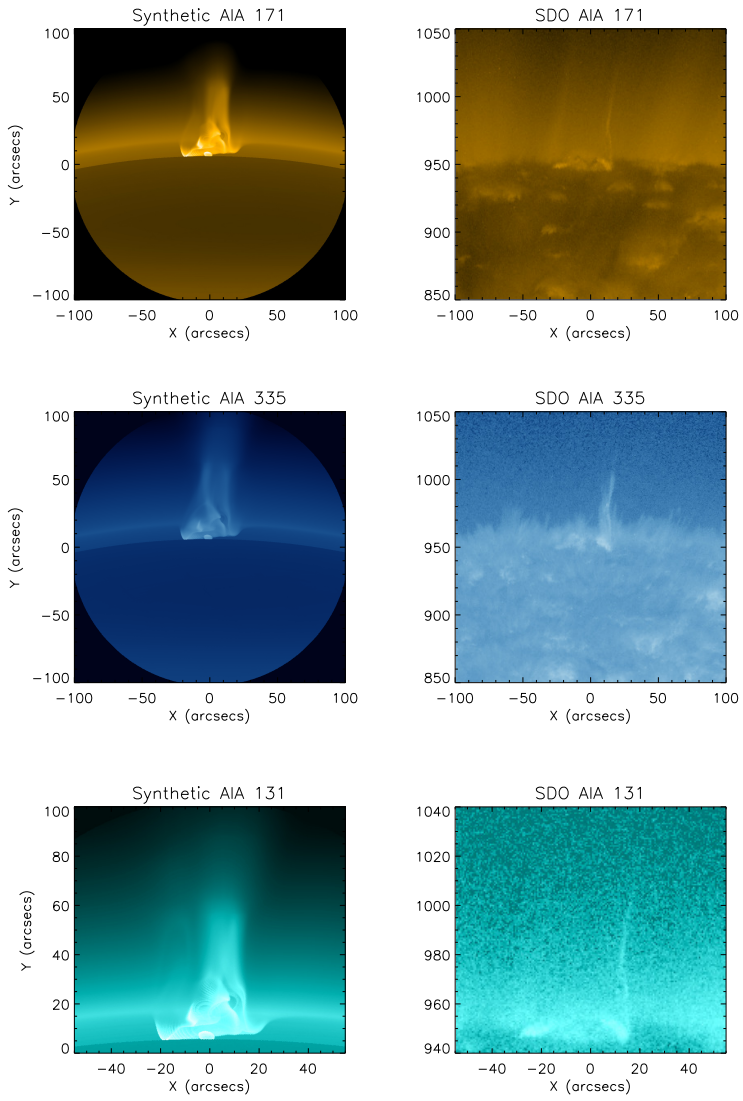

Figure 2.13: Line-of-sight synthetic and observed images in the same layout as Figure 2.12. The EUV observations (right panels) are of Jet 2. For further discussion see Section 2.5.

on the same spatial scale. The dome structure and jet tail are very similar to those observed both in size and in intensity. Also, the bright base on the left is visible and comparable in size on both images.

In Figure 2.13, the top two rows show a comparison of the jet model at t = 2h 29m (left) to Jet 2 at 19:02:13 UT at wavelength 171 Å and at 19:02:17 UT at wavelength

335 Å, corresponding to plasma about 0.6-0.8 MK and 2.5 MK, respectively. Due to the large field of view, the curvature of the solar surface and the ambient coronal plasma are visible. In both bands, the model jet creates a very similar geometry to the observations, especially the size of the dome and the jet's spire. In the bottom row on the left, we show a close-up of the jet model at t = 2h 29m compared to the observation at 19:02:11 UT at wavelength 131 Å. The size of the jet is similar to the SDO/AIA image on the right, and the core brightening and the strong spire on the right side of the jet are showing the same geometric structure. This band is emitted by both cold and hot plasma. The high noise level we see in the observation is due to low counts.

These images show that the jet model reproduces observations with very good qualitative agreement, even though the model is not tailored to any specific event. The agreement is even more remarkable when one considers that the energy buildup process – rotational motions of the chromospheric plasma – is rather simple.

Due to the impulsive nature of the energy release, there are strong temperature gradients in the jet plasma even in the corona. The heating is concentrated in the reconnection region, and then, because the coronal heating is inhibited in the outer corona, the temperature drops relative to the initial value: in the case of the electrons this change is present already in the low corona, in the case of the protons somewhat higher (see Figure 2.11). During the simulation the proton temperature is on the order of 10^7 K during the first bursty reconnection event; then as the periodic behavior settles, the proton temperature remains somewhat smaller, as observed by Chifor et al. (2008b). They observed a maximum temperature about 1.3×10^7 K at the footpoint at the first, bursty jet, and decreasing temperatures later on. As discussed in Section 2.4.2, the electrons are heated later than protons, and to a lower temperature,

due to the model implementation. Therefore the heat is conducted more efficiently in the denser regions than in low-density regions, which results in brighter features in the line-of-sight images close to high-density regions. In Figures 2.12 and 2.13 the model predictions match the high-temperature observation (Hinode/XRT) much better than the low-temperature ones (SDO/AIA 171,SDO/AIA 335). It might be due to the cooler ambient plasma, that contributes to low temperature filters much more than to higher temperature filters. Also, because we do not model these particular jets, the initial plasma conditions (magnetic field strength, electron density) likely differ from the background values of the observations and produce different brightness. The synthetic images exhibit the mixing of bright and dark areas in the jet's core, corresponding to different temperature and density regions. As shown in Figure 2.5, the reconnection regions where heating takes place do not necessarily coincide with the enhanced density regions.

2.6 Conclusions

We implemented a jet model based on rotational boundary motions into an advanced model for the global corona with an idealized initial magnetic field. The heating of the background corona and solar wind is produced by Alfvén-wave dissipation. Using an MHD model with separate electron and ion temperatures, we simulated two events: one located at a high magnetic latitude in an open-field region to form a polar jet, and one at a middle magnetic latitude in a closed-field region to form a loop jet. Both configurations initially produced a strong jet, then exhibited quasi-periodic behavior in their weaker reconnection events and the associated plasma ejections. The polar jet resembles the blowout type with similarities to observations, both in physical parameters and in morphology. In our case, the jet plasma does not create a global-scale shock that would be responsible for the observed heating. Hence we conclude that the heating is due to magnetic energy release at the reconnection site.

We see large-scale perturbations caused by the jet, originating in the chromosphere and propagating out to 24 solar radii within the approximately 3 hours of simulation time. The perturbations involve Alfvén waves plus temperature and density perturbations. The magnetic untwisting loses most of its energy in the low corona (below $2.2R_{\odot}$), but the introduced magnetic perturbation propagates out to $24R_{\odot}$ within 3 hours. Following the first build-up phase, a large reconnection event is observed to be followed by repetitive jetting with periods of about 700 s. We also see hints of another oscillation with a period of about an hour that peaks between $5000-7500$ s and $8000-10000$ s. Due to the shortness of the simulation time it is unclear if that is a sustained phenomenon. Both the observations and the simulations are supporting the theory that interchange reconnection happens between the twisted closed field and the open field. We find that the modeled jets produce large-scale perturbations in the solar wind, and that polar jet signatures (MHD waves) are being carried to large distances in both radial (up to 24 solar radii within 3 hours) and angular (from the pole to the equator) dimensions. Also, the polar jet caused cooling in the outer corona due to the sudden change in plasma properties (density, magnetic-field gradient, and vorticity). Cooling seems counter-intuitive, as reconnection produces heating near the jet. The cooling occurs because the Alfvén wave heating is trapped by the large reflection-rate gradients, resulting in depleted energy deposition in the upper atmosphere. The polar jet signatures in the polar corona can be directly measured by several instruments onboard Parker Solar Probe, which by reaching as far down as 10 solar radii, will be directly traveling through the jet perturbations. This study provides several observables (for example large gradients in density and temperature) that can be directly measured by the Parker Solar Probe instruments.

Many questions are left open to be addressed in follow-up work. First, as men-

tioned in Section 2.1, Shimojo et al. (2007) observed that some jets cause loop brightening at the other end of the loop along closed magnetic field lines. Second, to understand the connection between the periodicity of plasma rotation and reconnection events, a parameter study would be necessary; this will also be carried out in the future. Third, the introduced numerical resistivity may have a significant effect on the amount of twist being stored between the reconnection events. We hope to address this question in the future, using the already available fifth-order scheme implemented by Chen et al. (2016). Finally, the results suggest that jets do not contribute significantly to the solar wind, but are important contributors to plasma waves in the corona. As Liu et al. (2015) proposed, jets might trigger larger events, for example CMEs. In that case, jets play important roles even in forming space weather. This is an interesting scenario that we will explore in a future study.

CHAPTER III

Synthetic Spectrum

3.1 Introduction

Spectroscopic observations are highly sensitive to the thermal and dynamic properties of plasmas. Therefore, spectroscopy is a key diagnostic tool for studying the solar atmosphere (Cranmer et al., 2015, 2017). In this chapter, we describe the new SPECTRUM tool, which allows us to produce high-resolution spectra for studies of physical processes and validation studies.

Synthetic spectra based on the AWSoM model have been studied using isotropic proton and electron temperatures by Oran et al. (2017), showing good agreement with line widths and fluxes of a few spectral lines measured by the Solar Ultraviolet Measurements of Emitted Radiation on board the Solar & Heliospheric Observatory (SoHO/SUMER; Wilhelm et al., 1995), suggesting that the change in effective velocity along radial distance is indeed due to wave damping. To be able to perform similar studies on-demand and efficiently, we developed the parallel Fortran 90 code SPECTRUM as part of SWMF. SPECTRUM's main goal is to produce synthetic observations of any high-resolution spectra from any instrument, similarly to one of the capabilities of the FORWARD package (Gibson, 2014; Gibson et al., 2016).

In AWSoM, the corona is maintained in a physically self-consistent manner based on the Alfvén wave dissipation (see van der Holst et al., 2014). SPECTRUM can

calculate nonthermal broadening of spectral lines based on the local Alfvén wave energy density, which allows testing and/or validating the Alfvén wave heating theory against observations. Because significant temperature anisotropy is observed in the solar wind (Cranmer et al., 2007), we developed SPECTRUM so it can process AWSoM simulation results with isotropic electron and anisotropic proton temperatures (Meng et al., 2015). In Section 3.2, we describe the process of line formation and the AWSoM solar corona model. In addition to synthetic spectra, SPECTRUM calculates differential emission measure (DEM) and emission measure (EM) directly from the model output. The algorithms of SPECTRUM are discussed in Section 3.3. Section 3.4 shows AWSoM comparisons to observations, and finally Section 3.5 summarizes. The content of this chapter is in preparation for publication.

3.2 Synthetic Spectra

First, we describe the physical processes of line formation which are taken into account in these calculations, and then introduce briefly the AWSOM solar corona model we use to obtain the plasma parameters for the presented synthetic spectral calculations.

3.2.1 Line Formation

In the synthetic spectral calculations, we consider only the mechanisms building the solar coronal spectrum as discussed in Phillips et al. (2008). Because the coronal model we are working with models the Sun from 50,000 K and above (mid-chromosphere), the synthetic spectral calculations are going to be performed on coronal plasmas, which are optically thin and collisionally excited (including cascades). Absorption, resonant scattering, and continuum radiation are neglected. It is assumed that the plasma is in ionization equilibrium, which means that sudden energetic processes, such as flares for example, are not taken into account.

Individual ions emit in a Lorentzian profile, and due to the Maxwellian velocity profile of thermal ions, the line-of-sight integration of these thermally broadened spectral lines can be described with the Voigt profile, which is approximated by a Gaussian in the case of weak wings (for details see Phillips et al., 2008). Overall, the sum of all emitted photons in a given volume element dV, assumed to be homogeneous, results in a line profile that can be approximated with a Gaussian. The Gaussian line profile of the line emission centered at wavelength λ_0 an be written as:

$$\phi(\lambda) = \frac{1}{\sqrt{2\pi}\Delta\lambda} e^{-\left(\frac{\lambda-\lambda_0}{2\Delta\lambda}\right)^2}, \tag{3.1}$$

where $\Delta\lambda$ is the line width of the emission line. The width of the line can be described with the full width at half maximum (FWHM) that is related to the standard deviation $\Delta\lambda$ as FWHM $= \sqrt{8\ln 2}\Delta\lambda$. FWHM is given by

$$\text{FWHM} = \frac{\lambda_0}{c_{light}} \sqrt{8\ln 2 \left(\frac{k_B T_i}{M} + v_{nth}^2\right)}, \tag{3.2}$$

where c_{light} is the speed of light in vacuum (3×10^8 m s^{-1}), k_B is the Boltzmann constant $\left(1.38 \times 10^{-23}\ \text{m}^2\text{kg s}^{-2}\text{K}^{-1}\right)$, T_i is the ion temperature, and M is the ion mass of the emitting ion. The thermal line broadening can be expressed as $\left(\frac{\lambda_0}{c}\right)\left(\frac{2k_B T_i}{M}\right)^{\frac{1}{2}}$, and v_{nth} is the nonthermal broadening term that results from the Alfvén wave energy densities in the AWSoM simulations.

A dV volume element at d distance from the observer along the line of sight (LOS) containing ion X_j^{+m} with density $N\left(X_j^{+m}\right)$ emits dF at frequency ν_{ij} at transition j to i, where $dF = \frac{1}{4\pi d^2} N\left(X_j^{+m}\right) A_{ji} h\nu_{ij} dV$ energy per unit area and unit time and A_{ji} is the Einstein coefficient. The total flux that reaches the detector is calculated

by integrating the emission from the individual volume elements along the LOS:

$$F = \frac{1}{4\pi d^2} \int_V N\left(X_j^{+m}\right) A_{ji} h\nu_{ij} dV. \tag{3.3}$$

The density of the emitting ions $N\left(X_j^{+m}\right)$ in Equation 3.3 can be written as the product of relative level population $\frac{N\left(X_j^{+m}\right)}{N(X^{+m})}$ (calculated from the balance between excitation and de-excitation processes relative to level i, assuming equilibrium), the relative ion population $\frac{N\left(X^{+m}\right)}{N(X)}$ (obtained from solving the equations describing the ionization-recombination processes, assuming ionization equilibrium) the element's abundance relative to hydrogen $\frac{N(X)}{N(H)}$ (based on measurements), the ratio of hydrogen to free electrons $\frac{N(H)}{N_e}$ (which is about 0.83 due to the electrons originating from heavy ions and completely ionized He at the temperatures covered by AWSoM), and electron density N_e. Defining the contribution function as

$$G\left(T_e, N_e\right) = \frac{N\left(X_j^{+m}\right)}{N\left(X^{+m}\right)} \frac{N\left(X^{+m}\right)}{N\left(X\right)} \frac{N\left(X\right)}{N\left(H\right)} \frac{N\left(H\right)}{N_e} \frac{A_{ij}}{N_e} h\nu_{ij}, \tag{3.4}$$

the observed flux can be written simply as

$$F = \frac{1}{4\pi d^2} \int_V G\left(T_e, N_e\right) N_e^2 dV. \tag{3.5}$$

The F integral for each line along the LOS has to be calculated to obtain the full synthetic spectra of the simulation results. This is done by using the plasma parameters predicted by AWSoM to calculate both $G\left(T_e, N_e\right)$ and the line profile as described in Section 3.3.1.

3.2.2 Solar Corona Model

The SPECTRUM post-processing tool uses AWSoM simulation results as input data for synthetic spectral calculations. In principle it is possible to use the output of

any MHD corona model, but SPECTRUM is designed to make processing AWSoM output simple and direct. The results in this chapter are produced with the three-temperature AWSoM model, which is described in detail in Section 1.3. This model can solve for anisotropic proton and isotropic electron temperatures. This feature can be very important for calculating high-resolution synthetic spectra based on local electron temperature and taking into account the line-of-sight direction relative to the local magnetic field direction.

The magnetic boundary condition is based on synoptic magnetograms produced by the National Solar Observatory, Global Oscillation Network Group (NSO/GONG), and the plasma boundary is set to $n = 3 \times 10^{10}$ cm^{-3} and $T = 5 \times 10^4$ K at $1.001 R_\odot$. For the governing equations see van der Holst et al. (2014).

In this chapter, simulations of Carrington Rotations 2063 (CR 2063, between 2007-11-04 and 2007-12-01) and 2082 (CR 2082, between 2009-04-05 and 2009-05-03) are performed. We chose these time intervals because of their low solar activity. Figure 3.1 shows the steady-state solution for density, radial speed and the effect of temperature anisotropy in Figure 3.2 on the meridional cut plane from the view of the line-of-sight direction.

While at the base of the domain the plasma is isotropic due its high density, there is a strong temperature anisotropy in the low coronal region where collisions are not sufficient to equate the temperatures. As standard model validation, we compare the simulation results to line-of-sight narrow-band imager observations and also with 1 AU solar wind plasma measurements. Here we use observations by the Extreme Ultraviolet Imaging Telescope aboard the Solar & Heliospheric Observatory (SoHO/EIT; Delaboudinière et al., 1995), and OMNI (King & Papitashvili, 2005) composite data set, respectively. Figure 3.3 shows the steady-state solution compared to respective observations using 2D narrow band images. The images were taken with the *Al+1* filter, 12 and 13 s exposure times. The BATS-R-US images are reproduc-

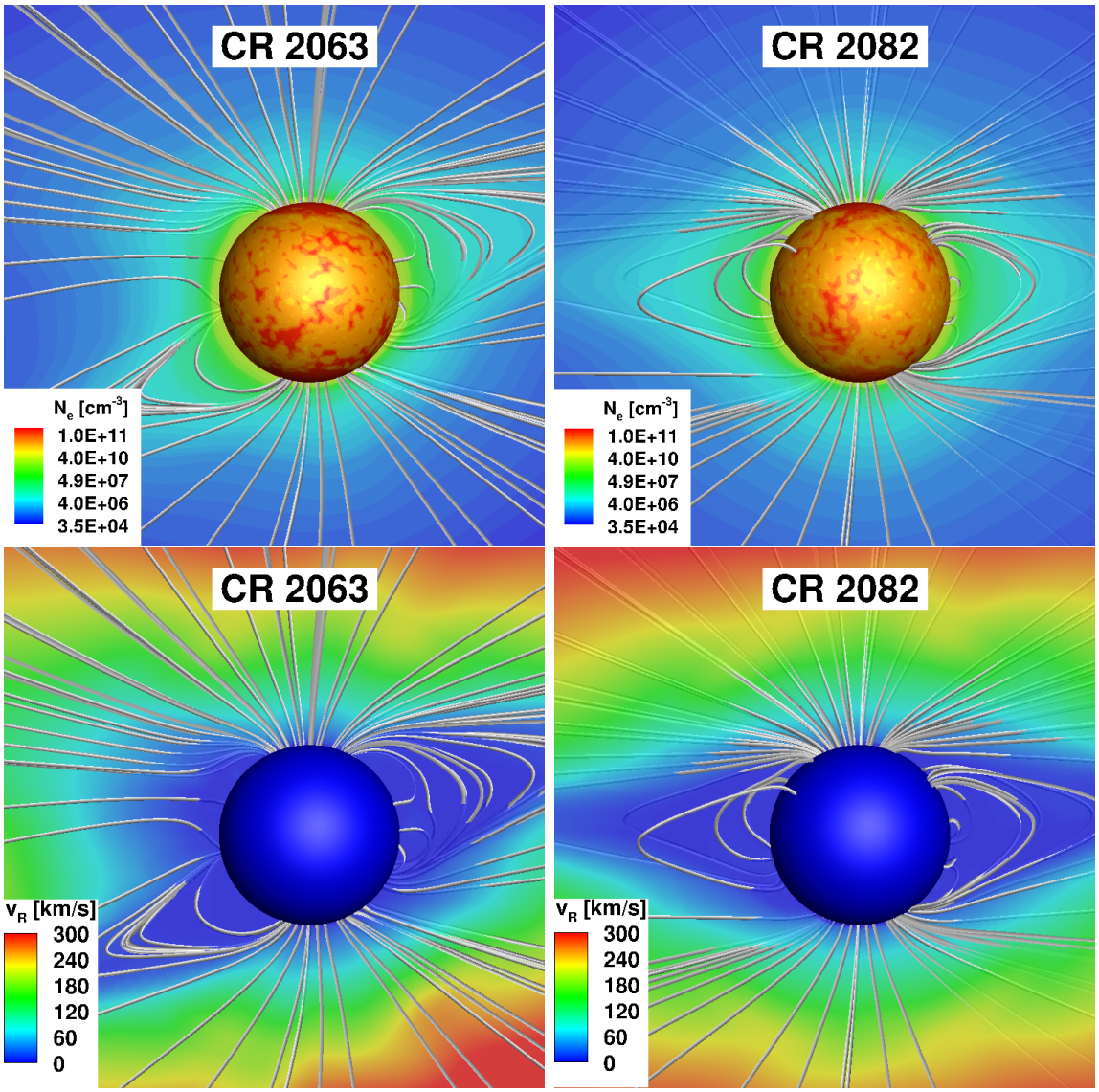

Figure 3.1: AWSoM steady-state simulation results of CR 2063 (*left*) and CR 2082 (*right*), showing electron density in the top row and radial bulk speed in the bottom one in a cut-plane viewed from the LOS direction, along with a similarly contour-colored 1.002 solar radii spherical surface of the solar body. The field of view is 6 solar radii in each image.

ing observations for the *clr* filter, which might add to the difference in the results.

Figure 3.4 shows in-situ data comparison for plasma observations taken at 1 AU.

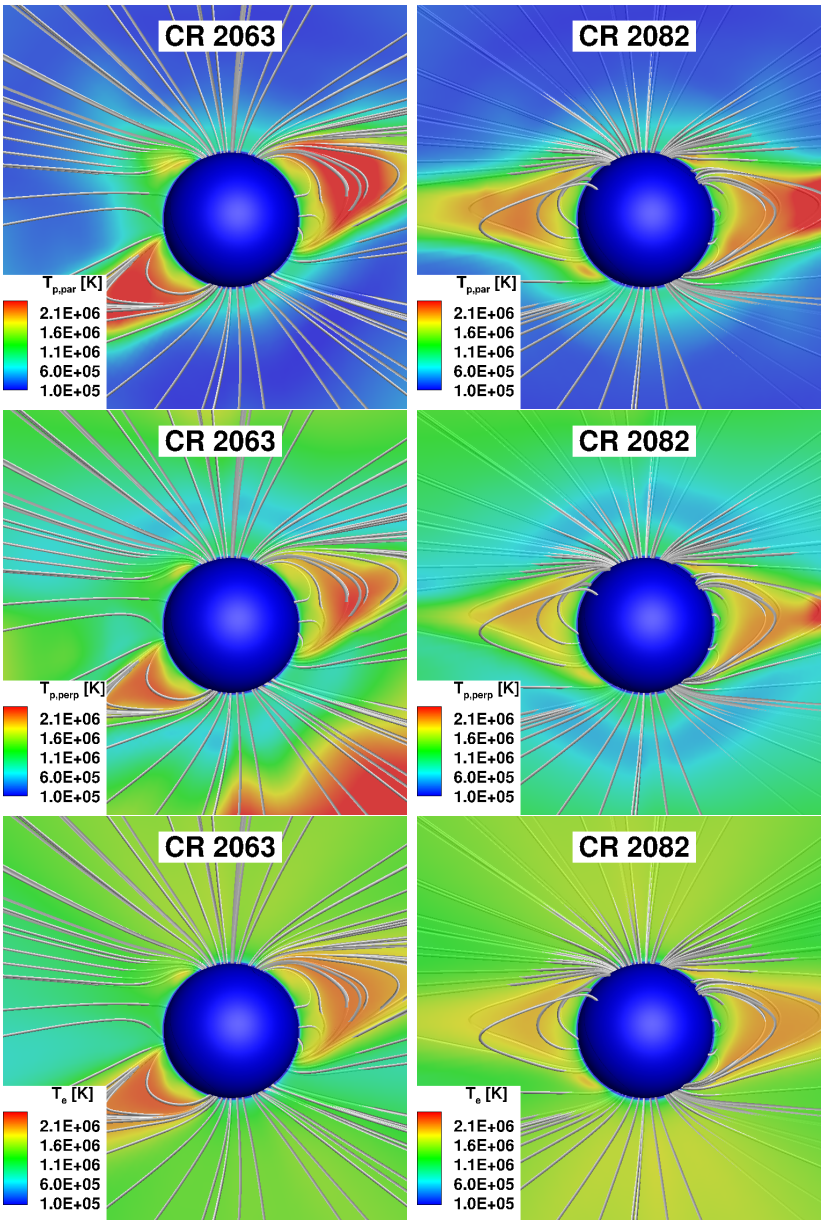

Figure 3.2: AWSoM steady-state simulation results of CR 2063 (*left*) and CR 2082 (*right*) respectively, showing parallel proton (top row), perpendicular proton (middle row), and electron temperatures (bottom row). A cut-plane from the LOS direction is shown, along with a similarly contour-colored 1.002 solar radii spherical surface of the solar body. The field of view is 6 solar radii in each image.

3.3 SPECTRUM Implementation

SPECTRUM is a post-processing synthetic spectral calculation tool, written in Fortran (it is optional to run parallelized), implemented within the Space Weather

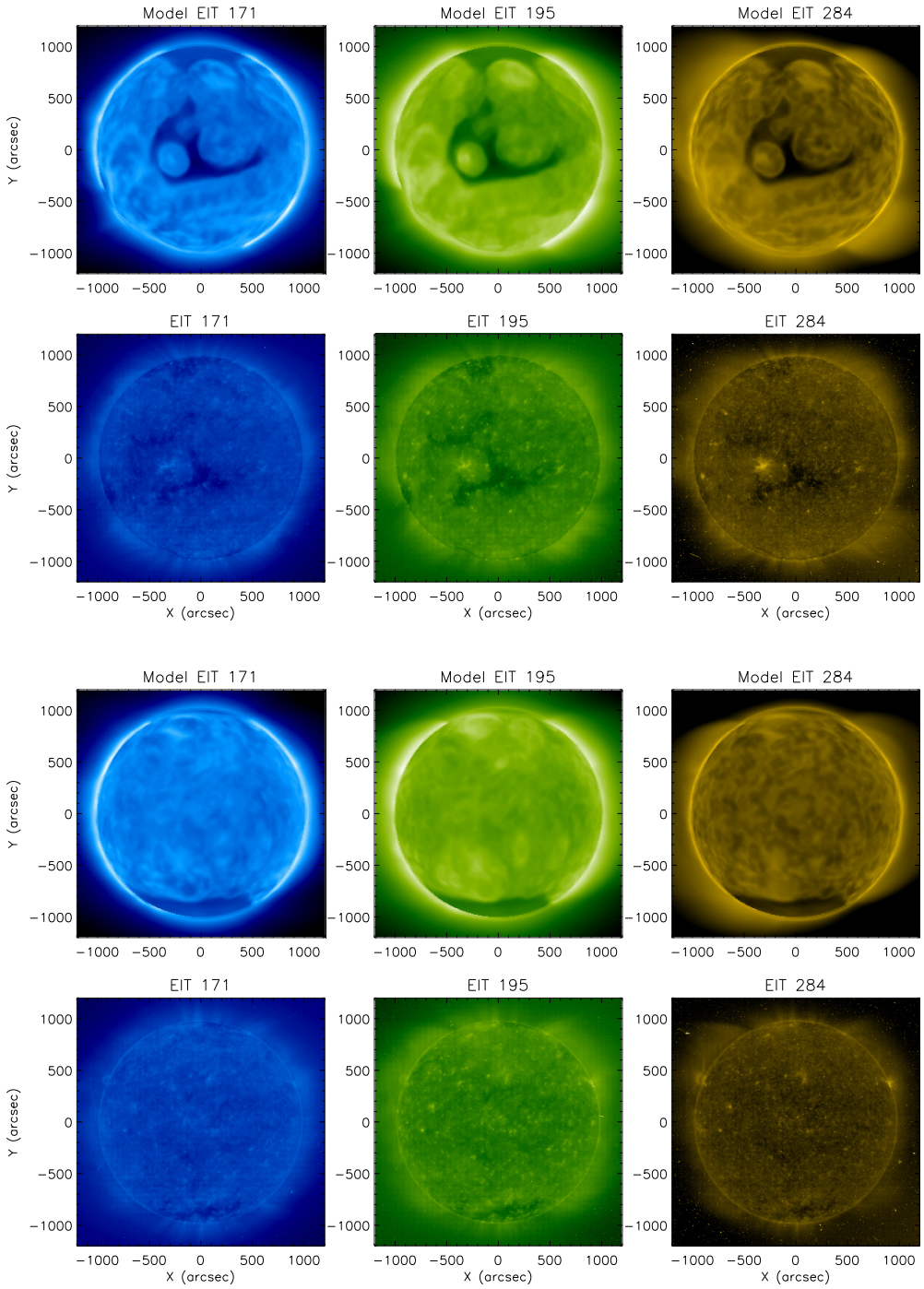

Figure 3.3: *From top to bottom:* Model validation of AWSoM steady-state simulation results of CR 2063 and CR 2082 respectively, comparing line-of-sight SoHO/EIT observations to synthetic images.

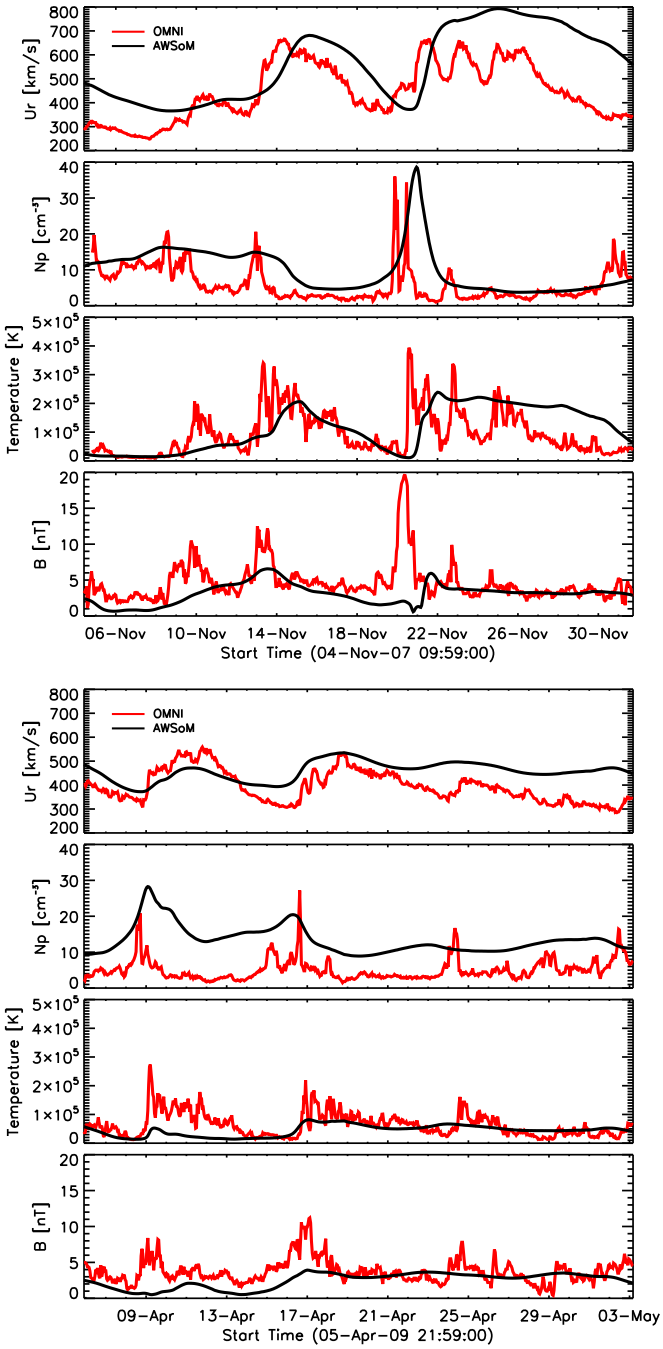

Figure 3.4: *From top to bottom:* Model validation of AWSoM steady-state simulation results of CR 2063 and CR 2082 respectively, comparing OMNI 1 AU in-situ plasma measurements (*red*) with simulated data sampled at the same location of the domain (*black*).

Modeling Framework (SWMF, Tóth et al., 2012), which is publicly available at the `http://csem.engin.umich.edu/Tools/SWMF` website. SPECTRUM uses MHD

simulation output data to calculate synthetic spectra based on CHIANTI (Dere et al., 1997; Del Zanna et al., 2015) emissivities. The user can control the parameters of spectral calculations via editing the commands of the input text file.

SPECTRUM produces synthetic spectra and synthetic DEM and EM data files using any MHD model output files, which contain the information needed to perform the calculations, as described in Section 3.3.1. Due to this flexibility, it is easy for SPECTRUM to provide observables for any spectroscopic, spectral- or narrow-band imager observation by prescribing the wavelength intervals and the wavelength resolution of the instrument to be used. Because of the natural assumption that SPECTRUM is used for solar coronal data analysis, the cells inside the solar body and behind the solar disk are automatically ignored in the following calculations.

The contribution function values (Equation 3.4) needed for emission calculations (Section 3.2.1) are obtained by an IDL script that uses procedures from the CHIANTI package. The logarithms of contribution function values are stored on a logarithmic density-temperature grid in an ASCII file. Both the tabulated values and the IDL program used to generate the table are available in the SWMF.

The input plasma data comes from data file (MHD simulation output) that contains the following information: plasma density, bulk velocity vector components, magnetic field vector components, plasma pressure or temperature (optional to have separate electron- and proton temperatures and anisotropic proton temperatures), backward- and forward propagating Alfvén wave energy densities, and the angles that describe the rotation that transforms the coordinate system of the simulation domain into the coordinate system aligned with the observer's LOS. (The observer's position is described in the command that saves the extracted data during the solar corona simulation.)

The data file is assumed to be on a uniform Cartesian grid. It is also possible to use uniform plasma parameters for testing purposes, by simply prescribing the

above listed variables in the input file. We use uniform plasma parameters (single temperature and density) to validate the spectral calculations against CHIANTI 8.0 uniform plasma calculations. The results of one of the validation comparisons are shown in Figure 3.5, using T = 10^6 K temperature and N_e = 10^8 cm^{-3} electron number density.

3.3.1 Synthetic Spectral Calculation

The CHIANTI table of $G(T_e, N_e)$ values is calculated on a temperature-density grid in the following steps. First, we calculate the emissivity:

$$G_{em} = \frac{h\ c}{\lambda} N\left(X_j\right) A_{ji}, \tag{3.6}$$

where $h\ c = 1.986 \times 10^{-8}$ erg Å, λ is in Ångström, $N\left(X_j\right)$ is the number density of ions in the upper emitting level j, and A_{ji} is the Einstein coefficient of the spontaneous radiative decay rate for the transition. Then G_{em} is multiplied with the element abundance (relative to hydrogen) from the abundance file *sun_coronal_1992_feldman.abund* stored in SolarSoft's CHIANTI package based on Feldman et al. (1992):

$$G_{rem} = G_{em} \frac{N\left(X\right)}{N\left(H\right)}. \tag{3.7}$$

The choice of element abundances is important when studying different coronal structures. For example, the abovementioned Feldman abundances are better for describing the plasma within closed field structures than in coronal holes. It is possible to use any of CHIANTI's abundance distributions, and calculate spectra based on these different tables. The implementation gives the freedom to use any user-defined or simulated non-equilibrium ion fraction, in preparation for a multi-fluid AWSoM model. The relative emissivity is multiplied by the fractional abundance of the ion in

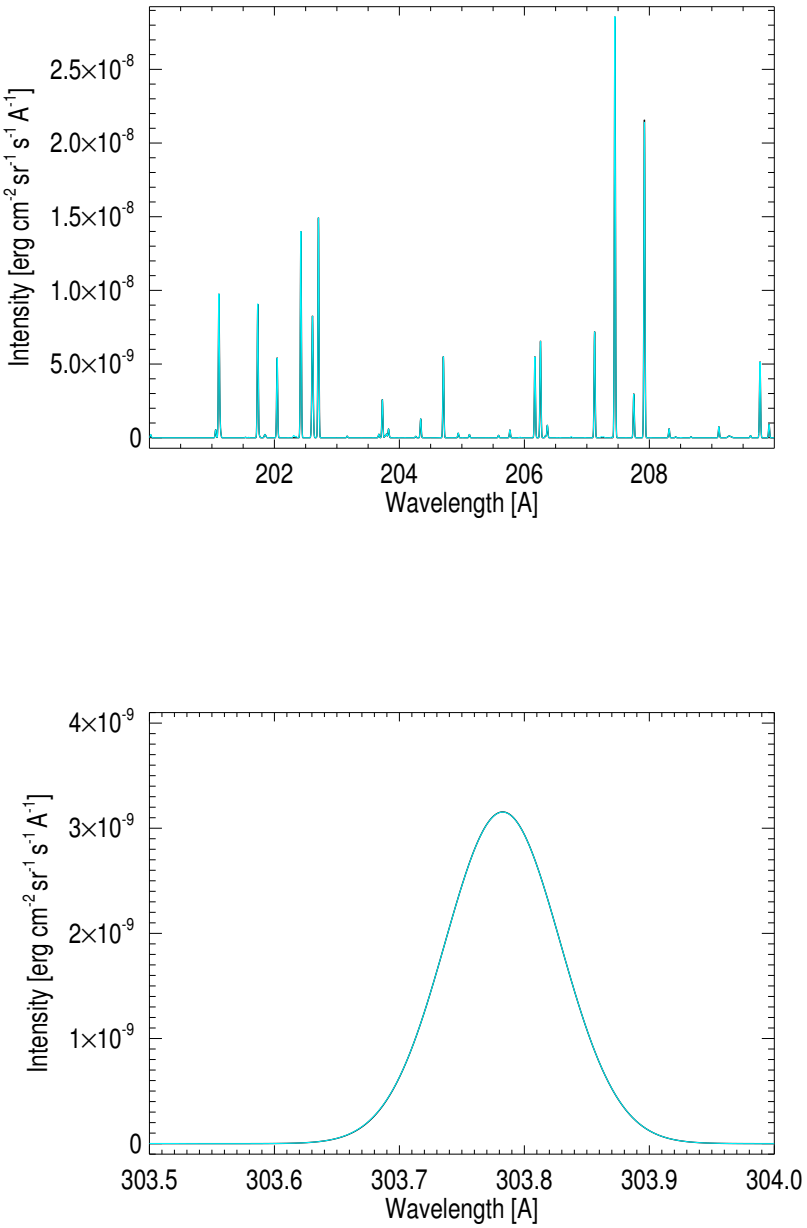

Figure 3.5: Spectral calculation validation of uniform density, isothermal plasma input from SPECTRUM (black) compared to CHIANTI's synthetic spectral calculation (turquoise).

ionization equilibrium to obtain the tabulated values of:

$$G = G_{rem} \frac{N\left(X_j\right)}{N\left(X\right)} \frac{1}{N_e}. \tag{3.8}$$

In the input file, the user can specify whether or not to use unobserved lines (lines that correspond to theoretically possible transitions between levels but have not been observed yet), calculate with Doppler-shift due to bulk plasma motion, and/or include nonthermal broadening due to Alfvén waves. The user can also select a certain instrument's resolution and wavelength intervals, or directly prescribe the wavelength interval(s) of interest along with the wavelength resolution. To calculate the Doppler shift, the wavelength intervals are extended by 10% in case some lines would shift outside or into the specified wavelength range. SPECTRUM loops over all lines from the contribution function ($G\left(T_e, N_e\right)$) table, and if they are within the wavelength interval of interest, it calculates the emission at that particular wavelength within the plasma data's grid in a cell-by-cell manner. (All cells behind the disk or inside the solar body are already excluded from the calculations, as mentioned in Section 3.3.)

Next, SPECTRUM performs the following calculations line by line for each cell of the simulated solar coronal data, then sums the results along the LOS direction for each cell. First, the Doppler shift is applied to the line and the shifted line is placed on the wavelength grid:

$$\lambda_{shifted} = \left(1 - \frac{u_{los}}{c_{light}}\right) \lambda, \tag{3.9}$$

where u_{los} is bulk plasma velocity's LOS component, positive towards the observer, and c_{light} is the speed of light (3×10^8 m s^{-1}). Second, the thermal and nonthermal line broadenings are calculated. The thermal broadening is calculated taking into account temperature anisotropy:

$$v_{th}^2 = \frac{k_B T_{LOS}}{m_{proton} A_{ion}}, \tag{3.10}$$

where k_B is the Boltzmann constant, the line-of-sight temperature is calculated as $T_{LOS} = \sin^2 \alpha T_{perp} + \cos^2 \alpha T_{par}$, where the angle between the line-of-sight and the

magnetic field direction is $\cos\alpha = |\mathbf{B}\cdot\mathbf{e}_{LOS}/B|$. For Alfvén waves, the kinetic and magnetic energies of the fluctuations $\frac{1}{2}\rho\delta\mathbf{u}^2$ and $\frac{1}{2\mu_0}\delta\mathbf{B}^2$ are approximately of the same magnitude, so

$$\frac{1}{2}\rho\delta\mathbf{u}^2 + \frac{1}{2\mu_0}\delta\mathbf{B}^2 = \rho\delta\mathbf{u}^2 = \omega_+ + \omega_- = \frac{1}{4}\rho\left(z_+^2 + z_-^2\right). \tag{3.11}$$

Nonthermal broadening due to low-frequency Alfvén waves in the two transverse directions is calculated as

$$v_{nth}^2 = \frac{1}{4}\langle\delta u^2\rangle\sin^2\alpha = \frac{1}{4}\frac{\omega^+ + \omega^-}{\rho}\sin^2\alpha = \frac{1}{16}\left(z_+^2 + z_-^2\right)\sin^2\alpha. \tag{3.12}$$

where $z_\pm$ are the Elsässer variables for forward- and backward-propagating waves with energy densities $\omega_\pm$. See (Oran et al., 2017, See)[for details.] The instrumental broadening ($\Delta\lambda^2_{instrument}$) can also be added to the calculation at the user's request. The total line broadening is the sum of thermal and nonthermal components:

$$\Delta\lambda^2 = \lambda^2\frac{u_{th}^2 + u_{nth}^2}{c_{light}^2} + \Delta\lambda^2_{instrument}. \tag{3.13}$$

As mentioned in Section 3.2.1, SPECTRUM calculates local electron density assuming a $1:0.83$ electron-to-proton ratio ($c_{ep} = 0.83$): $N_e = \frac{\rho}{c_{ep}m_{proton}}$. Finally, the monochromatic intensity component for the line is calculated using the previously obtained components:

$$I_{total} = \frac{1}{4\pi d_{1AU}^2}N_e^2 G_{int}\frac{dV}{d\Omega}, \tag{3.14}$$

where the solid angle of surface area $dydz$ at distance $1AU$ is $d\Omega = \frac{dydz}{d_{1AU}^2}$. To obtain

the full line profile, the line is dispersed on the wavelength grid. The Gaussians are truncated at $\pm 5\sigma$ for efficiency. Hence

$$I(\lambda) = I_{total} \frac{1}{\sqrt{2\pi}\Delta\lambda} e^{-\frac{\lambda_{Dist}^2}{\Delta\lambda^2}}, \tag{3.15}$$

where $\lambda_{Dist} = \lambda_{shifted} - \lambda_{Bin}$ is the distance between the actual Doppler-shifted wavelength and the center of the bin on the wavelength grid and $\Delta\lambda$ is the line broadening. SPECTRUM sums $I(\lambda)$ along the LOS cells and stores them in a grid with the chosen wavelength-spatial dimensions. The above calculations are repeated for each grid point, then SPECTRUM moves to the next line, and then finally saves the results. For the sake of computational speed, the lines can be distributed over many CPU cores and the calculations can be performed in parallel using the MPI library. These calculations produce output files containing the 1, 2, or 3 dimensional spectrum data, where the first dimension is the wavelength, and the second and third ones are spatial dimensions of the plane of the sky. For testing and diagnostics purposes, it is also possible to restrict the calculations to one line, or to one cell only.

An important feature of SPECTRUM is that line formation can be studied by separating thermal and nonthermal effects, Doppler effects, and temperature anisotropy effects, giving the opportunity to identify spatial locations where these effects dominate along the LOS direction. In this way SPECTRUM provides a formidable tool to interpret spectral observations in terms of the properties of different plasmas located at different places along the LOS.

3.3.2 DEM and EM Calculation

DEM and EM calculations can be performed independent of calculating spectra. SPECTRUM calculates

$$\mathrm{DEM}\,(T_e) = \sum_i \frac{N_e^2 dx_i}{dT_e}, \tag{3.16}$$

and

$$\mathrm{EM}\,(T_e) = \sum_i N_e^2 dV_i, \tag{3.17}$$

where T_e is electron temperature, T_p is proton temperature, dx is the size of the cell along the LOS, dV is the volume of the cell, and dT_e is the cell size on the logarithmic temperature grid. As mentioned in Section 3.2.1, the electron number density N_e is calculated assuming that the proton density is 0.83 times the electron one. The results are stored in a one-dimensional dataset on the logarithmic temperature grid.

3.4 Comparison with Observations

In this section comparisons to coronal observations done by the EUV Imagig Spectrometer for Hinode (Hinode/EIS; Culhane et al., 2007a) are shown. We chose quiet Sun observations from the end of solar cycle 23 and from the beginning of solar cycle 24. The first two observations are from CR 2063: one in a closed magnetic field region on the solar West limb taken at 2007-11-04UT19:12:27, and one in an open magnetic field region above the North coronal hole measured at 2007-11-12UT12:32:02. The third observation site is of CR 2082 in the open magnetic field region of the South coronal hole, collected at 2009-04-23UT12:08:15. All three observation sites are shown as white rectangles in the narrowband images taken by SoHO/EIT in Figure 3.6. The Hinode/EIS spectral resolution is 0.0223 Å in two wavelength bands

(170 - 210 Å and 250 - 290 Å). All three observations were done with the 2" slit in raster mode. We obtained the synthetic plasma data with the three-temperature

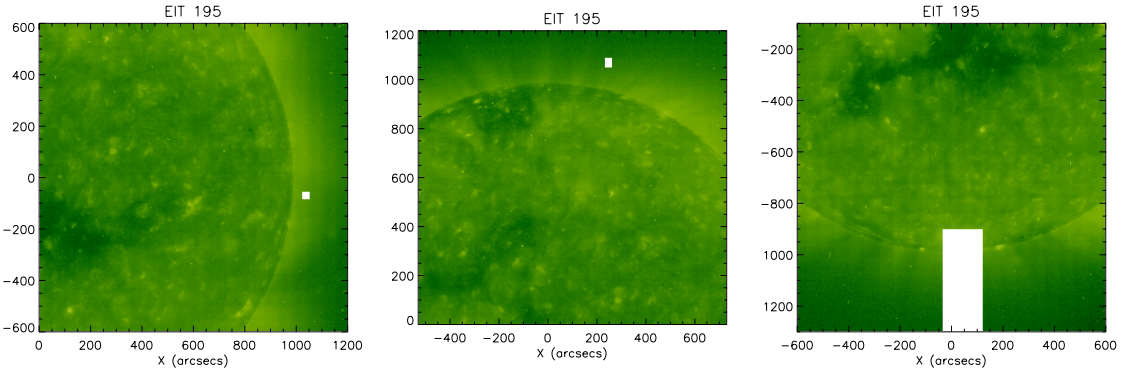

Figure 3.6: *From left to right:* White boxes show the Hinode/EIS observation sites of CR 2063 and CR 2082 on SoHO/EIT narrowband images.

AWSOM model. Using GONG synoptic magnetograms on the inner boundary as magnetic field boundary condition, after 60,000 iterations there is a steady-state solar wind solution on the domain (from the chromosphere to 24 solar radii). We show the comparison of the simulation results to observations by producing both synthetic EUV LOS images (which are in these cases taken by SoHO/EIT), and 1 AU in-situ plasma measurements (see Figure 3.3). The input data is extracted for SPECTRUM from the steady-state plasma solutions at the original Hinode/EIS observational sites, shown in Figure 3.7. Synthetic spectral observations and EM/DEM distributions of the following data sets have been produced (in the following x is in the LOS direction of the observer, z points towards North and y completes a right-hand coordinate system, units are in solar radii):

1. *West limb observation [CR 2063]:* Box shown in the first panel in Figure 3.7 centered at (x=0, y=1.1, z=-0.0556), with dimensions (3, 0.013, 0.013) along the (x,y,z) axes.

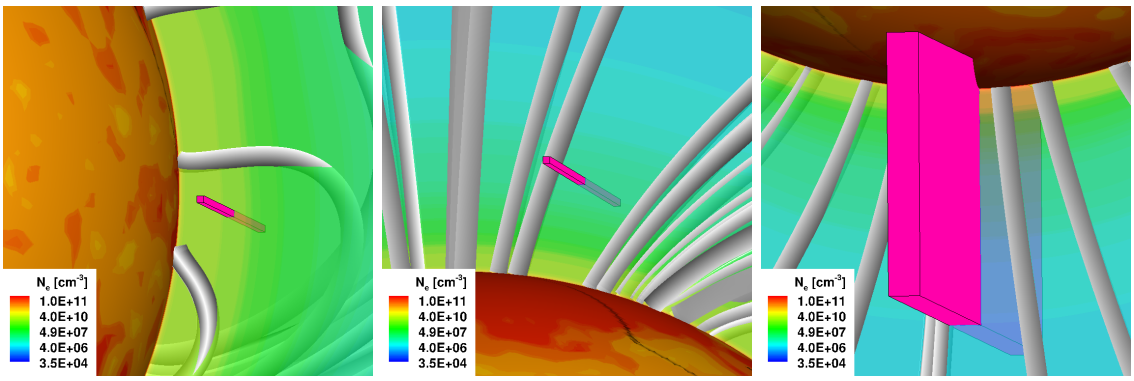

Figure 3.7: *From left to right:* Magenta boxes represent the three data boxes where the MHD solution data were extracted for synthetic spectral calculations corresponding to observation sites of CR 2063 and CR 2082 with field of view 0.8 solar radii.

2. *North pole observation [CR 2063]:* Box shown in the middle panel in Figure 3.7 is centered at (x=0, y=0.2556, z=1.1678), with dimensions (3, 0.013, 0.013) along the (x,y,z) axes.

3. *South pole observation [CR 2082]:* Box shown in the third panel in Figure 3.7 is centered at (x=0, y=0, z=-1.2), with dimensions (6, 0.03, 0.5) along the (x,y,z) axes.

In the following we show a representative sample of SPECTRUM data outputs. The first two observations will be discussed as comparisons of spectra produced in open- and closed magnetic flux regions, and the third observation will be used to calculate the nonthermal velocity distribution as a function of radial distance for selected emission lines. As mentioned by Hahn et al. (2012), the effective velocity trends are insensitive to the assumption of position-varying or fixed instrumental widths, so we used fixed instrumental broadening of 0.06 Å for both wavelength intervals, which is an estimated average for both intervals.

3.4.1 Open and Closed Magnetic Field Regions

In this section AWSoM simulation results are compared to Hinode/EIS observations of CR 2063. Figure 3.8 shows the EM and DEM comparisons of the coronal plasma. The difference between the observed and modeled corona shows that the

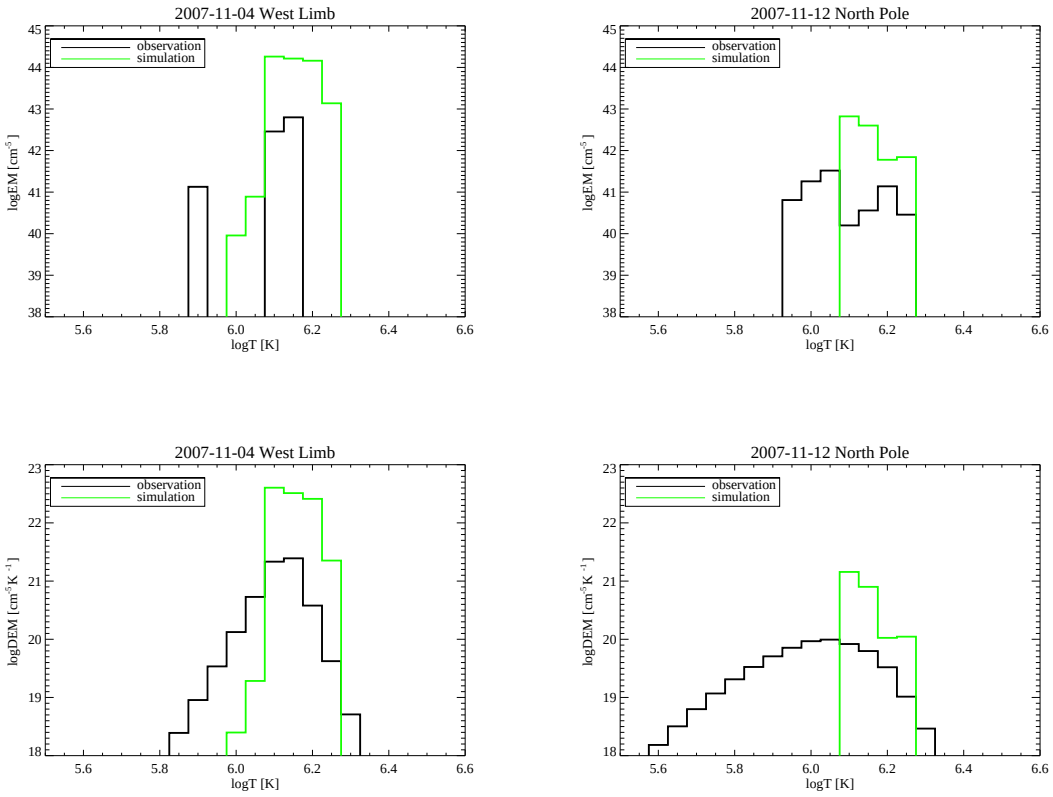

Figure 3.8: Coronal EM (*up*) and DEM (*down*) of observed *(black)* and simulated *(green)* coronal plasmas in closed *(left)* and open *(right)* magnetic field regions are shown.

model is denser, and warmer overall in the low corona. Based on this result, we expect that the spectra will be brighter, and that the lines forming at low temperatures while overpredicted, and warmer lines are better predicted, depending on the local temperature. Also, because we use exclusively abundances corresponding to closed magnetic coronal regions, the low-FIP ions (for example Fe) will be even more overpredicted for this reason, by a factor of 4.

Figure 3.9 and Figure 3.10 show the comparison between the observed and synthetic spectra in both open and closed magnetic field regions. The predicted spectra are scaled down by about a factor of 10.

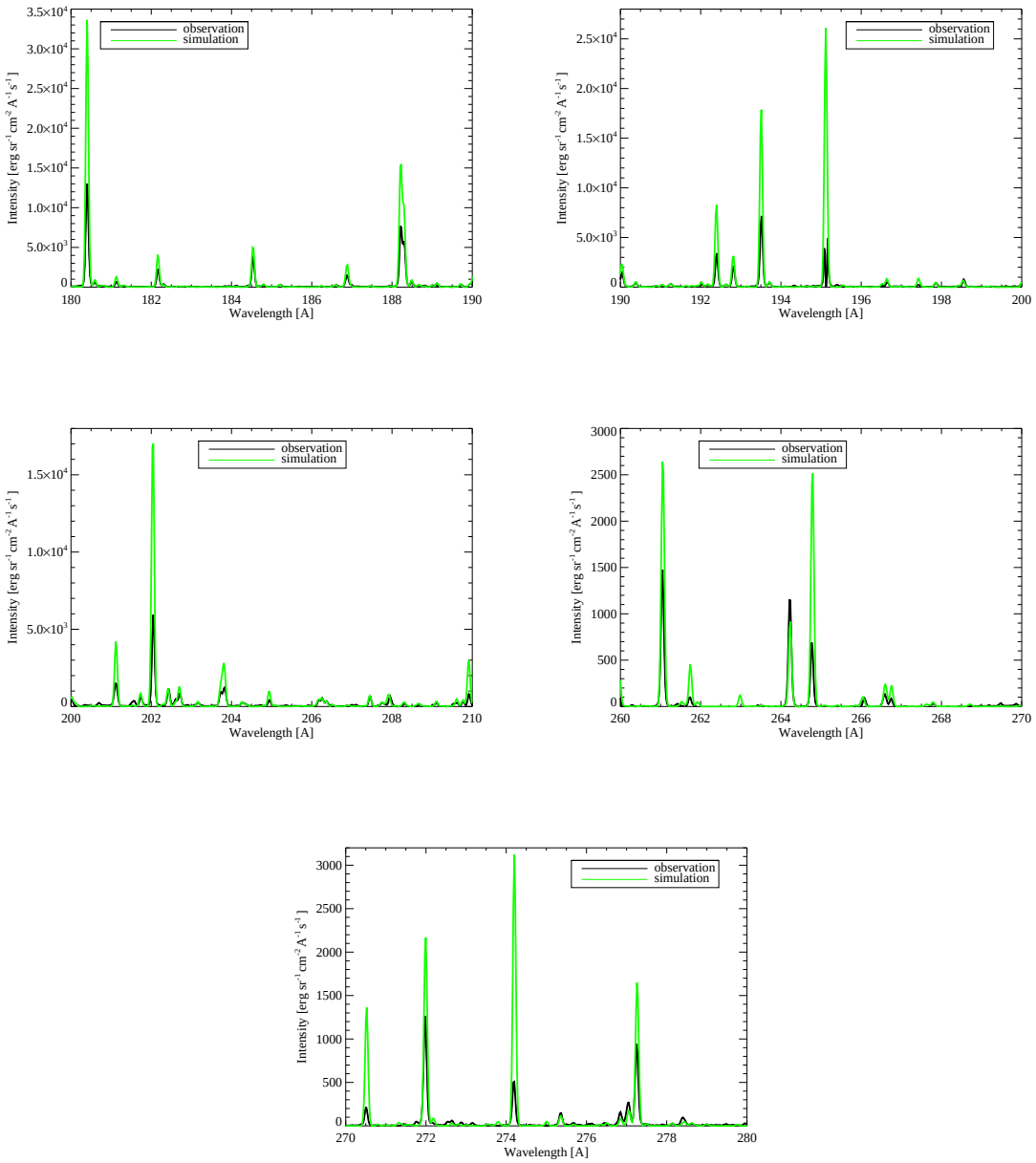

Figure 3.9: Comparison of coronal spectra of the observed *(black)* and simulated *(green)* plasmas in the closed magnetic field region. The synthetic spectra are scaled down by a factor of 10.

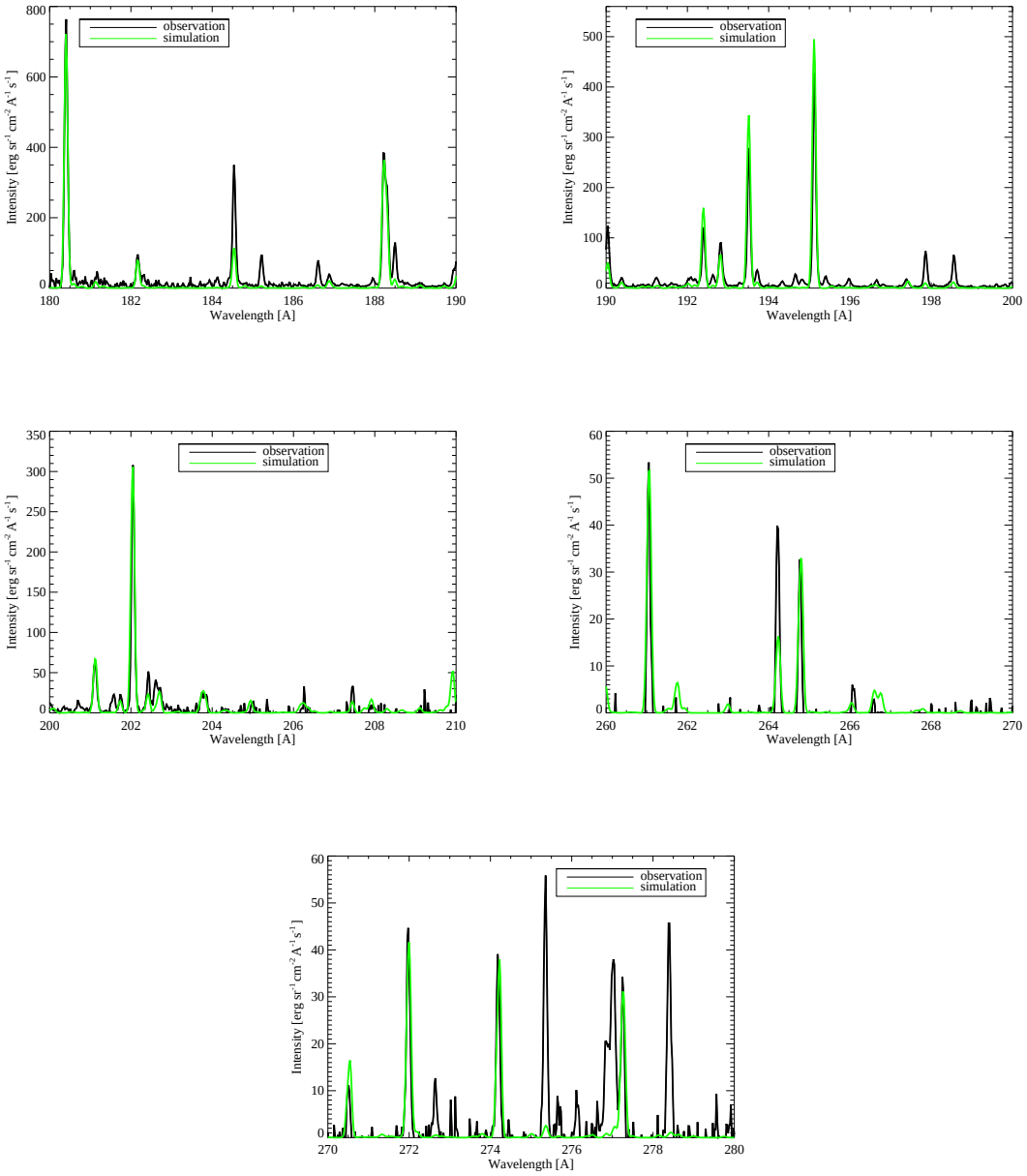

Figure 3.10: Comparison of coronal spectra of observed *(black)* and simulated *(green)* plasmas in open *(right)* magnetic field region. The synthetic spectra are scaled down by a factor 10.

The following list is an incomplete sample of commonly observed coronal ions with some comments about how their spectral lines look in the simulation compared to the observations:

- Fe VIII $\left(\lambda = 186.60 \text{ Å}, \log T = 5.6\right)$ is more overpredicted in the closed magnetic field region than in the open field of the coronal hole.

- Fe XI $\left(\lambda = 188.22 \text{ Å}, \log T = 6.1\right)$ and $\left(\lambda = 192.81 \text{ Å}, \log T = 6.1\right)$ line intensities are better predicted in the coronal hole, and after the scaling the line widths show a good match in both cases.

- Fe XII $\left(\lambda = 193.51 \text{ Å}, \log T = 6.2\right)$ shows a good match in width in both observational sites. $\left(\lambda = 195.12 \text{ Å}, \log T = 6.2\right)$ is predicted well in width and its intensity is less overpredicted in the coronal hole.

- Fe XIII $\left(\lambda = 203.79 \text{ Å}, \log T = 6.2\right)$ width is a good match in both cases.

- Fe XVII $\left(\lambda = 200.80 \text{ Å}, \log T = 6.5\right)$ is almost completely missing in both regions and both from simulation and observation, which is expected as this ion only exists in very hot regions, for example flares.

Figure 3.11 shows comparisons of individual lines in detail. The selected line is Fe XIII $\left(\lambda = 202.044 \text{ Å}, \log T = 6.3\right)$. Despite the intensity peaks are overestimated, and the Doppler shifts are slightly overpredicted, looking at neighboring lines, the relative line intensities and line widths show a good agreement. This suggests that the simulated plasma corresponding to this temperature has higher density and velocity than observed. To be able to analyze the discrepancies in such detail one has to take into account all errors in both the observations (instrumental error, data cleaning process) and modeling (e.g., missing magnetic field measurements at coronal holes that are input to the model (see for example, Linker et al., 2017). In this chapter we only present the capability of the SPECTRUM tool and will discuss the detailed model validation processes in the future.

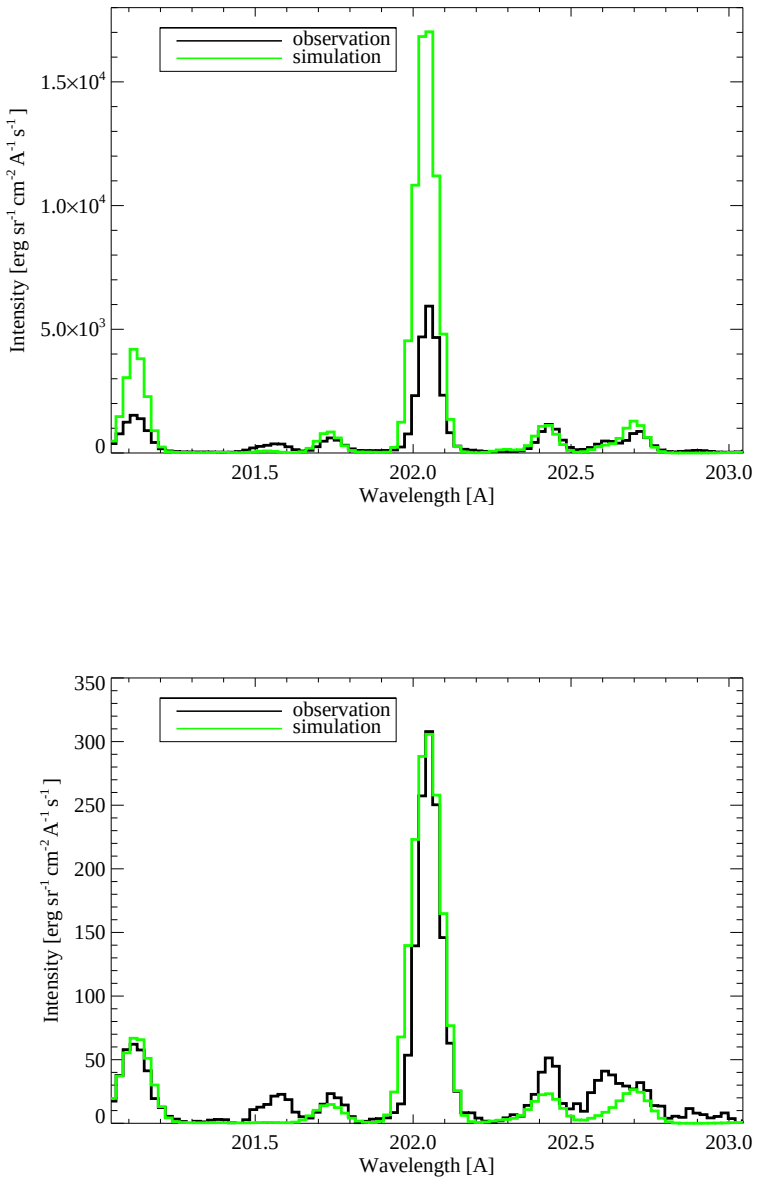

Figure 3.11: Synthetic spectral line profile of Fe XIII 202.044 Å obtained by SPECTRUM (*green*) compared to Hinode/EIS observation (*black*) for the West limb (*top*) and the North polar (*bottom*) observations of CR 2063.

3.4.2 Narrowband Imaging

SPECTRUM has the capability to apply instrument effective areas on the calculated intensities and create 2D narrowband images, such as those observed by

SoHO/EIT or SDO/AIA. Figure 3.12 is an example of both SoHO/EIT observations shown in Figure 3.3. To obtain such images, we need to save the data box surrounding the Sun. Figure 3.12 was created based on a box of sides 3 $R_\odot$ in length, 200 cells along each side. SPECTRUM calculated the full spectra from 165 to 350 Å for each cell within the box and convoluted them with the instrument's effective area to obtain the observed data number count (DN) measured with the imager. The conversion between between DN and physical intensity units is not a unique process. The line-of-sight images created in Figure 3.3 are obtained with a different method, using an older atmoic data and reflectivities than the direct calculation we perform. The resulting differences in brightness are expected.

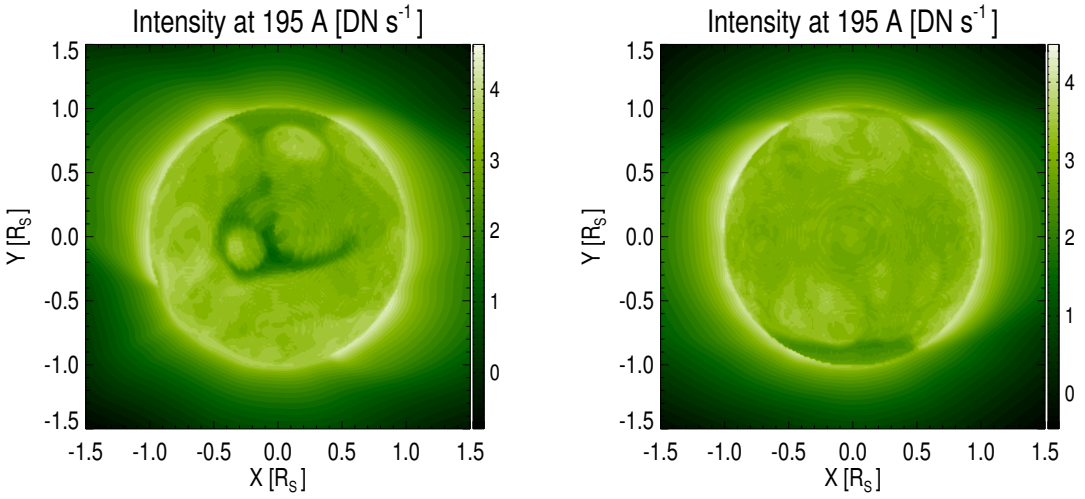

Figure 3.12: *Left to right:* LOS view of the modeled solar corona of CR 2063 and CR 2082. Synthetic narrowband images are calculated using synthetic spectra obtained from SPECTRUM in the wavelength range 165 Å to 350 Å, and instrumental response function from SoHO/EIT 195 Å. (The concentric cirles appear due to the low resolution of the images.)

3.4.3 Nonthermal Line Broadening and Effective Velocity

The third observation site is CR 2082, a quiet-Sun coronal hole. As discussed in Section 3.1, the effective velocity change along radial distance in the solar atmosphere

is a widely discussed and well-observed phenomena. While some observations support the theory of significant Alfvén wave dissipation happening in the low corona (e.g., Bemporad & Abbo, 2012; Hahn et al., 2012), others contradict this phenomena (e.g., Banerjee et al., 1998, 2009; Doyle et al., 1998). With SPECTRUM it is possible to obtain synthetic spectra of the above-mentioned studies and look for signatures of wave damping. The effective velocity is defined as:

$$v_{eff} = \sqrt{v_{th}^2 + v_{nth}^2}. \tag{3.18}$$

The thermal and nonthermal velocities (Equations 3.10 and 3.12) are obtained by estimating the FWHM (from Equation 3.2) of the LOS-integrated Gaussians:

$$\mathrm{FWHM} = \frac{\lambda_0}{c}\sqrt{8 \ln 2 \; v_{eff}^2}. \tag{3.19}$$

The effect of nonthermal broadening on the line width is presented via the different FWHM profiles predicted for the CR 2082 coronal hole observation, in Figure 3.13. Because the AWSoM model heats the corona purely by Alfvén wave dissipation, in

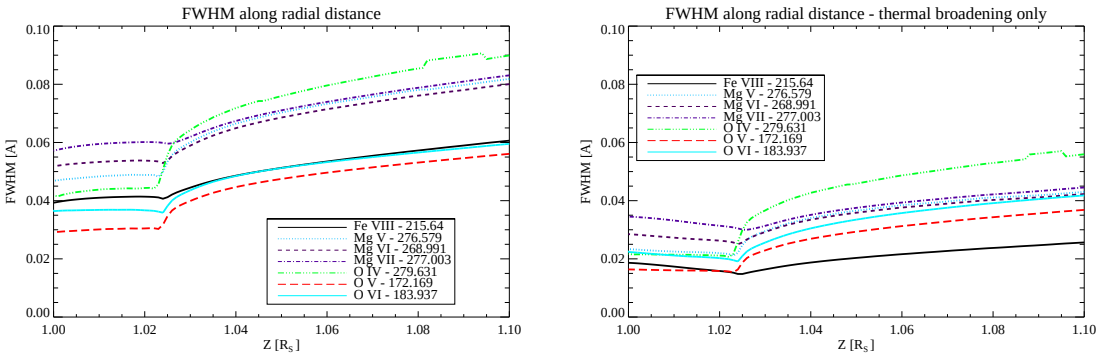

Figure 3.13: *Left to right:* FWHM for spectral lines of selected ions, having nonthermal effects included and excluded from the line profile calculation. The difference between the left and right panel shows that nonthermal broadening has a significant effect on line widths.

the simulation results we expect to see insignificant or no wave damping in the low coronal region, similar to observations and the theoretical predictions the model is based on (Hassler et al., 1990; Kohl et al., 1997; Doyle et al., 1999; Moran, 2001, 2003). The ion temperature, and as a result, the thermal component of the effective velocity increase with radial distance. The nonthermal component is due to perturbation propagation in the corona. In the model, the transverse velocity perturbation (Figure 3.14) increases with distance until about 5 $R_{\odot}$, and decreases thereafter. This suggests that the effective velocity profiles should only increase in the observed and modeled region. The data extraction site to calculate predicted emission line widths

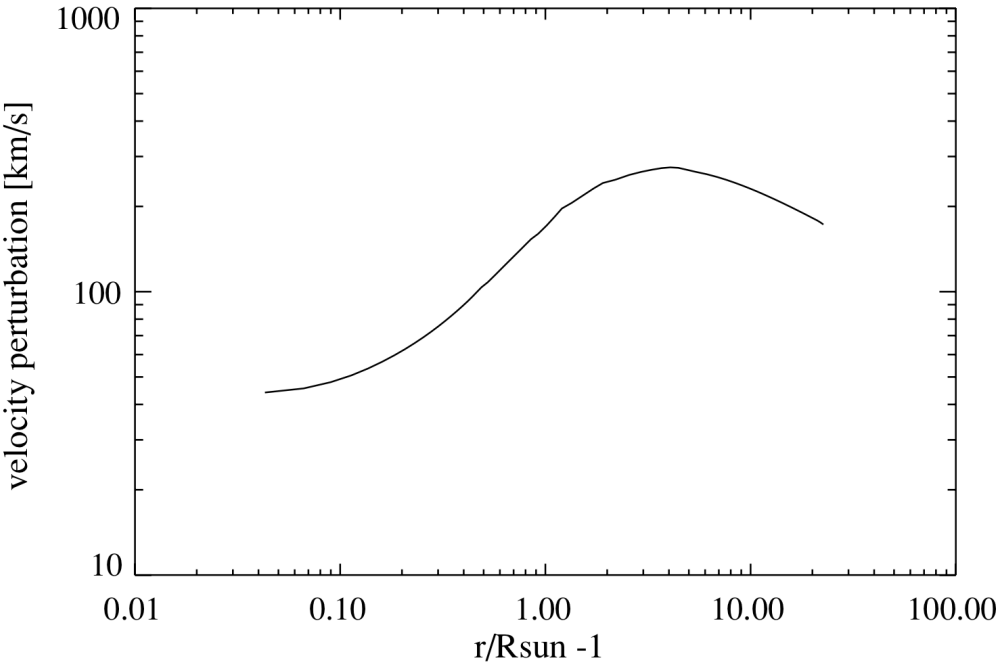

Figure 3.14: Figure 7 from van der Holst et al. (2010) shows the transverse velocity perturbation vs radial distance in a coronal hole of a two-temperature 3D simulation.

is chosen to be the same one analyzed by Hahn et al. (2012). Figure 5 of their paper shows a significant effective velocity drop in the low corona (shown in Figure 3.15). The decrease in effective velocities was attributed to wave damping in the coronal hole region below 1.4 solar radii. Using the synthetic data obtained from AWSoM,

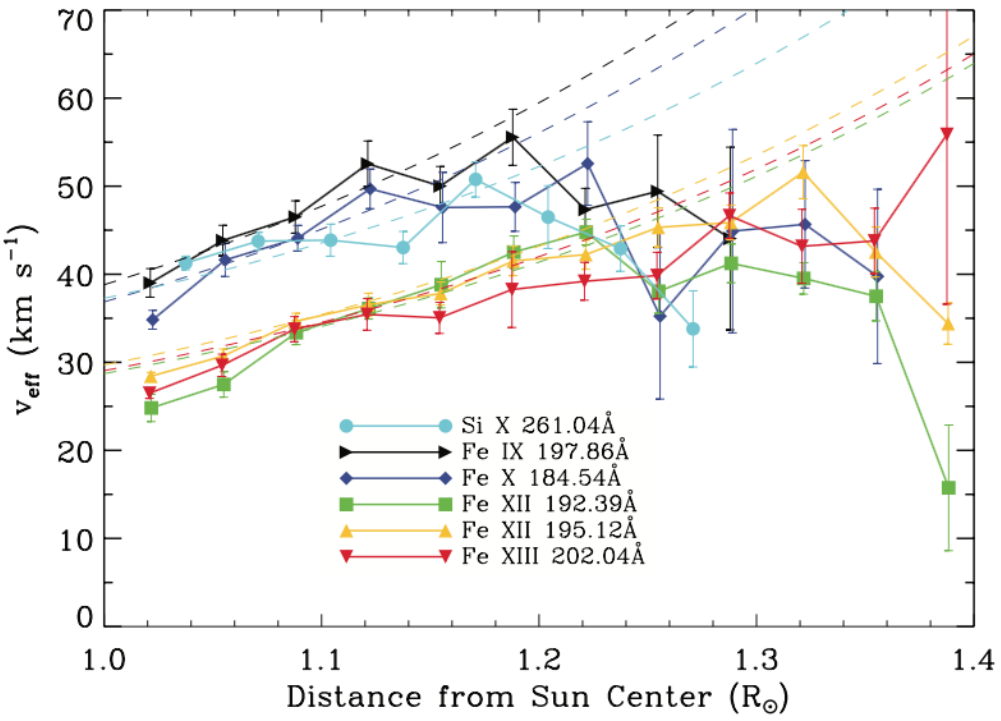

Figure 3.15: Figure 5 from Hahn et al. (2012) shows effective velocity of selected spectral lines vs radial distance in the coronal hole of CR 2082. Effective velocity profiles were interpreted as strong wave damping in the low coronal region, much stronger than expected by Alfvén-wave-heated theoretical coronal models. Dashed lines show for the effective velocity as a function of radial distance for each emission line in the case of undamped waves normalized at 1.1 $R_\odot$.

we also looked for this evidence of wave damping in the same region. If there were a significant decrease in effective velocity in the low corona, that would be attributed directly to wave damping in the region, and would be an argument against attributing the observed effective velocity decrease to some other (instrumental or scattering) effect. We extracted the data from the simulation results and calculated the spectral line profiles for the same ions as in the original paper. The intensity, the Doppler shift, the FWHM, and effective velocities vs radial distance from the southern pole for the six ions as in Hahn et al. (2012) are shown in Figure 3.16. The effective velocity change with radial distance obtained from the synthetic spectra shows no wave damping, or at least it is insignificant compared to what is observed. To further

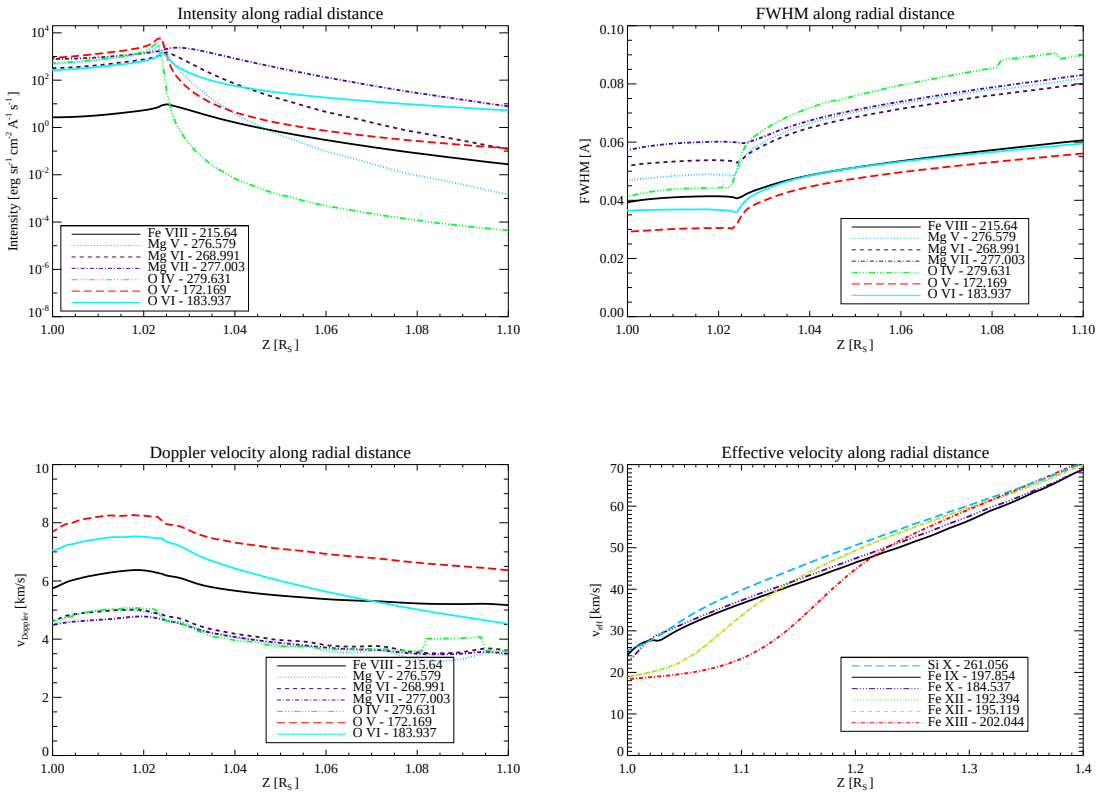

Figure 3.16: Predicted intensity (*top,left*), FWHM (*top,right*), Doppler shift (*bottom,left*), and effective velocity (*bottom,right*) of selected spectral lines along radial distance in the coronal hole of CR 2082. Effective velocities show little or no wave damping in the low coronal region compared to what was observed.

clarify, the spectra were calculated along one extracted 1D line inside the coronal hole. With this data set, we have no LOS effect, and can calculate the effective velocities based on spectra obtained from each plasma parcel along the radial distance. As expected, Figure 3.17 shows no difference between the effective velocities of ions of the same element, because the nonthermal velocities do not depend on charge but on the mass of the particle. Also, there is no drop in the effective velocities with height, as we observe in case of the Fe XII and Fe XIII lines on the bottom left panel in Figure 3.16. This result suggests that spectral observations are sensitive to LOS effects. Finally, SPECTRUM also provides 2D images of intensity, FWHM, thermal-

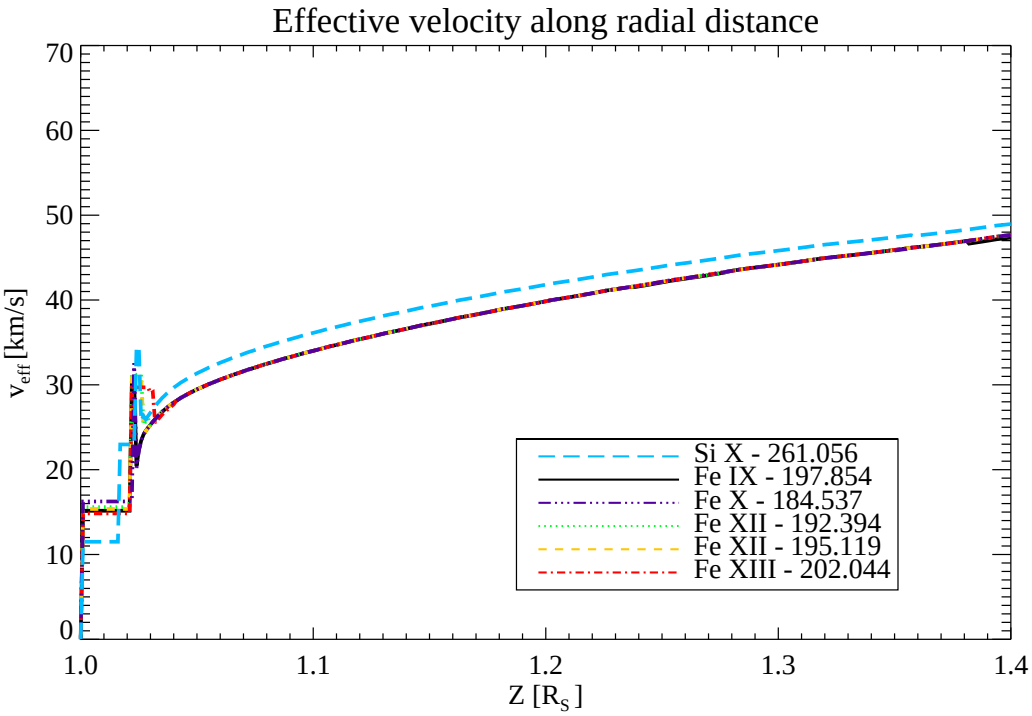

Figure 3.17: Effective velocities obtained from synthetic spectra using a 1D data set extracted from the same observation as in Figure 3.16 to avoid the line-of-sight effect.

and nonthermal velocity maps of any line, including those of Hinode/EIS HOP 130 (Warren et al., 2014). An example is shown for CR 2082 in Figure 3.18, using Fe XIII (202.04 Å) line. Because proton temperatures are higher in the open field region, we expect to see more line broadening above the coronal holes than above the closed field regions. Figure 3.18 shows significant broadening in the open magnetic field regions at the poles, where the effective velocities are also higher. The intensity drops in these coronal hole regions both on-disk and at the poles.

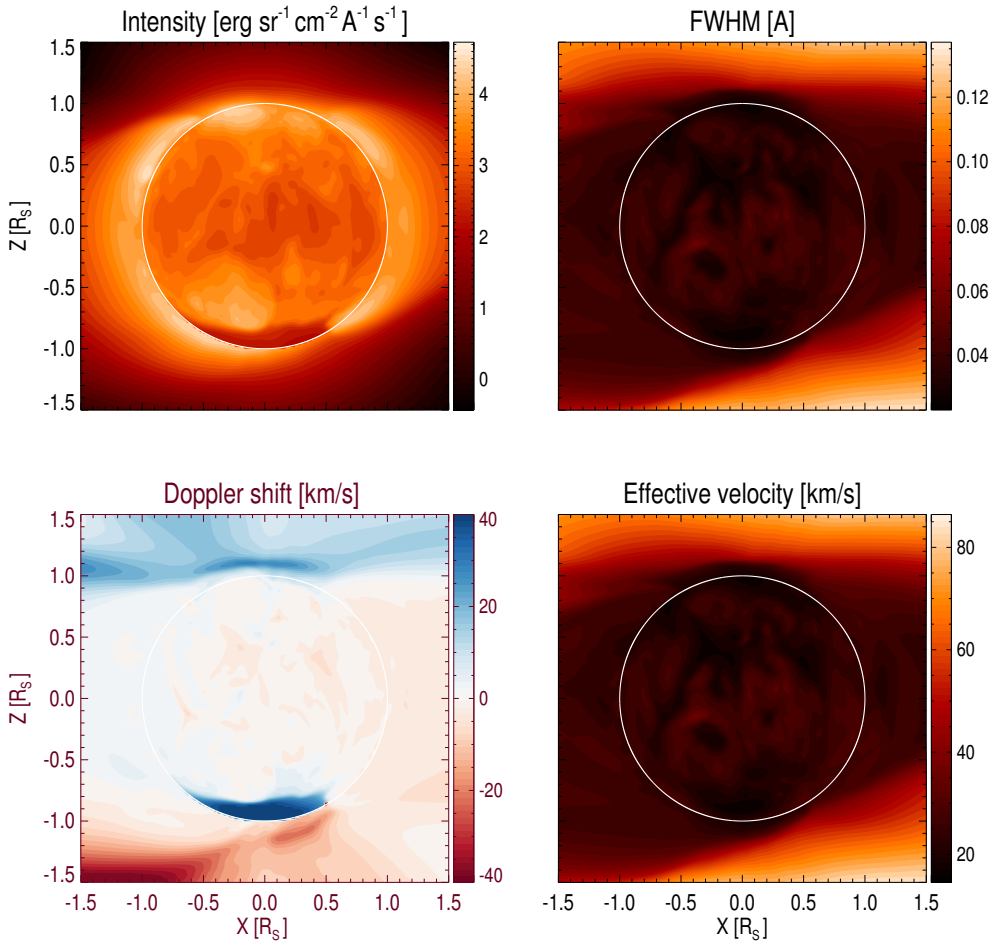

Figure 3.18: 2D synthetic maps of intensity (*top, left*), FWHM (*top, right*), Doppler shift (*bottom, left*), and effective velocity (*bottom, right*) of line Fe XIII 202.044 Å from the observer's LOS from CR 2082.

3.5 Summary of Chapter 3

SPECTRUM, a new post-processing tool available within the SWMF to perform synthetic spectral calculations, has been presented in this chapter. SPECTRUM calculates spectral line emission based on simulated MHD data using CHIANTI tables. We showed that synthetic spectra represent an invaluable diagnostics tool for solar observations, providing the potential to infer the three-dimensional density and temperature distributions by comparing the LOS observations with synthetic spectra

obtained from the numerical model. SPECTRUM can also be used for validating global simulations, as it can help to achieve a more realistic solar wind model for space weather predictions.

In the future, we plan to implement an automated process that distinguishes the open and closed magnetic field regions, so the difference between ion abundances can be taken into account during the calculations. We also plan to extend the calculations in SPECTRUM with resonant scattering, which enables the production of realistic synthetic coronagraph and eclipse observations of the corona above 1.5 solar radii with spectral lines in the visible frequency range. This would help to validate the modeled physical processes in the outer corona and provide better predictive capabilities, so SPECTRUM could be used not only for upcoming missions but also for space weather forecasting (Habbal et al., 2014; Landi et al., 2016; Tomczyk et al., 2016). In addition, AWSoM is currently being developed into a multi-fluid MHD global solar corona model, and SPECTRUM will be developed to take the multi-fluid solutions into account.

CHAPTER IV

Summary and Future Work

4.1 Summary

In the previous chapters we presented two approaches to study the mass, momentum and energy transport into the solar atmosphere using an MHD coronal model. First, we showed a coronal jet modeled with a realistic solar corona background. The simulated jet properties showed remarkable resemblance to observations both in size and dynamic behavior. Based on the simulation results, we estimated that jets contribute to the solar wind outflow on average less than 5%. This work revealed how dynamic processes of chromospheric origin interact with the corona. The results have been published (Szente et al., 2017). The second part of the thesis introduced SPECTRUM, which is a post-processing tool to calculate synthetic spectra of the low corona. We show products of SPECTRUM, which can be utilized to validate and analyze MHD coronal models relative to observations. For AWSoM, the results show that the current three-temperature coronal model is overestimating the line intensities, which may signify incorrect placement of the heat deposition. Substantial development of the coronal heating model is ongoing, and SPECTRUM will be udes to assess the improvements.

4.2 Future Plans

- Further examine how the thermal and nonthermal spectral-line widths change as a function of distance from the Sun in both observational and synthetic data, to study plasma heating and Alfvén wave properties, and aid in further development of the coronal heating implementation within the AWSoM model.

- Using multi-wavelength data sets based on both observations and correspondig simulations, we will analyze how the DEM calculation is affected by the reconstruction process (in our case, regularized inversion by Hannah & Kontar, 2012)). This study can complement the benchmark test effort by Aschwanden et al. (2015).

- The heating process is expected to have a strong influence on the shape of the DEM. Klimchuk (2017) showed that different nanoflare occurrence frequencies provided different power-law distributions in DEM curves, and comparison with observations lent support to nanoflare heating theories. As explanation, see the difference between the observed and simulated DEM shapes in Figure 1.10 and Figure 1.11. We will look at how a purely Alfvén-wave-driven coronal model reproduces these observations, and determine whether what is the slope range on the coolward part of the DEM peak can be explained by Alfvénic heating, taking into account the inversion uncertainties determined earlier.

- As mentioned in Section 3.5, further develop SPECTRUM by adding resonant scattering in order to extend the comparison to spectral observations obtained by the Upgraded Coronal Multi-channel Polarimeter at the Mauna Loa Solar Observatory (MLSO/UCoMP) in the visible wavelength range up to 2 solar radii. In low density plasmas resonant scattering is the process whereby in low-density plasma an ion absorbs a photon and re-emits it into another direction. This process enhances the observed flux of the emission line over the

nonresonant value. Because it also changes the line profile of the observed spectral line, the properties of the re-emitting ion can be measured (Phillips et al., 2008). This new feature can also be applied to spectra from the Solar Orbiter spectrometers, and will be valuable for future CME studies and eclipse observations.

BIBLIOGRAPHY

BIBLIOGRAPHY

Adams, M., Sterling, A. C., Moore, R. L., & Gary, G. A. 2014, *ApJ*, 783, 11

Alazraki, G., & Couturier, P. 1971, *A&A*, 13, 380

Antiochos, S. K. 1990, *Mem. Soc. Astron. Italiana*, 61, 369

Antiochos, S. K. 1996, in Astronomical Society of the Pacific Conference Series, Vol. 95, Solar Drivers of the Interplanetary and Terrestrial Disturbances, ed. K. S. Balasubramaniam, S. L. Keil, & R. N. Smartt, 1

Aschwanden, M. J. 2004, Physics of the Solar Corona. An Introduction (Praxis Publishing Ltd)

Aschwanden, M. J., Boerner, P., Caspi, A., et al. 2015, *Sol. Phys.*, 290, 2733

Athay, R. G., ed. 1976, Astrophysics and Space Science Library, Vol. 53, The solar chromosphere and corona: Quiet sun

Bame, S. J., McComas, D. J., Barraclough, B. L., et al. 1992, *A&AS*, 92, 237

Banerjee, D., Gupta, G. R., & Teriaca, L. 2011, *Space Sci. Rev.*, 158, 267

Banerjee, D., Pérez-Suárez, D., & Doyle, J. G. 2009, *A&A*, 501, L15

Banerjee, D., Teriaca, L., Doyle, J. G., & Wilhelm, K. 1998, *A&A*, 339, 208

Belcher, J. W. 1971, *ApJ*, 168, 509

Bemporad, A., & Abbo, L. 2012, *ApJ*, 751, 110

Bohlin, J. D., Vogel, S. N., Purcell, J. D., et al. 1975, *ApJ*, 197, L133

Box, G. 1979, in Robustness in Statistics, ed. R. L. LAUNER & G. N. WILKINSON (Academic Press), 201 – 236

Brooks, D. H., & Warren, H. P. 2006, *ApJS*, 164, 202

—. 2012, *ApJ*, 760, L5

—. 2016, *ApJ*, 820, 63

Brooks, D. H., Warren, H. P., Williams, D. R., & Watanabe, T. 2009, *ApJ*, 705, 1522

Brueckner, G. E., & Bartoe, J.-D. F. 1983, *ApJ*, 272, 329

Canfield, R. C., Reardon, K. P., Leka, K. D., et al. 1996, The Astrophysical Journal, 464, 1016

Carlsson, M., Stein, R. F., Nordlund, Å., & Scharmer, G. B. 2004, *ApJ*, 610, L137

Chandran, B. D. G., Dennis, T. J., Quataert, E., & Bale, S. D. 2011, *ApJ*, 743, 197

Chandrashekhar, K., Morton, R. J., Banerjee, D., & Gupta, G. R. 2014, *A&A*, 562, A98

Chen, H.-D., Zhang, J., & Ma, S.-L. 2012, Research in Astronomy and Astrophysics, 12, 573

Chen, Y., Tóth, G., & Gombosi, T. I. 2016, Journal of Computational Physics, 305, 604

Chifor, C., Young, P. R., Isobe, H., et al. 2008a, Astronomy & Astrophysics, 481, L57

Chifor, C., Isobe, H., Mason, H. E., et al. 2008b, Astronomy & Astrophysics, 491, 279

Cirtain, J. W., Golub, L., Lundquist, L., et al. 2007, Science, 318, 1580

Coleman, Jr., P. J. 1968, *ApJ*, 153, 371

Corti, G., Poletto, G., Suess, S. T., Moore, R. L., & Sterling, A. C. 2007, *ApJ*, 659, 1702

Cranmer, S. R. 2009, Living Reviews in Solar Physics, 6, 3

—. 2010, *ApJ*, 710, 676

Cranmer, S. R., Asgari-Targhi, M., Miralles, M. P., et al. 2015, Philosophical Transactions of the Royal Society of London Series A, 373, 20140148

Cranmer, S. R., Gibson, S. E., & Riley, P. 2017, *Space Sci. Rev.*, 212, 1345

Cranmer, S. R., & van Ballegooijen, A. A. 2005, *ApJS*, 156, 265

Cranmer, S. R., van Ballegooijen, A. A., & Edgar, R. J. 2007, *ApJS*, 171, 520

Culhane, J. L., Harra, L. K., James, A. M., et al. 2007a, *Sol. Phys.*, 243, 19

Culhane, L., Harra, L. K., Baker, D., et al. 2007b, Publications of the Astronomical Society of Japan, 59, 751

De Pontieu, B., McIntosh, S. W., Carlsson, M., et al. 2007, Science, 318, 1574

De Pontieu, B., Title, A. M., Lemen, J. R., et al. 2014, *Sol. Phys.*, 289, 2733

DeForest, C. E., Matthaeus, W. H., Viall, N. M., & Cranmer, S. R. 2016, *ApJ*, 828, 66

Del Zanna, G., Dere, K. P., Young, P. R., Landi, E., & Mason, H. E. 2015, *A&A*, 582, A56

Delaboudinière, J.-P., Artzner, G. E., Brunaud, J., et al. 1995, *Sol. Phys.*, 162, 291

Dere, K. P., Landi, E., Mason, H. E., Monsignori Fossi, B. C., & Young, P. R. 1997, *A&AS*, 125, 149

Dmitruk, P., Matthaeus, W. H., Milano, L. J., et al. 2002, *ApJ*, 575, 571

Domingo, V., Fleck, B., & Poland, A. I. 1995, *Sol. Phys.*, 162, 1

Doschek, G. A., Landi, E., Warren, H. P., & Harra, L. K. 2010, *ApJ*, 710, 1806

Doyle, J. G., Banerjee, D., & Perez, M. E. 1998, *Sol. Phys.*, 181, 91

Doyle, J. G., Teriaca, L., & Banerjee, D. 1999, *A&A*, 349, 956

Fang, F., Fan, Y., & McIntosh, S. W. 2014, *ApJ*, 789, L19

Feldman, U., Mandelbaum, P., Seely, J. F., Doschek, G. A., & Gursky, H. 1992, *ApJS*, 81, 387

Fletcher, L., Dennis, B. R., Hudson, H. S., et al. 2011, *Space Sci. Rev.*, 159, 19

Gibson, S. 2014, Proceedings of the International Astronomical Union, 10, 245250

Gibson, S., Kucera, T., White, S., et al. 2016, Frontiers in Astronomy and Space Sciences, 3, 8

Golub, L., & Pasachoff, J. M. 1997, The Solar Corona (Cambridge University Press)

Golub, L., Deluca, E., Austin, G., et al. 2007, *Sol. Phys.*, 243, 63

Gombosi. 1998, Physics of the Space Environment, 1st edn. (Cambridge UK: Cambridge University Press)

Gupta, G. R. 2017, *ApJ*, 836, 4

Gupta, G. R., Banerjee, D., Teriaca, L., Imada, S., & Solanki, S. 2010, *ApJ*, 718, 11

Gurnett, D. A., & Bhattacharjee, A. 2005, Introduction to Plasma Physics (Cambridge University Press), 462

Habbal, S. R., Morgan, H., & Druckmüller, M. 2014, *ApJ*, 793, 119

Hahn, M., Landi, E., & Savin, D. W. 2012, *ApJ*, 753, 36

Hahn, M., & Savin, D. W. 2014, *ApJ*, 795, 111

Handy, B. N., Acton, L. W., Kankelborg, C. C., et al. 1999, *Sol. Phys.*, 187, 229

Hannah, I. G., Hudson, H. S., Battaglia, M., et al. 2011, *Space Sci. Rev.*, 159, 263

Hannah, I. G., & Kontar, E. P. 2012, *A&A*, 539, A146

Harrison, R. A., Hood, A. W., & Pike, C. D. 2002, *A&A*, 392, 319

Harrison, R. A., Sawyer, E. C., Carter, M. K., et al. 1995, *Sol. Phys.*, 162, 233

Hassler, D. M., Rottman, G. J., Shoub, E. C., & Holzer, T. E. 1990, *ApJ*, 348, L77

Heinemann, M., & Olbert, S. 1980, *J. Geophys. Res.*, 85, 1311

Hirayama, T. 1974, *Sol. Phys.*, 34, 323

Hollweg, J. V. 1978, Reviews of Geophysics and Space Physics, 16, 689

Huang, Z., Frazin, R. A., Landi, E., et al. 2012, *ApJ*, 755, 86

Jess, D. B., Mathioudakis, M., Erdélyi, R., et al. 2009, Science, 323, 1582

Jian, L. K., MacNeice, P. J., Taktakishvili, A., et al. 2015, Space Weather, 13, 316

Jin, M., Manchester, W. B., van der Holst, B., et al. 2017a, *ApJ*, 834, 172

—. 2012, *ApJ*, 745, 6

—. 2013, The Astrophysical Journal, 773, 50

—. 2017b, *ApJ*, 834, 173

Kaastra, J. S., Paerels, F. B. S., Durret, F., Schindler, S., & Richter, P. 2008, *Space Sci. Rev.*, 134, 155

Kaiser, M. L., Kucera, T. A., Davila, J. M., et al. 2008, *Space Sci. Rev.*, 136, 5

Kamio, S., Hara, H., Watanabe, T., et al. 2007, Publications of the Astronomical Society of Japan, 59, 757

Karpen, J. T., DeVore, C. R., Antiochos, S. K., & Pariat, E. 2017, *ApJ*, 834, 62

Kim, Y.-H., Moon, Y.-J., Park, Y.-D., et al. 2007, Publications of the Astronomical Society of Japan, 59, 763

King, J. H., & Papitashvili, N. E. 2005, Journal of Geophysical Research (Space Physics), 110, A02104

Klimchuk, J. A. 2006, *Sol. Phys.*, 234, 41

—. 2015, Philosophical Transactions of the Royal Society of London Series A, 373, 20140256

—. 2017, ArXiv e-prints, arXiv:1709.07320

Kohl, J. L., Esser, R., Gardner, L. D., et al. 1995, *Sol. Phys.*, 162, 313

Kohl, J. L., Noci, G., Antonucci, E., et al. 1997, *Sol. Phys.*, 175, 613

Kosugi, T., Matsuzaki, K., Sakao, T., et al. 2007, *Sol. Phys.*, 243, 3

Kumar, P., Karpen, J. T., Antiochos, S. K., et al. 2018, *ApJ*, 854, 155

Laming, J. M. 2015, Living Reviews in Solar Physics, 12, 2

Landi, E. 2007, *ApJ*, 663, 1363

Landi, E., & Cranmer, S. R. 2009, *ApJ*, 691, 794

Landi, E., Habbal, S. R., & Tomczyk, S. 2016, Journal of Geophysical Research (Space Physics), 121, 8237

Landi, E., Young, P. R., Dere, K. P., Del Zanna, G., & Mason, H. E. 2013, *ApJ*, 763, 86

Landi Degl'Innocenti, E. 2014, Atomic Spectroscopy and Radiative Processes (Springer-Verlag Italia)

Lemen, J. R., Title, A. M., Akin, D. J., et al. 2012, *Sol. Phys.*, 275, 17

Li, X., Morgan, H., Leonard, D., & Jeska, L. 2012, The Astrophysical Journal Letters, 752, L22

Linker, J. A., Caplan, R. M., Downs, C., et al. 2017, *ApJ*, 848, 70

Lionello, R., Linker, J. A., & Mikić, Z. 2009, *ApJ*, 690, 902

Liu, J., Wang, Y., Shen, C., et al. 2015, *ApJ*, 813, 115

Madjarska, M. S. 2011, Astronomy & Astrophysics, 526, A19

Madjarska, M. S., Doyle, J. G., Innes, D. E., & Curdt, W. 2007, The Astrophysical Journal Letters, 670, L57

Matthaeus, W. H., Zank, G. P., Oughton, S., Mullan, D. J., & Dmitruk, P. 1999, *ApJ*, 523, L93

McComas, D. J., Elliott, H. A., Schwadron, N. A., et al. 2003, *Geophys. Res. Lett.*, 30, 1517

McIntosh, S. W., & De Pontieu, B. 2012, *ApJ*, 761, 138

McIntosh, S. W., de Pontieu, B., Carlsson, M., et al. 2011, *Nature*, 475, 477

Meng, X., van der Holst, B., Tóth, G., & Gombosi, T. I. 2015, *MNRAS*, 454, 3697

Mickey, D. L., Canfield, R. C., Labonte, B. J., et al. 1996, *Sol. Phys.*, 168, 229

Moore, R. L., Cirtain, J. W., Sterling, A. C., & Falconer, D. A. 2010, *ApJ*, 720, 757

Moore, R. L., Sterling, A. C., & Falconer, D. A. 2015, *ApJ*, 806, 11

Moore, R. L., Sterling, A. C., Falconer, D. A., & Robe, D. 2013, *ApJ*, 769, 134

Moran, T. G. 2001, *A&A*, 374, L9

—. 2003, *ApJ*, 598, 657

Moreno-Insertis, F., & Galsgaard, K. 2013, The Astrophysical Journal, 771, 20

Moschou, S. P., Tsinganos, K., Vourlidas, A., & Archontis, V. 2013, Solar Physics, 284, 427

Newkirk, Jr., G. 1967, *ARA&A*, 5, 213

Nishizuka, N., Nakamura, T., Kawate, T., Singh, K. A. P., & Shibata, K. 2011, The Astrophysical Journal, 731, 43

Nishizuka, N., Shimizu, M., Nakamura, T., et al. 2008, The Astrophysical Journal Letters, 683, L83

Nuevo, F. A., Huang, Z., Frazin, R., et al. 2013, *ApJ*, 773, 9

Ogawara, Y., Takano, T., Kato, T., et al. 1991, *Sol. Phys.*, 136, 1

Okamoto, T. J., Tsuneta, S., & Berger, T. E. 2010, The Astrophysical Journal, 719, 583

Oran, R., Landi, E., van der Holst, B., Sokolov, I. V., & Gombosi, T. I. 2017, The Astrophysical Journal, 845, 98

Panasenco, O., Martin, S. F., & Velli, M. 2014, Solar Physics, 289, 603

Paraschiv, A. R., Bemporad, A., & Sterling, A. C. 2015, Astronomy & Astrophysics, 579, A96

Pariat, E., Antiochos, S. K., & DeVore, C. R. 2009, The Astrophysical Journal, 691, 61

—. 2010, The Astrophysical Journal, 714, 1762

Pariat, E., Dalmasse, K., DeVore, C. R., Antiochos, S. K., & Karpen, J. T. 2015, Astronomy & Astrophysics, 573, A130

—. 2016, *A&A*, 596, A36

Parker, E. N. 1958, *ApJ*, 128, 664

—. 1965, *Space Sci. Rev.*, 4, 666

—. 1972, *ApJ*, 174, 499

—. 1988, *ApJ*, 330, 474

Patsourakos, S., & Klimchuk, J. A. 2006, *ApJ*, 647, 1452

Patsourakos, S., Klimchuk, J. A., & Young, P. R. 2014, *ApJ*, 781, 58

Patsourakos, S., Pariat, E., Vourlidas, A., Antiochos, S. K., & Wuelser, J. P. 2008, The Astrophysical Journal Letters, 680, L73

Penn, M. J., Mickey, D. L., Canfield, R. C., & Labonte, B. J. 1991, *Sol. Phys.*, 135, 163

Pesnell, W. D., Thompson, B. J., & Chamberlin, P. C. 2012, *Sol. Phys.*, 275, 3

Phillips, K. J. H., Feldman, U., & Landi, E. 2008, Ultraviolet and X-ray Spectroscopy of the Solar Atmosphere (Cambridge University Press)

Poletto, G., Sterling, A. C., Pucci, S., & Romoli, M. 2014, in IAU Symposium, Vol. 300, Nature of Prominences and their Role in Space Weather, ed. B. Schmieder, J.-M. Malherbe, & S. T. Wu, 239–242

Powell, K. G. 1994, Approximate Riemann solver for magnetohydrodynamics (that works in more than one dimension), Tech. rep., Institute for Computer Applications in Science and Engineering, NASA Langley Research Center

Powell, K. G., Roe, P. L., Linde, T. J., Gombosi, T. I., & De Zeeuw, D. L. 1999, Journal of Computational Physics, 154, 284

Pucci, S., Poletto, G., Sterling, A. C., & Romoli, M. 2012, *ApJ*, 745, L31

—. 2013, *ApJ*, 776, 16

Riley, P., Linker, J. A., & Arge, C. N. 2015, Space Weather, 13, 154

Savcheva, A., Cirtain, J., Deluca, E. E., et al. 2007, Publications of the Astronomical Society of Japan, 59, 771

Schatten, K. H., Wilcox, J. M., & Ness, N. F. 1969, *Sol. Phys.*, 6, 442

Schmidt, W., von der Lühe, O., Volkmer, R., et al. 2012, Astronomische Nachrichten, 333, 796

Schrijver, C. J. 2001, in Astronomical Society of the Pacific Conference Series, Vol. 223, 11th Cambridge Workshop on Cool Stars, Stellar Systems and the Sun, ed. R. J. Garcia Lopez, R. Rebolo, & M. R. Zapaterio Osorio, 131

Schrijver, C. J., & De Rosa, M. L. 2003, *Sol. Phys.*, 212, 165

Schrijver, C. J., & Siscoe, G. L. 2009, Heliophysics: Plasma Physics of the Local Cosmos (Cambridge University Press)

Shen, Y., Liu, Y., Su, J., & Ibrahim, A. 2011, The Astrophysical Journal Letters, 735, L43

Shibata, K. 1982, Solar Physics, 81, 9

Shibata, K., Nitta, N., Strong, K. T., et al. 1994, The Astrophysical Journal Letters, 431, L51

Shibata, K., Ishido, Y., Acton, L. W., et al. 1992, Publications of the Astronomical Society of Japan, 44, L173

Shibata, K., Nakamura, T., Matsumoto, T., et al. 2007, Science, 318, 1591

Shimojo, M., Hashimoto, S., Shibata, K., et al. 1996, Publications of the Astronomical Society of Japan, 48, 123

Shimojo, M., Narukage, N., Kano, R., et al. 2007, Publications of the Astronomical Society of Japan, 59, 745

Singh, K. A. P., Isobe, H., Nishizuka, N., Nishida, K., & Shibata, K. 2012, The Astrophysical Journal, 759, 33

Sokolov, I. V., van der Holst, B., Oran, R., et al. 2013, *ApJ*, 764, 23

Srivastava, A. K., & Murawski, K. 2011, *A&A*, 534, A62

Sterling, A. C., Harra, L. K., & Moore, R. L. 2010, *ApJ*, 722, 1644

Sterling, A. C., Moore, R. L., Falconer, D. A., & Adams, M. 2015, *Nature*, 523, 437

Sterling, A. C., Shibata, K., & Mariska, J. T. 1993, *ApJ*, 407, 778

—. 1994, *Space Sci. Rev.*, 70, 77

Szente, J., Toth, G., Manchester, IV, W. B., et al. 2017, The Astrophysical Journal, 834, 123

Tlatov, A. G., Pashchenko, M. P., Ponyavin, D. I., et al. 2016, Geomagnetism and Aeronomy, 56, 1095

Tomczyk, S., Landi, E., Burkepile, J. T., et al. 2016, Journal of Geophysical Research (Space Physics), 121, 7470

Tóth, G., van der Holst, B., Sokolov, I. V., et al. 2012, Journal of Computational Physics, 231, 870

Tsuneta, S., Acton, L., Bruner, M., et al. 1991, *Sol. Phys.*, 136, 37

Tsuneta, S., Ichimoto, K., Katsukawa, Y., et al. 2008, *Sol. Phys.*, 249, 167

Vaiana, G. S., & Rosner, R. 1978, *ARA&A*, 16, 393

van der Holst, B., Manchester, IV, W. B., Frazin, R. A., et al. 2010, *ApJ*, 725, 1373

van der Holst, B., Sokolov, I. V., Meng, X., et al. 2014, *ApJ*, 782, 81

Velli, M., Grappin, R., & Mangeney, A. 1989, Physical Review Letters, 63, 1807

Verdini, A., & Velli, M. 2007, *ApJ*, 662, 669

Wang, Y.-M., Sheeley, Jr., N. R., Socker, D. G., et al. 1998, The Astrophysical Journal, 508, 899

Warren, H. P., Ugarte-Urra, I., & Landi, E. 2014, *ApJS*, 213, 11

Wenzel, K. P., Marsden, R. G., Page, D. E., & Smith, E. J. 1992, *A&AS*, 92, 207

Wilhelm, K., Curdt, W., Marsch, E., et al. 1995, *Sol. Phys.*, 162, 189

Wuelser, J.-P., Lemen, J. R., Tarbell, T. D., et al. 2004, in *Proc. SPIE*, Vol. 5171, Telescopes and Instrumentation for Solar Astrophysics, ed. S. Fineschi & M. A. Gummin, 111–122

Wyper, P. F., Antiochos, S. K., & DeVore, C. R. 2017, *Nature*, 544, 452

Wyper, P. F., & DeVore, C. R. 2016, *ApJ*, 820, 77

Wyper, P. F., DeVore, C. R., & Antiochos, S. K. 2018, *ApJ*, 852, 98

Wyper, P. F., DeVore, C. R., Karpen, J. T., & Lynch, B. J. 2016, *ApJ*, 827, 4

Yang, L., He, J., Peter, H., et al. 2013, The Astrophysical Journal, 777, 16

Yokoyama, T., & Shibata, K. 1995, Nature, 375, 42

Yokoyama, T., & Shibata, K. 1996, Publications of the Astronomical Society of Japan, 48, 353

Yokoyama, T., & Shibata, K. 1999, in American Institute of Physics Conference Series, Vol. 471, American Institute of Physics Conference Series, ed. S. T. Suess, G. A. Gary, & S. F. Nerney, 61–66

Zaqarashvili, T. V., Oliver, R., & Ballester, J. L. 2006, *A&A*, 456, L13